Sheffield Hallam University

Formation of metal-gallium nitride contacts.

MAFFEIS, Thierry Gabriel Georges.

Available from Sheffield Hallam University Research Archive (SHURA) at:

http://shura.shu.ac.uk/19998/

This document is the author deposited version. You are advised to consult the publisher's version if you wish to cite from it.

Published version

MAFFEIS, Thierry Gabriel Georges. (2001). Formation of metal-gallium nitride contacts. Doctoral, Sheffield Hallam University (United Kingdom)..

Copyright and re-use policy

See http://shura.shu.ac.uk/information.html

Sheffield Hallam University Research Archive
http://shura.shu.ac.uk

CITY CAMPUS, POND STREET,
SHEFFIELD, S1 1WB.

101 657 638 2

REFERENCE

ProQuest Number: 10697305

All rights reserved

INFORMATION TO ALL USERS
The quality of this reproduction is dependent upon the quality of the copy submitted.

In the unlikely event that the author did not send a complete manuscript
and there are missing pages, these will be noted. Also, if material had to be removed,
a note will indicate the deletion.

ProQuest 10697305

Published by ProQuest LLC (2017). Copyright of the Dissertation is held by the Author.

All rights reserved.
This work is protected against unauthorized copying under Title 17, United States Code
Microform Edition © ProQuest LLC.

ProQuest LLC.
789 East Eisenhower Parkway
P.O. Box 1346
Ann Arbor, MI 48106 – 1346

Formation of Metal-Gallium Nitride Contacts

Thierry Gabriel Georges Maffeïs

A thesis submitted in partial fulfilment of the requirements of
Sheffield Hallam University
for the degree of Doctor of Philosophy

In collaboration with the University of Sheffield

March 2001

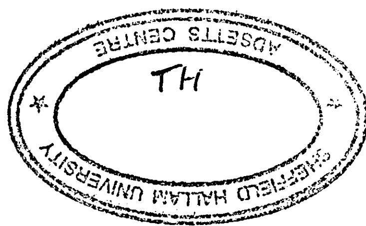

Contents

Title page i

Contents ii

Abstract v

Acknowledgements vi

Chapter 1: Introduction 1

Chapter 2: Literature review 6

2.1 Practical contacts 7

2.1.1 Ohmic contacts to nGaN 7

2.1.2 Ohmic contacts to pGaN 9

2.1.3 Schottky contacts to nGaN 10

2.2 Intimate contacts 13

2.2.1 Clean GaN surfaces 13

2.2.2 Metal contacts 15

2.3 Summary 17

Chapter 3: Theory of metal-semiconductor contacts 19

3.1 Models of metal-semiconductor contact formation 20

3.1.1 The Schottky-Mott model 20

3.1.2 The Bardeen model 23

3.1.3 Intimate contacts 25

3.1.4 Bias dependence of the barrier height 26

3.1.5 Electronegativity and ionicity 27

3.1.6 The MIGS-and-electronegativity model 29

3.1.7 The Cowley-Sze model 30

3.1.8 The effective work function model 31

3.2 Current transport mechanisms 32

3.2.1 Emission over the barrier 32

3.2.2 Tunnelling through the barrier 33

3.2.3 Recombination current 35

3.2.4 Ideality factor 35

3.3 Extraction of the Schottky parameters 37
3.3.1 Norde plot 37
3.3.2 Small signal conductance 38
3.3.3 Flat-band barrier height 39

Chapter 4: Experimental techniques 40

4.1 The Photoemission process 41

4.2 The three step model 42

4.3 Photo-ionisation cross section 46

4.4 Surface sensitivity 47
4.4.1 Electron scattering and inelastic mean free path (IMFP) 47
4.4.2 Effective escape depth: Changing the angle of detection 48
4.4.3 Photoelectron diffraction 49

4.5 Spectral interpretation 50
4.5.1 Auger lines 50
4.5.2 X-ray satellites and ghosts 51
4.5.3 Loss features 52

4.6 Core level analysis 53
4.6.1 Structural or surface related shifts 53
4.6.2 Chemical shifts 53
4.6.3 Band bending 54
4.6.4 Lineshape broadening effects 54
4.6.5 Core level intensities and overlayer growth 55
4.6.6 Spin orbit splitting 56
4.6.7 Asymmetric metal core levels 57
4.6.8 Deconvolution of core level spectra 57

4.7 XPS at the Material Research Institute 59
4.7.1 Experimental set-up 59
4.7.2 Electron energy analyser 61

4.8 SXPS at Daresbury laboratory 63

4.9 Transmission Electron Microscopy 64
4.9.1 Principle 64
4.9.2 Sample preparation 66

4.10 Transport measurement 67

Chapter 5: Cleaning of GaN 68

5.1 Introduction 68

5.2 Wet chemical etching in an HF solution 70

5.3 UHV annealing 73

5.4 Ga reflux cleaning 76

5.5 Ag contacts: transport measurements 81

5.6 Summary 85

Chapter 6: Au-nGaN contact formation 87

6.1 Introduction 87

6.2 Experimental details 88

6.3 Deposition on *in-situ* annealed surface 90

6.3.1 Core level intensity 90

6.3.2 Core level binding energy 93

6.3.3 I-V results 97

6.4 Deposition on *in-situ* Ga reflux cleaned surface 102

6.4.1 Core level intensity 102

6.4.2 Core level binding energy 104

6.4.3 I-V results 108

6.5 Deposition on chemically treated surface 112

6.5.1 Core level intensity 112

6.5.2 Core level binding energy 113

6.6 Discussion 117

6.6.1 Interface formation 117

6.6.2 Schottky barrier formation 120

6.6.3 Conclusions 125

Chapter 7: Conclusion 127

References 131

Abstract

The influence of pre-metallisation surface preparation on the structural, chemical, and electrical properties of metal-nGaN interfaces has been investigated by X-ray Photoemission Spectroscopy (XPS), current-voltage measurement (I-V) and cross section Transmission Electron Microscopy (TEM).

XPS analysis showed that the three GaN substrate treatments investigated, *ex-situ* HF etch, *in-situ* anneal in Ultra-High-Vacuum (UHV), and *in-situ* Ga reflux cleaning in UHV result in surfaces increasingly free of contaminants. Additionally, the three treatments are found to induce increasingly larger upward band bending. Ag-nGaN contacts formed after Ga reflux cleaning exhibit a Schottky barrier height of 0.80 eV and an ideality factor of 1.56, as determined by I-V.

XPS and TEM characterisation of Au-nGaN formed after the three pre-metallisation surface treatments show that HF etching and UHV annealing produce abrupt, well-defined interfaces. Conversely, GaN substrate cleaning in a Ga flux results in Au/GaN intermixing. I-V characterisation of Au-nGaN contacts yield a Schottky barrier height of 1.25 eV with very low ideality factor and very good contact uniformity for the pre-metallisation UHV anneal while the Ga reflux cleaning result in a much lower barrier (0.85 eV), with poor ideality and uniformity. I-V and XPS results suggest a high density of acceptor states at the surface, which is further enhanced by UHV annealing.

The mechanisms of Ga-nGaN, Ag-nGaN and Au-nGaN Schottky barrier formation are discussed in the context of the Metal-Induced Gap States model (MIGS) Unified Defect Model (UDM) and Cowley-Sze model.

Acknowledgements

I would like to express my gratitude to my supervisors, Dr Simon A. Clark and Dr. Peter J. Parbrook, for giving me the opportunity to carry out this research work at the Sheffield Hallam and Sheffield universities, and for their guidance throughout the course of the work. I am very grateful to Dr. Mike C. Simmonds for his help and support during the experimental work at the Material Research Institute. I would like to thank Mr. Paul Haines and Mr Geoff France for their technical support, and Dr. Henning Riechert and Dr. Victoria Roberts for kindly providing the samples. I am also very grateful to Dr. John P. David for his assistance and to Dr. Francesca Peiro for her help and expertise in Barcelona. Thanks to Pierre, Sonia, Tom, Pete and Jane for making my stay in Sheffield more interesting!

Acknowledgements are made to the joint studentship scheme, which gave me access to facilities at both Sheffield universities.

Finally, my gratitude to my family, especially Ann for her patience and encouragement.

Chapter 1: Introduction

Since the discovery of the rectifying properties of metal semiconductor contacts[1] in 1874, semiconductor devices have evolved from scientific curiosity to be part of our every day life. The major breakthrough came in 1947 with the invention of the transistor[2]. This first transistor was fabricated using Germanium, but it was another group IV element, Silicon, which transformed electronics. Silicon, whose main application is the computer chip, is still by far the most used substrate material in the semiconductor industry. Other material systems with established industrial applications include III-V compounds such as Indium Phosphide (InP) and Gallium Arsenide (GaAs). Their applications are mainly optoelectronics devices such as red and infra-red lasers used in CD players or fibre optics telecommunication, and high frequency microelectronics devices employed, for example, in mobile phones.

Two of the great advantages of III-V compounds over single element semiconductor such as Si, are their direct band gaps and the possibility of modifying the band gap by changing the ternary or quaternary alloy composition. These properties led, amongst other applications, to the fabrication of light emitting devices (LED) and laser

diodes (LD) whose emission wavelengths can be chosen by altering the compound composition. However, the wavelengths that devices fabricated on GaAs and InP can attain only range from near infra red to red, which leaves out most of the visible spectrum.

Blue LEDs and LDs, in particular, have great potential applications such as LED screen displays and high density optical storage. To reach these shorter wavelengths, a wider band gap semiconductor is needed. Gallium Nitride (GaN) is a novel III-V semiconductor with a direct band gap of 3.4 eV and is therefore a good candidate for blue LED fabrication.

Professor J. Pankove pioneered the study of GaN and demonstrated the first blue LED using a Metal-Insulator-Semiconductor structure[3] in 1971. However, GaN is naturally n-type and it proved impossible, at the time, to grow p-type layers so that research in the field was nearly abandoned. The first p-type layer was successfully demonstrated in 1989 by activating Mg acceptors in GaN using Low Energy Electron Beam Irradiation (LEEBI)[4] and interest in GaN was revived. Figure 1-1 shows the increase in the volume of nitride publications since 1989. In 1990, S. Nakamura developed the two-flow, Metal-Organic Vapour Phase Epitaxy (MOVPE) reactor which greatly improved the quality of the GaN epilayers and also discovered that annealing in N_2 was a better alternative to LEEBI for activating Mg dopants[5]. These breakthroughs led to the fabrication and commercialisation of blue GaN based LED (1993) and LDs (1999).

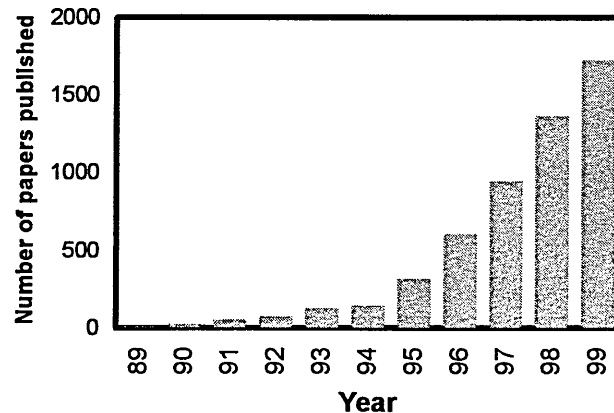

Figure 1-1: number of publications in the gallium nitride field during the last 10 years.

One of the main technological steps in device fabrication lies with the formation of metal contacts to connect the device to the outside world. Ideally, Ohmic contacts should be of low resistance and Schottky contacts should exhibit very little reverse current with forward current dominated by thermionic emission. Additionally, both types of contact need to be thermally stable, especially in the case of GaN, which is a promising material for devices operating at high temperature. Metal contacts constitute a critical parameter of device performance, as contact degradation is often a cause of device failure. Furthermore, as device integration intensifies, device behaviour is increasingly governed by the physical properties of junctions and interfaces rather than bulk properties. It is therefore crucial to understand how metal contacts are formed. We mentioned earlier that GaN is mainly used for optoelectronics applications such as blue LEDs and LDs, for which good Ohmic contacts is a crucial requirement. Additionally, the wide band gap of GaN means that it remains extrinsic even at high temperature, which makes it interesting for high power, high frequency microelectronics. Devices such as High Electron Mobility Transistor (HEMT) and Metal Semiconductor Field Effect Transistor (MESFET) require reliable and reproducible high barrier Schottky contacts for the gate metallisation. This Schottky contact governs the flow of electrons in the channel from the source to the drain and is therefore central to device operation. Schottky contacts are also used in GaN based Ultra-Violet photodetectors[6,7].

Metal semiconductor contacts can be broadly divided into two categories: practical (real) contacts and intimate contacts. Practical contacts are the norm in device manufacture. Before the formation of a practical contact, the semiconductor substrate is subjected to wet chemical treatments in order to remove surface contaminants. However, the substrates are exposed to air between surface treatment and metal deposition so that there is always a thin layer of native oxide remaining on the surface as well as carbon and water vapour contamination. This insulating layer is thin enough for electrons to tunnel through it, but is thick enough to ensure that the contact properties are governed by the insulator-semiconductor interface[8]. The semiconductor surface is therefore decoupled from the metal. Intimate contacts are formed on atomically clean surfaces, which can be prepared in an ultra high vacuum (UHV) environment, either by cleaving a crystal in order to expose a clean surface or by *in-situ* cleaning techniques such as ion bombardment or annealing. Alternatively, metals can be deposited directly after epitaxial growth. Intimate contacts are free of the amorphous

interfacial layer so that metal and semiconductor can interact. This results in a more complex interface because of a range of factors such as chemical reactions between metal and semiconductor, metal atom in-diffusion, semiconductor atom out-diffusion or structural changes at metal-semiconductor interface.

As GaN is a relatively new material, the formation of metal contacts to GaN is less well understood than for more established semiconductor materials such as Si or GaAs. In particular, we will see in Chapter 2 that surface treatments prior to metallisation, both *ex-situ* and *in-situ,* play an important role in the behaviour of the contact. During the course of this work, two major experiments were performed with the aim of achieving a better understanding of the influence of GaN surface preparation on the properties of rectifying metal-GaN contacts. The first experiment is a soft x-ray photoemission spectroscopy (SXPS) and x-ray photoemission spectroscopy (XPS) investigation of three different surface preparations. The amount of C and O contamination at the surface and surface band bending are compared. Additionally, Ag contacts, deposited on the least contaminated surface are characterised by current-voltage (I-V) measurements and the results are compared to the photoemission results. The second experiment is an extensive XPS, I-V and transmission electron microscopy (TEM) study of Au contacts deposited on the three GaN surfaces studied during the first experiment. Au was chosen because its excellent electrical conductivity and resistance to oxidation means it is widely used in devices. Au, because of its high work function, is expected to form a Schottky contact to nGaN. We have seen that reliable and reproducible high barrier Schottky contacts are crucial to the operation of GaN based HEMTs and MESFETs. During the experiment Au was deposited in steps of increasing thickness from sub-monolayer coverage to thick blanket coverage so that the initial stages of contact formation were monitored by XPS while the final contacts were characterised by I-V and cross-sectional TEM. This work therefore combines and compares results from three fundamentally different techniques for the first time in the field of metal–GaN contacts.

The organisation of the thesis is as follows:

- Chapter 2 is a brief review of the work done to date on the topic of metal-GaN contacts.
- Chapter 3 describes the many models put forward over the years in a attempt to predict the behaviour of metal semiconductor contacts and provides the relevant

theoretical background of current transport mechanisms across a metal-semiconductor interface.

- Chapter 4 gives a description, both theoretical and practical, of the experimental techniques used in the course of this research.
- Chapter 5 presents the results of the photoemission study of three GaN surface treatments, together with a I-V characterisation of Ag-GaN contacts formed on one of the surfaces.
- Chapter 6 focuses on the XPS and I-V investigation of the formation of Au contacts onto the three GaN surfaces studied in the previous chapter.
- Finally, Chapter 7 summarises the important conclusions of the work and suggests programmes of future research in this area.

Chapter 2: Literature review

As seen in Chapter 1, metal-semiconductor contacts can be divided in two broad categories, namely practical contacts and intimate contacts. Practical metal contacts to GaN have been studied quite extensively while publications on atomically clean GaN surfaces and intimate contacts to GaN are fewer. These contacts are often investigated by surface sensitive techniques such as XPS, which give more insight into the interface formation mechanisms. Conversely, practical contacts are mostly characterised by transport and capacitance measurements.

In this chapter, we first review practical metal contacts to GaN, Ohmic contacts to n and p-type GaN and Schottky contacts to n-type GaN. The second part of the chapter summarises results from previous work on clean GaN surfaces and intimate metal contact formation.

2.1 Practical contacts

2.1.1 Ohmic contacts to nGaN

Table 2-2 presents the contact resistivity ρ_c of different metallisation schemes on nGaN. The donor concentration and anneal conditions are also given. It can be seen that most of the Ohmic contacts involve low work function metals, mainly Al and Ti. The work function of the various metal used in the studies presented in this chapter are given in Table 2-1. The Ohmic behaviour of Al and Ti contacts is thought[9] to come from their low work functions combined with the formation of a very thin layer of AlN and TiN at the interface upon annealing. This increases the density of N vacancies, therefore creating an interfacial layer of highly doped GaN.

Metal	Pt	Ni	Pd	Au	Cu	W	Cr	Ti	Al	Ag	Ga	Mg	Cs
Work function (eV)	5.65	5.15	5.12	5.1	4.65	4.55	4.5	4.33	4.28	4.26	4.2	3.66	2.14

Table 2-1: work functions of selected metals (ref. 8).

Another mechanism put forward[10] suggests that the Ohmic behaviour is due to the reduction of the native oxide (Ga_2O_3) by the highly reactive Ti and the formation of an Ga-Ti intermetallic alloy with a low work function coming into intimate contact with the GaN surface. These two metals, however, oxidise easily even at room temperature, which results in increased contact resistivity. To avoid this oxidation, the contacts are often coated with a Ni/Au bilayer, hence enhancing temperature stability. W and WSi_x[22,11] contacts exhibited superior thermal stability compared to other contacts. Lee *et al.* [12] compared Ti/Al/Au and Ti/Al/Pt/Au contacts and found that the Pt layer acted as an effective barrier to prevent Au in-diffusion and improved the thermal stability.

Metallisation	ρ_c (Ωcm^2)	N_d (cm^{-3})	Anneal conditions	Ref.
Al	$\approx 10^{-3}$-10^{-4}	3×10^{18}	575°C, 10 min	13
Au	$\approx 10^{-3}$-10^{-4}		575°C, 10 min	
$PtIn_2$	1.2×10^{-2}	5×10^{17}	No anneal	14
	$<1\times10^{-3}$		800°C, 1 min, Ar	
Ti/Ag (15/150nm)	6.5×10^{-5}	1.7×10^{19}	No anneal	15
Ti/Al (35/115nm)	4×10^{-6}	7×10^{17}	600°C, 15 s, Ar	16
Pd/Al (25/125nm)	5×10^{-5}		600°C, 30 s, Ar	
Ta/Al (35/135nm)	6×10^{-5}		600°C, 30 s, Ar	
Ti/Al/Ni/Au (15/220/40/50nm)	1.19×10^{-7}	2×10^{17}	900°C, 30 s	17
	8.9×10^{-8}	4×10^{17}	900°C, 30 s	
	3.3×10^{-6}		No anneal	
Al	9×10^{-5}	2.8×10^{17}	No anneal	18
Ti/Al (25/100nm)	6×10^{-6}		550°C, 30 s	
Ti/Al (20/100nm)	8×10^{-6}	1×10^{17}	900°C, 30 s	19
Ti/Al	10^{-5}	3×10^{19}	No anneal	20
Ti/Au (3/300nm)	3.6×10^{-8}	4×10^{20}	No anneal	21
W (50nm)	8×10^{-5}	1.5×10^{19}	600°C, 1 min, N_2	22
Nd/Al	8×10^{-6}	1×10^{18}	250°C, 5 min; 600°C, 30 s	23
Cr/Al	3.8×10^{-5}	2×10^{17}	600°C, 2 min, vacuum	24
	5.2×10^{-4}	1.1×10^{18}	1200°C, 2 min, vacuum	
Cr/Al/Ni/Au	4.7×10^{-5}	2×10^{17}	700°C, 2 min, vacuum	
	2.4×10^{-5}	1.1×10^{18}	950°C, 2 min, vacuum	
InN/GaN superlattice	6×10^{-5}	5×10^{18}	No anneal	25

Table 2-2: contact resistivity of various metallisation schemes on nGaN. For multilayer contacts, the order of deposition is from left to right.

The lowest specific contact resistivity[21] reported is 3.6×10^{-8} Ωcm^2 for non-annealed Ti/Au contacts (3/300 nm) on Si implanted nGaN. This very low contact resistivity is likely to be due to the high doping density of about 4×10^{20} cm^{-3}. Another study[20] on Si implantation (donor concentration of 3×10^{19} cm^{-3}) reported a specific

contact resistivity of 10^{-5} Ωcm^2 for non-annealed Ti/Al contacts. Both these studies required high temperature pre-metallisation anneals (1150°C and 1120°C) in order to activate the implanted Si.

Use of a InN/GaN short period superlattice is an alternative technique requiring no anneals to the standard Ti/Al bilayer. Quantum tunnelling through the superlattice conduction band was suggested[25] to be responsible for the effective barrier lowering leading to the low resistivity.

2.1.2 Ohmic contacts to pGaN

Low resistance Ohmic contacts to pGaN represent a greater challenge than n-type, mainly because of the difficulty[9] to achieve hole concentrations greater than about 5×10^{18} cm^{-3}. Table 2-3 presents a compilation of the various results obtained so far.

Metallisation	$\rho_c(\Omega cm^2)$	p (cm^{-3})	Anneal conditions	Ref.
Ni/Au (10/40 nm)	10^{-2}	3×10^{17}	500°C, vacuum	26
Pd/Au (20/500 nm)	4.3×10^{-4}	3×10^{17}	No anneal	27
Ta/Ti (60/40 nm)	3.2×10^{-5}	7×10^{17}	800°C, 20 min, vacuum	28
Pt (70 nm)	1.5×10^{-2}	4.6×10^{17}	600°C, 1 min, N_2	29
Ni/Pt (50/100 nm)	1.8×10^{-2}			
NiIn (80 nm)	$8\text{-}9\times10^{-3}$	2×10^{17}	800°C, 1 min, N_2	30
Ni/Au (20/100 nm)	$1.2\text{-}2.1\times10^{-2}$		750°C, 1 min, N_2	
Pt_3In_7 (150 nm)	9.5×10^{-2}	1.7×10^{17}	800°C, 1 min, N_2	31
Ni/Au (10/5 nm)	$<10^{-4}$	2×10^{17}	400°C, 10 min, air	32
Pt/Ni/Au (20/30/80 nm)	5.1×10^{-4}	3×10^{17}	350°C, 1 min	33

Table 2-3: comparison of contact resistivity for various metallisation schemes to p-type GaN. In ref. 29, Pt was electro-deposited.

The first systematic study of practical contact to p-type GaN was conducted by Ishiwaka *et al.*[26], investigating a wide range of metals, Ni, Ta, Au, Ti, Al, Cu, Pd, and Pt; Ni/Au was a standard used for comparison. The metals were deposited on GaN substrates previously treated in a buffered HF solution. They found that contact resistance decreased exponentially with increasing metal work function, seemingly

indicating that the Fermi level is not pinned at pGaN surfaces. Additionally, removal of the native oxide layer did not significantly improve the contacts while the standard Ni/Au bilayer exhibited the lowest contact resistivity. The main implication of this study is that large work function metals are desirable for Ohmic contact on pGaN.

This has been repeatedly confirmed by later experiments, except for the Ta/Ti bilayer as shown in Table 2-3. These two low work function metals formed the lowest contact resistivity reported to date, because of their strong binding energy with hydrogen atoms[28] which are known to inhibit Mg acceptors in GaN[5]. This characteristic facilitates out-diffusion of H atoms from the GaN and therefore increases the ionisation efficiency of the Mg dopants upon annealing.

Kim *et al.*[27] reported the only non-annealed Ohmic contact using a Pd/Au bilayer deposited after substrate cleaning in *aqua regia* which improved the contact resistivity from 2.9×10^{-2} Ωcm^2 to 4.3×10^{-4} Ωcm^2. Removal of surface oxide was put forward as an explanation for the improvement. Electrodeposited Pt contacts[29] yielded better contact resistivity than sputtered contacts, again possibly because of a more intimate contact.

Ho *et al.*[32] attributed the low contact resistivity of their Ni/Au contacts ($<10^{-4}$ Ωcm^2) to the heat treatment in ambient air, which caused oxidation of the Ni film. They argued that the NiO films formed by oxidation of Ni were p-type with a high carrier concentration, therefore acting as a low barrier, interfacial semiconductor layer and lowering the contact resistivity compared to the conventional Ni/Au contacts. This interpretation was refuted by Maeda *et al.*[34]. They deposited Li doped NiO layers with resistivity lower than that of pGaN before the Au layer and found that this did not improve contact resistivity.

2.1.3 Schottky contacts to nGaN

The abrupt end of the three dimensional periodic structure of the crystalline lattice at the surface of a semiconductor causes major perturbations in the valence states of surface atoms in covalent semiconductor like silicon but has little effect on ionic compounds[35]. These surface states lead to Fermi level pinning at the surface of covalent semiconductors but the ionic nature of the GaN bonds suggests little or no Fermi level pinning, therefore the Schottky barrier height of metal-GaN contacts may be expected to depend on the metal work function. Barrier heights of a variety of rectifying metal

contacts to nGaN reported in the literature are plotted as a function of metal work function in Figure 2-1. The plot shows that, within experimental error, the barrier height does indeed increase with increasing work function. The work function dependence is however not as strong as predicted by the Schottky-Mott model, which suggests the presence of surface states. The work function dependence of the barrier height, given by the index of surface behaviour S (or slope factor), can provide an estimate of the density of surface states (see section 3.1.7). Schmitz *et al.*[44] calculated a S value of 0.385 (as opposed to 1 for the ideal Schottky-Mott case) from measurements taken on 7 metals, which corresponds to a surface state density D_S of about 1.6×10^{13} $cm^{-2}eV^{-1}$. An earlier experiment[42] conducted on GaN grown on a different substrate and using a different surface treatment yielded S=0.97 which corresponds to $D_S\approx3\times10^{11}$ $cm^{-2}eV^{-1}$. Surface treatment, choice of substrate and lattice polarities may influence the electrical properties of metal-GaN contacts. The different growth methods and surface treatments employed in the experiments of Figure 2-1, given in Table 2-4, might therefore account for the wide spread in values.

Koyama *et al.*[46] studied the influence of pre-deposition surface treatment on the electrical characteristics of Ag, Au and Pt contacts on nGaN. They found that diodes formed after cleaning in organic solvents only exhibited poor linearity and high ideality factors, while those formed after an HF/HCl treatment were nearly Ohmic. On the other hand, diodes formed after cleaning in a warm NH_4OH solution exhibited near ideal electrical behaviour but no systematic dependence of the barrier height on the metal work function was found. By contrast, barrier heights for metal contacts (Sn, Ni and Au) electrodeposited[36] on nGaN were strongly dependent on the metal work function, with a slope factor S=0.49. These results were explained from the viewpoint of the disorder induced gap states model.

Study	GaN growth	n (cm^{-3})	Surface treatment
Hacke *et al*[37]	MOCVD on Al_2O_3	6.6×10^{16}	Boiling *aquia regia*
Binari *et al*[38]	MOVPE on Al_2O_3	4×10^{17}	O_2 plasma+ NH_4OH:H_2O
Guo *et al*[39]	LP-MOCVD on Al_2O_3	2×10^{17}	Buffered Oxide Etch
Mohammad *et al*[40]	MBE on Al_2O_3	5×10^{16}	Boiling *aquia regia*
Wang *et al*[41]	MOCVD on Al_2O_3	10^{17}	Buffered Oxide Etch
Kalinia *et al*[42]	MOCVD on SiC	6×10^{17}	KOH:H_2O solution
Kribes *et al*[43]	MBE on Al_2O_3	7×10^{17}	Boiling *aquia regia*
Schmitz *et al*[44]	LP-MOCVD on Al_2O_3	10^{17}	Oxygen plasma asher + HCl solution
Liu *et al*[45]	MOVPE on Al_2O_3	10^{17}	HCl:H_2O solution
Koyama *et al*[46]	MBE on Al_2O_3	$5\text{-}7\times10^{16}$	NH_4OH solution at 50°C

Table 2-4: GaN layers growth details and surface treatments used in the various studies of Figure 2-1. Solvent degreasing (organic treatment) was also conducted before (and sometimes afterwards) the surface treatments mentioned.

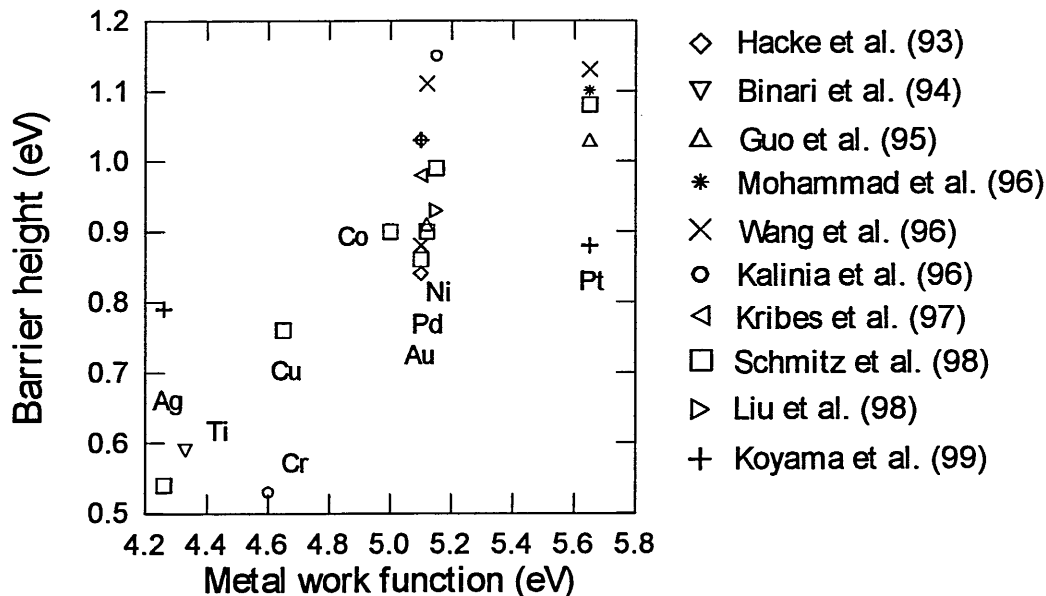

Figure 2-1: reported barrier heights of practical metals/nGaN contacts versus metal work function. The metals have been vacuum deposited and the barrier heights have been extracted by current-voltage measurements. The ideality factors were close to unity.

2.2 Intimate contacts

As opposed to practical contacts, intimate contacts are formed on atomically clean semiconductor surfaces by making use of UHV systems. The absence of interfacial oxide layer means that metal and semiconductor can interact freely and the resulting interfaces may be more complex than the practical contacts.

2.2.1 Clean GaN surfaces

Unless metal deposition occurs *in-situ* after epitaxial growth or on a cleaved crystal facet (which is not yet possible for GaN) it is necessary to prepare atomically clean surfaces in order to study the formation of intimate contacts. This is usually achieved by an *ex-situ* surface treatment similar to that of a practical contact followed by *in-situ* processing in UHV.

The most efficient chemical etches, in term of removing carbon and oxygen contamination, seem to be HF and HCl solutions[47]. Annealing in UHV alone reduces further the amount of oxygen and carbon but complete removal does not occur at temperature below 950°C, at which point the GaN layer starts to decompose[47]. Annealing in NH_3 at 700-800°C has been shown to produce atomically clean, as well as stoichiometric surfaces[47]. Several groups[48,49,50,51] have reported clean surfaces obtained by annealing at 900°C in a gallium flux or by desorbing at 900°C several monolayers of gallium previously evaporated at room temperature. It is thought that gallium atoms react with oxygen while carbon "floats" to the surface of the metal and that both are then evaporated during the 900°C anneal[52]. Wu and Kahn[53] used a repeated nitrogen sputtering and annealing steps at 900°C to prepare clean and ordered GaN (0001)-(1×1) surfaces. They performed the last annealing steps in 10^{-7} torr N_2 to improve the Ga to N ratio. Argon sputtering has been shown to induce a loss of nitrogen at the surface, which resulted in the formation of metallic gallium[54]. Bermudez[52] compared nitrogen-ion sputtering and Ga metal deposition and desorption, and found that both methods produce equivalent clean surfaces.

Ga3d binding energy	VBM binding energy	Band bending	Electron affinity	Work function	Additional information	Ref.
20.3±0.2	2.4±0.2	0.9±0.2	3.2±0.2		Clean nGaN (1×1)	52
		0.4±0.2			Etched nGaN	
20±0.2	2.1±0.2	1.2±0.2			Clean nGaN (3×3)	55
20.7	3.5±0.1	≈0			nGaN	54
20.8±0.1	2.6±0.1	0.75±0.1	3.5±0.1	4.3±0.1	Clean nGaN (1×1)	53
19.3±0.1	1.0±0.1	-0.75±0.1	3.5±0.1	5.9±0.1	Clean pGaN (1×1)	
	2.94	0.48	3.35±0.1	3.88±0.15	Clean nGaN	56
	3.22	-3.18	3.35±0.1	3.6±0.15	Clean pGaN	
		2.2			nGaN	57

Table 2-5: clean surface parameters measured by XPS and UPS. All values are in eV. Binding energies are referenced to the Fermi level. The work functions from ref. 56 were measured using a Kelvin probe.

The GaN surfaces used in these studies were cleaned using the different methods mentioned above, except for references 54 and 57 where the GaN surfaces were only annealed at 900°C. The surface reconstruction patterns were obtained by low-energy electron diffraction and reflection high-energy electron diffraction. The (3×3) reconstruction[55] was observed during MBE growth, and XPS scans performed *in-situ* after growth on this layer showed a significant amount of relaxed metallic gallium on the surface. This has not been observed on cleaned surfaces studied in the other works presented. Several surface reconstructions have been observed during MBE growth[58], depending on lattice polarity, temperature and Ga to N ratio at the surface. It has been shown that the 2 lattice polarities, corresponding to growth on the (0001) face and the (000$\bar{1}$), are associated with 2 different groups of surface reconstructions[58].

Band bending at the surface is an important parameter since it directly affects the final barrier height of metal contacts. Table 2-5 shows that the nGaN bare surface, except in one case[54], exhibits upward band bending. Bermudez compared atomically

clean and practical surfaces and found that the band bending at the practical surface (cleaned in NH_4OH) is significantly less than at the clean surface[52]. In contrast, Wu *et al.*[53] observed a decrease in band bending of about 0.4 eV as the surface became clean. p-type GaN surfaces exhibit downward band bending, although the two studies cited in Table 2-5 report very different values. Wu *et al.*[53] found that band bending at clean p-type surfaces is of the same magnitude as that of the n-type surfaces indicating the presence of a depletion layer at both surfaces. On the other hand, Eyckeler *et al.*[56] reported a strong inversion layer at their p-type surfaces. The surface states responsible for the band bending have not been identified.

2.2.2 Metal contacts

Table 2-6 summarises the barrier heights of intimate contacts obtained by different groups. It can be seen that barrier height values differ considerably, from practical to intimate contacts, for the same metal. For example, low work function metals such as Al and Ti, which make non-rectifying practical contacts, are found to induce significant barrier heights when deposited on atomically clean surfaces. Several comments can be made about this fact, arising from both the measurement methods and the actual interface formation mechanisms:

- The metal contacts investigated by XPS are very thin, typically 20-50Å, compared to the practical contacts measured by I-V (>1000 Å). There is no certainty that the interface remains the same as the film thickness increases.
- As shown in Table 2-6, the initial band bending of the bare surface accounts for a significant part of the total barrier height. Atomically clean surfaces can be expected to exhibit different band bending to practical surfaces.
- I-V measurements tend to yield lower barrier because of the image force lowering and other bias dependant effects.
- If the interface presents local variations of the barrier height, XPS measurements will yield an average value while the I-V method will only "see" the lowest value because of electron flow mechanisms across the barrier.

Metal work function (eV)	Bare surface barrier height (eV)	Barrier height (eV)	Doping (cm^{-3})	Reference
Pt (5.65)	0.75±0.1	1.65	n=1×10^{19}	59
	0.75±0.1	0.9	p=5×10^{17}	
Ni (5.15)	0.9 ±0.2	2.2	n	52,60
Au (5.1)	0.75±0.1	1.25	n=1×10^{19}	59
	0.75±0.1	1.2	p=5×10^{17}	
	2.2	1.15	n	57
Ti (4.33)	0.75±0.1	1.25	n=1×10^{19}	59
	0.75±0.1	1.55	p=5×10^{17}	
Al (4.28)	0.75±0.1	0.7	n=1×10^{19}	59
	0.75±0.1	0.7	p=5×10^{17}	
	0.9 ±0.2	1.4	n=2×10^{17}	52,61
Ag (4.26)		0.7	n<1×10^{16}	50
Pb (4)		0.72	n<1×10^{16}	
Mg (3.66)	0.75±0.1	0.65	n=1×10^{19}	59
	0.75±0.1	1.9	p=5×10^{17}	
	0.7 ±0.2	0.8	n=7.3×10^{17}	62
Cs (2.1)	0.48	0.2±0.15	n=5×10^{16}	56
	3.18	3.2±0.15	p=1.2×10^{17}	

Table 2-6: Barrier heights of various intimate metal contacts to GaN. All values are in eV except carrier concentrations (cm^{-3}). The bare surface barrier heights have been obtained by UPS, while the final barrier heights are extracted from XPS except ref. 50 (I-V).

Wu and Kahn[59] conducted the most extensive study, investigating 5 metals on atomically clean n and p-type GaN. They found that Mg, Al and Ti reacted with GaN while Pt and Au formed abrupt interfaces. The high work function metals (Pt and Au) led to higher barrier heights on n-type GaN than low work function Mg and Al, and to lower barrier heights on p-type GaN than Mg and Ti. This behaviour tends to confirm the Schottky Mott model and seem to rule out any Fermi level pinning. Ti and Al, however behave differently despite having similar work functions: Ti contacts resulted

in a similar barrier as Au on n-type GaN while Al depositions on both n and p type did not induce further significant band bending. The authors pointed out that Al reacts with GaN to form AlN, which is a near insulator (band gap of 6.2 eV) so that the interface consists of a metal-insulator-semiconductor structure and therefore the metal induced states are decoupled from the semiconductor. On the other hand, Ti reacts with GaN to form TiN, which is a metallic compound; hence the discrepancy between the two metals.

Bermudez investigated three metals, Mg[62], Al[61] and Ni[60] on n-type GaN, and also found that the barrier height increases with increasing metal work function. He recently[63] put forward the simple Cowley-Sze[64] model, in which the barrier height is expressed as a sum of the "bare surface barrier height" or band bending before metal deposition, and a Schottky-Mott term induced by the metal. This model generally agrees well with experimental results except for the Au contact studied by Sporken *et al.*[57], in which the Au deposition caused the bands to bend in the opposite way of that predicted by the Schottky-Mott model.

Kampen and Mönch[50] devised the MIGS-and-electronegativity model to describe metal contact formation on nGaN. According to this model, the barrier height of ideal semiconductor arises from the position of the charge neutrality level of the MIGS within the band gap, and the electronegativity difference between metal and semiconductor. They found that predictions from this model were in very good agreement with experimental results for Ag, Pb[50] and Cs[56] on nGaN.

2.3 Summary

In this chapter, practical and intimate metal contacts to GaN have been reviewed. Practical contacts have been mostly characterised using transport measurements while XPS was the main tool used for the investigation of intimate contacts.

The barrier height dependence of practical metal contacts to GaN on the metal work function is now well established. Low work function metals are used for Ohmic contacts to n-type GaN while high work function metals resulted in lower barriers on p-type. The standard Ohmic metallisation schemes for n and p-type GaN are Ti/Al and Ni/Au bilayers, respectively. The specific contact resistance of Ohmic contacts to n-type is low enough for device applications but improvements are still needed for contacts to p-type material. The barrier heights of Schottky contacts to nGaN increases with

increasing metal work function but also vary significantly with surface preparation and other parameters such as lattice polarity and choice of substrate for the GaN layer. The simple Schottky-Mott model does not, in most cases, give an accurate prediction of the barrier height.

Studies of intimate contacts show that, as for practical contacts, high work function metals lead to high barriers on n-type and low barriers on p-type GaN. The opposite also seems to be true for low work function metals. However, most metals resulted in a much higher barrier when deposited onto an atomically clean nGaN surface than onto a practical surface. This difference is partly attributed to different measurement techniques (transport measurement and photoemission spectroscopy) and to upward band bending on the clean surface induced by the cleaning processes which usually involve high temperature anneals in UHV. The two main models put forward are the Cowley-Sze and the MIGS-and-electronegativity models.

Chapter 3: Theory of metal-semiconductor contacts

This chapter is divided in two main sections. The first section presents the various models of metal-semiconductor formation put forward in an attempt to describe experimental data, including the main models and less known models which have been specifically used to interpret contacts to GaN. The second part provides the relevant theoretical background of current transport mechanisms across a metal-semiconductor interface and various methods used to extract the barrier height.

3.1 Models of metal-semiconductor contact formation

3.1.1 The Schottky-Mott model

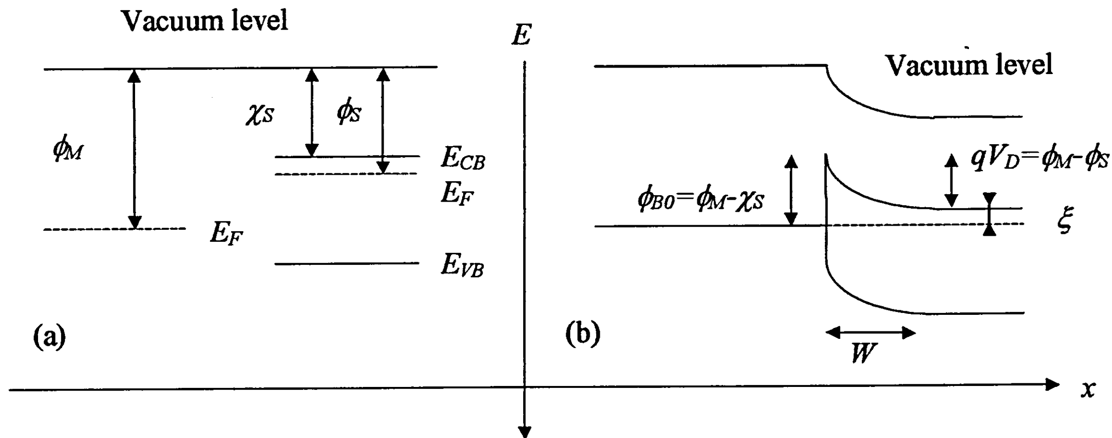

Figure 3-1: energy band diagram of the formation of a barrier between a metal and semiconductor : (a) isolated, (b) in perfect contact.

Figure 3-1 shows the mechanism of a Schottky contact formation according to the Schottky-Mott model. Before contact, the metal is characterised by its Fermi level E_F and its work function ϕ_M, which is the energy needed to remove an electron from the Fermi level to the vacuum level. In a semiconductor, it is more convenient (and more realistic, as there are no electrons at the Fermi level energy) to use the electron affinity χ_S, which is the energy needed to remove an electron from the bottom of the conduction band.

When the two are placed into contact, assuming the parameters of Figure 3-1 (n-type GaN and $\phi_M > \phi_S$), electrons move from the semiconductor into the metal in order to equalise their Fermi levels. This results in an excess positive charge at the semiconductor surface due to ionised donors. The semiconductor surface is said to be depleted and this depletion zone extends to a depth W into the bulk. As the interface must be neutral there is also an excess negative charge at the metal surface, but because the electron concentration in the metal is much greater than the donor concentration in the semiconductor, the charges are confined in a much smaller depletion zone (typically within 1Å). The bands in the semiconductor are then bent upwards and the resulting

zero-bias barrier height ϕ_{B0} is, as shown on Figure 3-1 (b), the difference between the metal work function and the electron affinity of the semiconductor:

$$\phi_{B0} = \phi_M - \chi_S$$

[3-1]

with:

$$\chi_S = \phi_S - \xi$$

[3-2]

and:

$$\xi = E_{CB} - E_F = \frac{kT}{q} \ln \frac{N_C}{N_D}$$

[3-3]

where N_C and N_D are respectively the effective density of states in the conduction band and the donor concentration, k is the Botzmann constant, T the temperature and q the elemental electronic charge.

If $\phi_M < \phi_S$ then electron transfer takes place from the metal to the semiconductor and the bands bend downward forming an Ohmic or linear contact (Figure 3-2 (b)). When such a contact is biased, electrons encounter no barrier flowing from the semiconductor to the metal and the reverse direction current is eased by the high concentration of electrons in the region where the bands are bend downward. The resistance of the contact is then negligible compared to that of the semiconductor bulk.

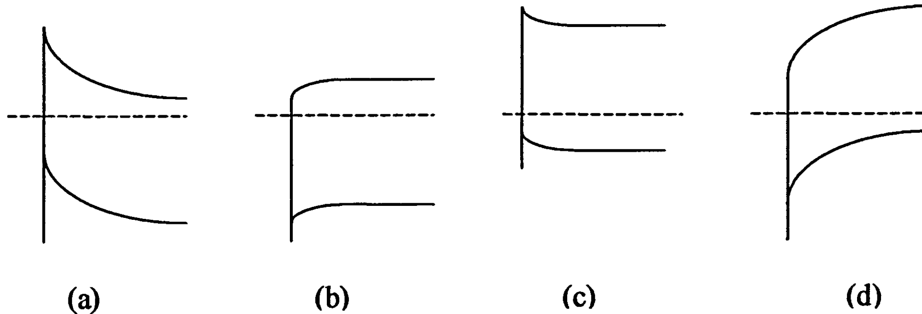

Figure 3-2: band bending at the interface for n-type semiconductor with : (a) $\phi_M > \phi_S$, (b) $\phi_M < \phi_S$ and p-type :(c) $\phi_M > \phi_S$, (d) $\phi_M < \phi_S$.

Because of the nature of holes, contacts on p-type semiconductors give rise to rectification when $\phi_M < \phi_S$ and to linearity when $\phi_M > \phi_S$ as shown on Figure 3-2 (d) and

(c), respectively. In practice, however, situations depicted in Figure 3-2 (b) and (c) (Ohmic contacts) are rarely encountered[8].

In the case of a rectifying contact on a n-type semiconductor and assuming that the interface is chemically inert and there are no surface states, Poisson's equation leads to the expressions of the potential $\psi(x)$ (relative to the Fermi level) and the depletion width W[65] :

$$\frac{d^2\psi}{dx^2} = -\frac{\rho}{\varepsilon} \Rightarrow |E(x)| = -\frac{d\psi}{dx} = \frac{qN_D}{\varepsilon}(W-x)$$
$$\Rightarrow \psi(x) = \frac{qN_D}{\varepsilon}\left[Wx - \frac{x^2}{2}\right] - \phi_{BO}$$

[3-4]

$$\Rightarrow W = \sqrt{\frac{2\varepsilon}{qN_D}(V_D - V)}$$

[3-5]

Where $\rho=qN_D$ is the depletion charge in the semiconductor, N_D the donor concentration, V_D the built-in diffusion potential and ϕ_{BO} the zero-bias barrier height. V is the positive (forward) applied bias.

When a forward bias is applied to a rectifying contact the diffusion potential V_D is lowered and the band bending attenuated (Figure 3-3 (a)). When the applied bias is equal to the diffusion potential the bands are not bent anymore and the depletion zone disappears ($V=V_D$ in equation [3-5]). This is the flat-band case (Figure 3-3 (c)). Equation [3-5] leads to the total charge and capacitance in the depletion zone:

$$Q_{SC} = qN_D W = \sqrt{2q\varepsilon N_d(V_D - V)}$$

[3-6]

$$\Rightarrow C = \frac{\partial Q_{SC}}{\partial V} = \sqrt{\frac{q\varepsilon N_D}{2(V_D - V)}} = \frac{\varepsilon}{W}$$

[3-7]

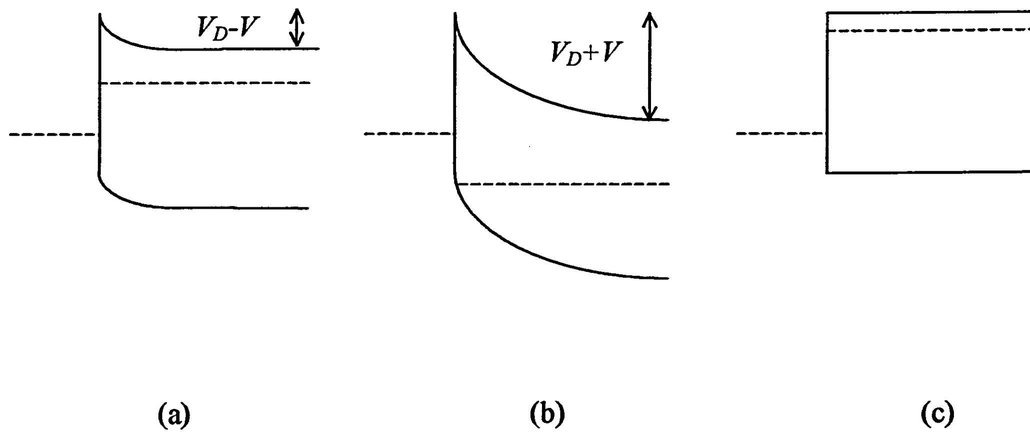

Figure 3-3: (a) forward biased contact, (b) reverse biased contact, and (c) flat-band case.

3.1.2 The Bardeen model

The Schottky-Mott model does not take into account the thin insulating layer of oxide between the semiconductor and the metal or the presence of surface states, which are both part of a real metal-semiconductor contact as shown on Figure 3-4[8]. The interface layer is usually so thin (10-20 Å) that electrons tunnel through it quite easily and the Schottky-Mott relation is still valid.

The surface states contribution to the barrier height cannot, however, be neglected in most cases. At the surface, atoms have neighbours on one side only and the valence electrons on the vacuum side cannot form a covalent bond. These unpaired electrons ('dangling bonds') act either as donors or acceptors, creating two surfaces states per surface atom. Surface charge neutrality requires that half of these surface states should be filled, or, in other words, that the Fermi level at the surface should coincide with the neutrality level ϕ_0 of the surface states. States below ϕ_0 are called donor-like (positive when empty and neutral when full) while states above ϕ_0 are acceptor-like (neutral when empty and negative when full).

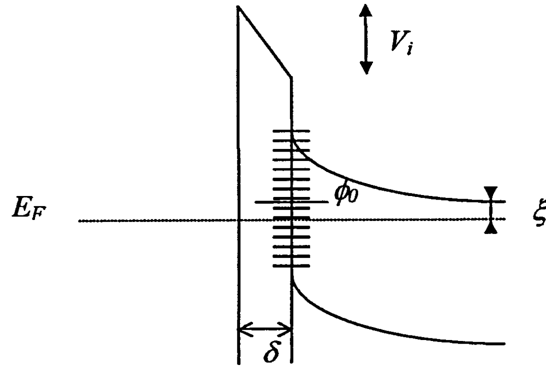

Figure 3-4: real metal semiconductor contact with surface states and insulating layer.

The neutrality condition of the junction is then $Q_m+Q_{sc}+Q_{ss}=0$ where Q_m is the charge in the metal and Q_{ss} in the surface states. If the Fermi level (constant throughout the junction at zero-bias) is below the neutral level, as shown in Figure 3-4, then there is a net positive charge at the interface which means that the charge in the semiconductor depletion zone is smaller than it would be in the absence of surface states. This in turn implies that the diffusion potential, and therefore the barrier height are also reduced. The reduction of the barrier height pushes ϕ_0 down towards E_F. Similarly, if the Fermi level is above the neutral level then there is a negative charge at the interface, the barrier height is increased and ϕ_0 is pulled up towards E_F. In both cases the surface states tend to drag the Fermi level towards the neutrality level. If the density of states is very high then $\phi_0 \approx E_F$ and the barrier height is given by:

$$\phi_{B0} \approx E_g - \phi_0$$

[3-8]

The Fermi level is then independent of the metal and is said to be pinned[8]

If a voltage is applied to the junction described in Figure 3-4 so that the flat-band situation is reached, then the neutrality equation becomes $Q_m+Q_{ss}=0$. It is then possible to derive an equation for the flat-band barrier height (ϕ_{BF}), uniting the Schottky-Mott model and the Bardeen model :

$$\phi_{BF} = \gamma(\phi_M - \chi_S) + (1-\gamma)(E_g - \phi_0)$$

[3-9]

with

$$\gamma = \frac{\varepsilon_i}{\varepsilon_i + q\delta D_S}$$

[3-10]

where ε_i is the permittivity of the interfacial layer, δ the interfacial layer thickness and D_s the density of surface states ($cm^{-2}eV^{-1}$). When D_s is very small then $\gamma \approx 1$ and the barrier height is given by the Schottky-Mott theory (equation [3-1]). On the other hand, for a very high density of states the barrier height is given by the Bardeen model (equation [3-8]) and is independent of the metal work function.

3.1.3 Intimate contacts

Contacts with a thin oxide layer between metal and semiconductor are the norm in commercial devices, but this does not alter the performances of the devices as the interfacial layer is very thin (10-20 Å). The semiconductor surface is, however, decoupled from the metal and the interface states arise mostly from the oxide-semiconductor interface. It is possible to evaporate metal contacts on atomically clean surfaces where the metal will contribute to the interface states. The semiconductor surfaces are usually cleaned of any possible contamination (mainly oxygen and carbon) by annealing in an UHV environment or by ion sputtering. Alternatively, the metal might be deposited *in-situ* on a cleaved facet or just after growth by MBE.

In any case, intimate contacts are free from an insulating interfacial layer and the metal can interact with the clean semiconductor. Diffusion of metallic atoms into the semiconductor or out-diffusion of semiconductor atoms onto the metal overlayer may occur, as well as chemical reactions resulting in a layer of compound at the interface.

It is also possible for the wave functions of those electrons in the metal with energies corresponding to the forbidden gap in the semiconductor to penetrate into the semiconductor in the form of evanescent waves. As the attenuation length of the electron wave functions is of the order of a few Angstroms, the transfer of charge from the metal is confined at the interface, hence creating new interface states. Intrinsic electron states, which might have been present at the semiconductor surface will then be replaced by these metal induced gap states (MIGS)[66]. Calculations[67] indicate that MIGS might be present at metal-semiconductor interfaces in densities sufficient to cause pinning of the Fermi level, as in the Bardeen theory. Because of the origin of MIGS, the

pinning of the Fermi level is a reversible phenomenon; upon removal of the metal the MIGS would revert to the intrinsic surface states.

The deposition of metal on semiconductor surface might also generate interface states by causing structural damage to the surface thus increasing the density of defects such as steps (on cleaved surfaces), vacancies or anti-sites defects (cations on anions sites and vice-versa). This increase in defect density leads, in turn, to the pinning of the Fermi level. This model is called the unified defect model[68] and as opposed to the MIGS model the interface states created are permanent.

The mechanism of the Fermi level pinning is essentially the same for both the MIGS and the unified defect model as it is in the Bardeen theory, but with the layer of semiconductor between the surface of the metal and the centre of the depletion zone (caused by either electrons wave functions or defects) playing the role of the insulating layer of the Bardeen model.

3.1.4 Bias dependence of the barrier height

The Bardeen relationship for the barrier height presented in section 3.1.2 has been derived for the flat-band case, where there is no electric field in the semiconductor. However, such an electric field normally exists within a Schottky barrier, and the voltage drop across the interfacial layer is modified by it. The barrier height ϕ_B is then reduced from its flat-band value ϕ_{BF} by an amount proportional to the maximum electric field in the semiconductor E_{max} which itself depends on the applied bias:

$$\phi_B = \phi_{BF} - \alpha E_{\max}$$

[3-11]

with

$$\alpha = \frac{\delta\varepsilon_s}{\varepsilon_i + q\delta D_s}$$

[3-12]

where ε_i and ε_s are the permittivity of the insulating layer and semiconductor.

Even without an insulating layer at the interface, the barrier height is influenced by the electric field within the semiconductor. Electrons approaching the metal surface experience an attractive force as if a positive charge of magnitude q was located at the

mirror image of the electron with respect to the interface. This effect gives the electrons a negative potential energy, which has to be added to the potential energy due to the Schottky barrier thus leading to a lowering of the barrier by an amount,

$$\Delta\phi_{Bi} \propto \left[N_D \left(\phi_B - V - \xi - \frac{kT}{q} \right) \right]^{1/4}$$

[3-13]

3.1.5 Electronegativity and ionicity

The electronegativity of an atom in a molecule measures its ability to attract the bonding electrons to itself. Pauling[69] described the ionicity of the single bond of a diatomic molecule by the electronegativity difference of the atoms involved. If the difference is high (ionic material), the valence (bonding) electrons will be localised around the atom with the highest electronegativity, thus creating an imbalance in the allocation of the electronic charge. On the other hand, in single element semiconductors like Si or Ge or when the difference in electronegativity is low (covalent material), the valence electrons do not discriminate any particular atom.

Upon analysing a large body of data about metal contacts on III-V semiconductors, it has been found[70] that the barrier height is much more dependent on the metal for contacts to ionic semiconductors than to covalent ones. This is illustrated on Figure 3-5 and Figure 3-6. Figure 3-5 shows the variation of the barrier height ϕ_B of various metals on three n-type semiconductors with the electronegativity X_M of the metal. The slope ($S=d\phi_B/dX_M$) of a straight line fit to the data points varies from nearly zero for covalent Si to near one for ionic SiO_2.

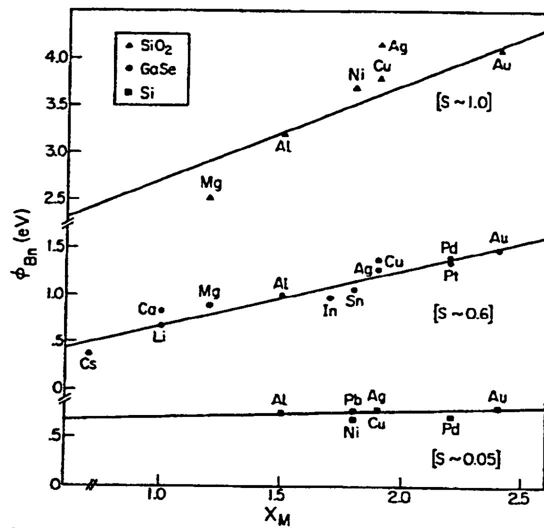

Figure 3-5: barrier heights of various metal on n-type semiconductors plotted versus the Pauling electronegativity X_M of the metal (from ref. 70).

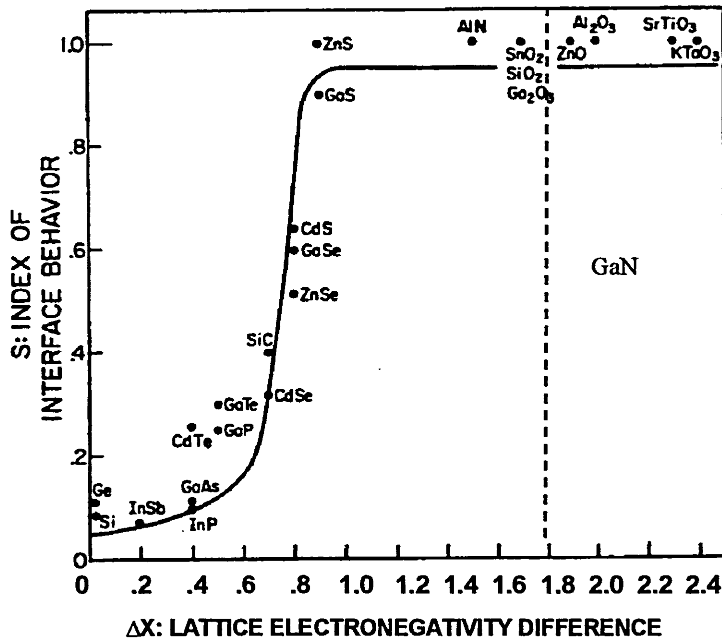

Figure 3-6: dependence of S on the electronegativity difference between the components of the compound (from ref. 70).

The slope, or index of surface behaviour S is plotted as a function of the lattice electronegativity difference (ionicity) of semiconductor compounds on Figure 3-6 and clearly reveals a transition between covalent and ionic semiconductors. This behaviour might be partly explained by the MIGS theory, as electrons wave functions penetrate a

much shorter distance into wide band gap, ionic semiconductors compared with low band gap, covalent materials[8]. This would mean less MIGS and therefore a less effective pinning of the Fermi level. GaN is a strongly ionic material (ΔX=1.8), therefore the barrier height of metal contacts is expected to depend on the electronegativity of the metal.

3.1.6 The MIGS-and-electronegativity model

This model is a combination of the physical MIGS and chemical electronegativity concepts put forward by Mönch[71]. The author assumed that the formation of MIGS is the dominant mechanism governing the barrier height of intimate, abrupt metal–semiconductor interfaces. As for the Bardeen model, a charge neutrality level can be defined for the MIGS: the net charge in the MIGS continuum has positive sign, vanishes and becomes negative when the Fermi level at the interface is below, coincides or is above the charge neutrality level. Since interfaces are neutral, the charge in the MIGS continuum is compensated by an equal amount of charge of opposite sign, on the metal side of the interface. The authors likened this imbalance of charge at the interface to that of an ionic bond of a diatomic molecule. We saw in the previous section that Pauling correlated the ionic character of single bonds in a diatomic molecule with the difference of the atomic electronegativities. A generalisation of this chemical concept then describes the charge transfer across metal-semiconductor interfaces by the difference of the metal and semiconductor electronegativities. According to this model the barrier height is given by (see ref. 71 for calculation details):

$$\phi_B = \phi_{cnl} + S(X_M - X_S)$$

[3-14]

where S is the slope parameter defined in the previous section, ϕ_{cnl} the energy position of the charge neutrality level within the band gap and X_M and X_S are the electronegativities of metal and semiconductor, respectively. Theoretical predictions from this model were found to be in excellent agreement with experimental data for a number of semiconductor materials including GaN, as shown on Figure 3-7.

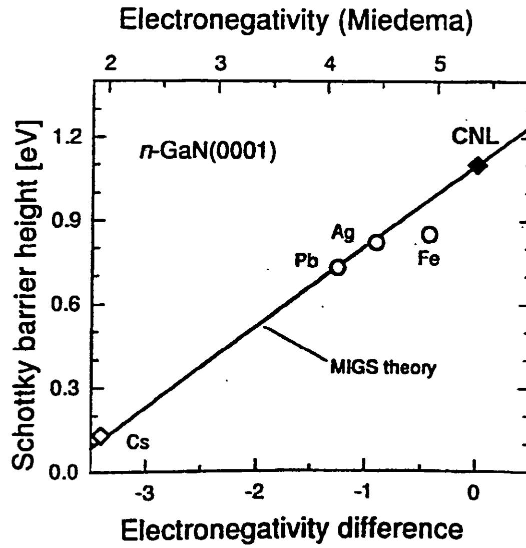

Figure 3-7: barrier heights of GaN Schottky contacts as a function of the difference of the metal and the GaN electronegativity. The Cs data point was determined by using ultraviolet photoemission spectroscopy and a Kelvin probe. The MIGS line is drawn with the charge neutrality level (CNL) at 1.1 eV below the conduction band and a slope parameter *S* of 0.29 eV/Miedema-unit. From ref. 71.

3.1.7 The Cowley-Sze model

This model[72] postulates a uniform density of surface states, D_S ($cm^{-2}eV^{-1}$), throughout the gap. These states are assumed to be independent of any chemical effect, other than charge transfer resulting from metal deposition. Neglecting any image charge effect, the barrier height ϕ_{BO} is expressed as a sum of the "bare surface barrier height" ϕ_O or band bending before metal deposition, and a Schottky-Mott term induced by the metal:

$$\phi_{BO} - \phi_o = S(\phi_M - \chi) - S\phi_o$$

[3-15]

where ϕ_M is the metal work function and χ the semiconductor electron affinity. S is a constant depending only on the density of surface state D_S:

$$D_S \approx 10^{13} \frac{(1-S)}{S}$$

[3-16]

Bermudez[63] suggested that this model could be used to interpret results from several groups, as shown on Figure 3-8. The difference in S can be related to a

difference in the density of surface states which is attributed to pre-metallisation surface treatment, substrate choice (sapphire versus SiC) and/or surface polarities.

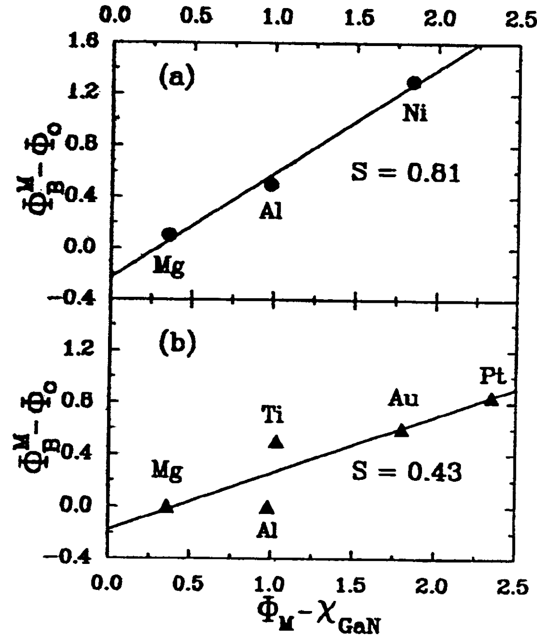

Figure 3-8: metal-nGaN barrier heights vs metal work function, plotted in accordance with equation [3-15], from photoemission data given in (a) Refs. 62 and 52 and in (b) Ref. 59.

3.1.8 The effective work function model

This model suggests that the Fermi level at the surface of a semiconductor or at a metal-semiconductor interface is not fixed by surface states but rather is related to the work functions of microclusters of the one or more interface phases resulting from either oxygen contamination or metal-semiconductor reactions which occur during metallisation. According to this assumption, the ideal Schottky-Mott relationship (equation [3.1]) becomes:

$$\phi_B = \phi_M - \phi_{eff}$$

[3-17]

where ϕ_{eff} is an appropriately weighted average of the work function of the different interface phases.

The authors argued that for most of the III-V compounds the effective work function is mainly due to the work function of the anion. They found that the barrier

heights of Au contacts on a variety of III-V and II-VI compounds correlated well with the anion work function.

3.2 Current transport mechanisms

There are essentially three ways by which electrons can cross from the semiconductor into the metal under applied bias[8]:

-a- emission over the barrier
-b- tunnelling through the barrier
-c- recombination

In an ideal Schottky diode the current flow across the barrier would be entirely due to the first mechanism. In a real diode, the contributions of the other two cause departure from the ideal case.

3.2.1 Emission over the barrier

This mechanism can itself be split into two different processes, diffusion current and thermionic emission current. Although the real current is a combination of these two, numerous experiments showed that the thermionic emission theory agrees the best with the experimental data and is now widely adopted[8]. The thermionic emission theory[73] assumes that the effect of drift and diffusion in the depletion region is negligible. The current is controlled by the transfer of electrons across the barrier. According to the kinetic theory of gases, only a limited number of electrons can cross the barrier in unit time. Assuming Boltzmann statistics, the number of electrons with velocity between v_x and v_x+dx, which pass unit cross-section in unit time, is[74]:

$$dn = n_e v_x \sqrt{\frac{m}{2kT}} \exp\left(\frac{-mv_x^2}{2kT}\right) dv_x$$

[3-18]

where n_e is the equilibrium electron concentration and m the standard electron mass. The minimum velocity v_{x0} required to cross the barrier from the semiconductor (forward direction) is given by

$$E_0 = \frac{1}{2}mv_{x0}^2 = q(V_D - V)$$

[3-19]

Where V_D is the built-in diffusion potential and V the applied bias (V>0). The current density in the forward direction is therefore:

$$j_+ = q\int_{v_{x0}}^{\infty} dn = n_e q\sqrt{\frac{kT}{2\pi m}}\exp\left(\frac{-q(V_D - V)}{kT}\right)$$

[3-20]

The electron concentration at the interface is given by:

$$n_e = 2\left(\frac{2\pi m^* kT}{h^2}\right)^{3/2}\exp\left(\frac{-q(\phi_B - V)}{kT}\right)$$

[3-21]

The total current density $j = j_+ + j_-$ must be zero when V=0, so

$$j = j_0\left[\exp\left(\frac{qV}{kT}\right) - 1\right]$$

[3-22]

with:

$$j_0 = A^* T^2 \exp\left(\frac{-q\phi_B}{kT}\right)$$

[3-23]

where $A^* = 4\pi q m^* k^2/h^3$ is the Richardson constant and m^* the electron effective mass.

3.2.2 Tunnelling through the barrier

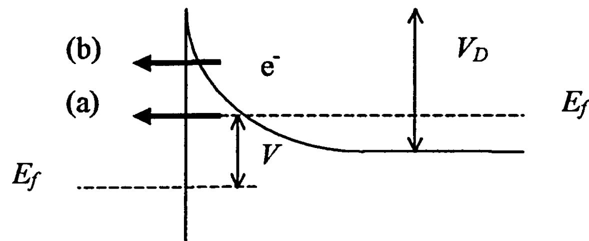

Figure 3-9: (a) field emission, and (b) thermionic field emission for a degenerate semiconductor.

Even when the temperature is too low for the electrons to be thermally excited over the barrier, there might be a current flowing across the interface due to electron tunnelling. According to quantum mechanics, an electron has a non-zero probability of crossing a barrier potential greater than its energy. The wave vector of the electron wave function becomes imaginary within the barrier and the wave function decays exponentially with the distance. Therefore, the thinner the barrier the greater the probability of tunnelling. Figure 3-9 shows the pure field emission case (a) and the so-called thermionic-field emission case (b) which occurs when the temperature is high enough to thermally excite a significant number of electrons to an energy where tunnelling is more probable. Applying the WKB approximation to a triangular barrier, the probability is given by[8]:

$$P = \exp\left\{\frac{-2(\Delta E)^{3/2}}{3E_{00}}\sqrt{V_D}\right\}$$

[3-24]

with

$$E_{00} = \frac{h}{2\pi}\sqrt{\frac{N_D}{m^* \varepsilon_s}}$$

[3-25]

where N_D is the donor concentration in the semiconductor and ε_s its permittivity. Field emission is likely to occur if $E_{00} >> kT/q$, thermionic-field emission if $E_{00} \approx kT/q$ and pure thermionic emission if $E_{00} << kT/q$[75]. We can see that the smaller the effective mass and the higher the doping, the more likely tunnelling is. This is why field emission only occurs in degenerate semiconductors as shown on Figure 3-9. The degenerate case is of great importance for Ohmic contacts, where the high resistivity of the barrier is overcome by tunnelling of electrons from the heavily doped semiconductor into the metal.

It has been shown that the current/voltage relationship is of the same form as for the pure thermionic emission theory[75]:

$$j = j_s \exp\left(\frac{V}{E_0}\right)\left\{1 - \exp\left(-\frac{qV}{kT}\right)\right\}$$

[3-26]

where $E_0 = E_{00}$ for field emission and $E_0 = E_{00}\coth(qE_{00}/kT)$ for thermionic field emission. For thermionic field emission, the pre-exponential term j_S is given by[75]:

$$j_S = A^* T^2 \exp\left(-\frac{q\xi}{kT}\right)\frac{q}{kT}\frac{\{\pi E_{00}(\phi_B - V - \xi)\}^{1/2}}{\cosh(qE_{00}/kT)}\exp\left(-\frac{\phi_B - \xi}{E_0}\right)$$

[3-27]

3.2.3 Recombination current

Electron-hole recombination can either take place in the depletion region through localised states or in the bulk of the semiconductor due to hole injection (for a n-type semiconductor). The latter effect arises when the Schottky barrier height is greater than half the band gap, which means that the semiconductor region immediately next to the interface has become p-type and contains a high density of holes.

Recombination in the depletion region takes place through localised states in the middle of the forbidden gap and the current density for low forward bias is given by[76]:

$$j = j_0 \exp\left(\frac{qV}{2kT}\right)\left\{1 - \exp\left(-\frac{qV}{kT}\right)\right\}$$

[3-28]

with

$$j_0 = qn_i \frac{W}{2\tau_r}$$

[3-29]

where n_i is the intrinsic electron concentration, W the depletion width defined by equation [3-5] and τ_r the lifetime within the depletion region.

3.2.4 Ideality factor

The current/voltage relationship derived from the thermionic emission theory in section 3.2.1 (equations [3-22] and [3-23]) assumes that the barrier height is independent of bias. However, as discussed in section 3.1.4, the barrier height is bias dependent because of the image-force lowering effect and the presence of an interfacial layer. In order to take this into account, the effective barrier height[8] ϕ_{eff} is introduced:

$$\phi_{eff} = \phi_{B0} - (\Delta\phi_{Bi})_0 + \beta V$$

[3-30]

where ϕ_{B0} and $(\Delta\phi_{Bi})_0$ are the barrier height and image-force lowering at zero-bias. The variation of the effective barrier height with bias is assumed linear, with $\beta = \frac{\partial\phi_{eff}}{\partial V}$=constant. After substituting in the ideal current/voltage relationship (equation [3-22]), we obtain:

$$j = j_0 \exp\left(\frac{qV}{nkT}\right)\left\{1 - \exp\left(-\frac{qV}{kT}\right)\right\}$$

[3-31]

with

$$j_0 = A^* T^2 \exp\left[-\frac{q}{kT}(\phi_{B0} - (\Delta\phi_{Bi})_0)\right]$$

[3-32]

and where $1/n=1-\beta$. n is called the ideality factor and is an important parameter of any real diodes. The more n is close to unity, the more ideal the diode is. As β is always positive (in the forward direction), n cannot be smaller than unity. Equation [3-31] is often re-written in the literature[8] in the form:

$$I = I_0\left\{\exp\left(\frac{q(V - IR)}{nkT}\right) - 1\right\}$$

[3-33]

with,

$$I_0 = AA^{**}T^2 \exp\left(\frac{-q\phi_B}{kT}\right)$$

[3-34]

where A is the contact area, A^{**} is the effective Richardson constant, and R is the series resistance. When the forward bias is low enough so that the effect of series resistance is negligible compared to the contact resistance and high enough so that the '1' in the bracket is negligible compared to the exponential term (typically for V such as $3kT/q<V<\phi_B$), then equation [3-33] is reduced to:

$$I = I_0 \exp\left(\frac{qV}{nkT}\right)$$

[3-35]

This expression for the current density is used to extract the zero-bias barrier height and ideality factor from experimental I-V curves. When plotted on a semi-log scale, equation [3-35] is a straight line, which slope yields n and y-intercept yields j_0 and therefore ϕ_{B0} through equation [3-23].

The departure from ideality is not only due to the bias dependence of the barrier height but also arises from tunnelling and recombination currents. As the current/voltage relationships of these two currents are similar in form to equation [3-31], it is possible to define an ideality factor associated with them: $n_{tunnelling}=qE_0/kT$ from equation [3-26] and $n_{recombination}=2$ from equation [3-28]. The ideality factor extracted from current/voltage measurements will then be a combination of the ideality factors associated with bias dependence, tunnelling and recombination. Even a perfect diode, free of these effects will have an ideality factor greater than unity because of the image force lowering (typically n=1.01-1.02).

3.3 Extraction of the Schottky parameters

The standard method for extracting the Schottky parameters (barrier height and ideality factor) from experimental I-V measurement data is to fit equation [3-35] to the linear region of the log(I) versus V curve. This region lies within a voltage interval which theoretical lower boundary is about $3kT/q$ (80 mV at room temperature) and which upper boundary is determined by the series resistance. The higher the series resistance, the lower this boundary lies. Additionally, shunt resistance effects can hide the low bias part of the linear region. In some cases, the linear region is completely hidden by high series resistance combined with shunt resistance effects and fitting equation [3-35] is impossible. In an effort to find a way around this problem, researchers have devised more advanced extraction methods, which are presented in this section.

3.3.1 Norde plot

This method assumes an ideality factor of unity and uses the following function:

$$F(V) = \frac{V}{2} - \frac{kT}{q}\ln\left(\frac{I}{A^{**}T^2}\right)$$

[3-36]

After replacing I by equation [3-33] with n=1, F can be rewritten as:

$$F(V) = \phi_B + IR - \frac{V}{2}$$

[3-37]

The series resistance is negligible at small forward bias so that a plot of $F(V)$ will approach a straight line of slope –1/2. Inversely, the series resistance is the only hindrance to current flow at high forward bias so IR can be replaced by V in equation [3-37], which makes $F(V)$ approaching a straight line of slope +1/2 for large forward bias. In between these two extremes, $F(V)$ reaches a minimum at a voltage V_0 and current I_0, which gives respectively the barrier height and the series resistance:

$$\phi_B = F(V_0) + \frac{V_0}{2} - \frac{kT}{q}$$

[3-38]

$$R = \frac{kT}{qI_0}$$

[3-39]

3.3.2 Small signal conductance

This method, put forward by Werner[77], yield the ideality factor and the series resistances *via* the conductance G. The series resistance thus obtained can then be used to correct the voltage axis of the raw I/V plot in order to determine the saturation current and therefore the barrier height.

At forward bias greater than $3kT/q$, equation [3-33] can be rewritten as:

$$I = I_0 \exp\left(\frac{q(V - IR)}{nkT}\right)$$

[3-40]

Equation [3-40] yields for the small signal conductance $G = \frac{\mathrm{d}I}{\mathrm{d}V}$:

$$\frac{I}{G} = \frac{kT}{q}n + RI$$

[3-41]

Plotting I/G versus I therefore results in a straight line which slope and y-axis intercept yield the series resistance and ideality factor, respectively.

Werner pointed out that a step size of 1 mV would be needed to numerically determine the conductance G from the original I/V curve in order to get the real slope rather than just a secant line. Instead of measuring the I/V curves with such small voltage steps, it is possible to determine G from the less steep log(I)/V curve with the help of the identity:

$$G = I \frac{\mathrm{d}(\ln I)}{\mathrm{d}V}$$

[3-42]

In this case even voltage steps of 10 mV are small enough to yield a good approximation of the true slope of the I/V curve.

3.3.3 Flat-band barrier height

This method, proposed by Wagner *et al.*[78], does not directly solve the problem caused by shunt or series resistance effects but rather provides a more fundamental value of the barrier height than the zero-bias barrier height. We have seen in section 3.1.1 that under flat-band condition the internal electric field across the interface is zero and the depletion zone disappears. The flat-band barrier height is therefore unaffected by electric field dependant effects such as tunnelling, recombination, image force lowering or interfacial oxide layer.

The flat-band barrier height ϕ_{BF} can be derived from the conventionally extracted zero-bias barrier height ϕ_{B0} and ideality factor n:

$$\phi_{BF} = n\phi_{B0} - (n-1)\frac{kT}{q}(E_c - E_f)$$

[3-43]

Chapter 4: Experimental techniques

In this chapter, the theory and experimental set-up of the techniques used to characterise the GaN surfaces and the formation of Au-GaN interfaces are presented.

XPS has been the main experimental technique utilised during the course of this research; hence the fundamental principles of photoemission and the description of the experimental apparatus form the main part of this chapter. The non-destructive and surface sensitive nature of the photoemission process lends itself to the study of the chemical, electrical and structural nature of metal-semiconductor interfaces.

TEM and transport measurements have also been employed as complementary techniques, hence a brief description of the fundamental principles of TEM and the I-V experimental set-up is presented.

4.1 The Photoemission process

Photoemission theory has been developed from Einstein's original work on the photoelectric effect[79]. Photoemission is the emission of electron from a solid as a result of the absorption of photons. The electrons are emitted from the surface if the incident photons have an energy ($h\nu$) that is greater than the binding energy (E_b) of the electron plus the work function (ϕ) of the solid. The subsequent kinetic energy of the emitted photoelectron is given by the following equation,

$$E_k = h\nu - E_I - \phi \tag{4-1}$$

where E_I is the initial state energy of an electron in the solid. According to Koopmans theorem[80], the initial state energy (E_I), can be regarded to a first approximation as the binding energy of the electron in the solid. This however fails to account for the hole left when the electron is emitted from the solid. The remaining electrons will relax to a lower energy state in order to screen the photo-hole from the nucleus, resulting in an excess of energy, which is carried away by the ejected photoelectron. The consequence of this action is that the kinetic energy of the emitted photoelectron is increased resulting in an apparent reduced energy of the initial state.

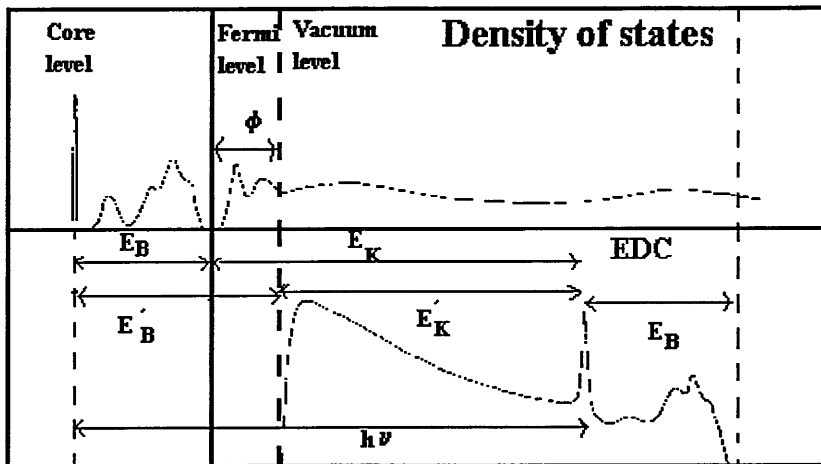

Figure 4-1: A schematic representation of how the density of states of a semiconductor relates to the energy distribution curve (EDC) obtained by the X-ray Photoemission process.

Once the photoelectrons have escaped from the surface of the solid, the spectrometer measures the number of electrons emitted at values of kinetic energy from zero up to a maximum value, determined by the energy of the incident photons. The result is presented as an energy distribution curve (EDC) as shown on Figure 4-1.

In XPS, the photons are provided by an x-ray source; however, in recent years extensive use has been made of synchrotron radiation to provide photons with a tuneable range of energies. This technique can provide a photon beam of much lower energy (in the soft x-ray range) for increased surface sensitivity, and hence is known as "soft XPS" or SXPS. The EDC obtained (see Figure 4-1) reflects the density of occupied states in the solid. However, the EDC is not a direct representation of the density of states as there also exists a large featureless background to low kinetic energy which is characteristic of emitted electrons that have undergone inelastic scattering and lost energy during propagation through the solid to the surface[81]. Electrons that have been emitted from the comparatively narrow core levels and the broad valence band without loss of energy produce sharp discrete peaks in the EDC.

The sharp core level photoemission peaks can be used to identify specific atoms near the surface of the solid, as each element has its own set of discrete core level binding energies[8,82]. It is for this reason that XPS is occasionally known as ESCA (electron spectroscopy for chemical analysis) as the chemical composition of the material near the surface can be identified.

More importantly studying the changes in peak positions and hence binding energies of the core levels can give information on chemical, electrical and structural changes at the surface of the solid[83]. This makes photoemission a powerful tool in the non-destructive analysis of surfaces and interfaces. It is surface and chemically sensitive and provides information on the atomic bonding of species present in a material.

4.2 The three step model

There are many models that have been proposed to describe the photoemission process, the most accurate ones being those that describe it as a single quantum mechanical event, from the absorption of a photon through to the emission and detection of the photoelectron[81,84,85]. These theories however are extremely intricate, and for the purpose of explaining the photoemission process and the phenomena

observed in the photoemission data presented here, a far simpler model, The Three Step Model, is discussed[86,87]. This model ignores many body effects such as electron-electron interactions and inelastic scattering and focuses on the elastically scattered electrons.

The Three Step Model describes the photoemission process in three stages, which are all dependent on the initial electron energy (E) and the energy of the incident photons ($h\nu$). These stages are:

(i)	Photoexcitation of the electron	$P(E,h\nu)$
(ii)	Propagation through the solid	$T(E,h\nu)$
(iii)	Escape from the solid surface into vacuum	$D(E,h\nu)$

The intensity of the resulting photocurrent $I(E,h\nu)$ is given by the relation,

$$I(E,h\nu) = P(E,h\nu)T(E,h\nu)D(E,h\nu)$$

[4-2]

(i) Step one: Photoexcitation

If the photoemission process is considered for each individual particle one can use the independent particle approximation whereby the unperturbed system is described by the Hamiltonian energy operator,

$$\hat{\mathbf{H}}_o = \frac{\hat{\mathbf{p}}^2}{2m} + \mathbf{V}(\mathbf{r})$$

[4-3]

where $\hat{\mathbf{p}}$ is the momentum operator, m is the mass of the electron and $\mathbf{V}(\mathbf{r})$ is the self consistent screening potential energy operator, which accounts for the effects of the other electrons on the independent electron as well as surface effects.

If this system is subsequently perturbed by the absorption of a photon, the introduction of an electromagnetic wave of vector potential $\mathbf{A}$ will change the momentum operator such that it becomes[88],

$$\hat{\mathbf{p}} + \frac{e}{c}\mathbf{A}$$

[4-4]

And the new perturbed Hamiltonian can be written as,

$$\hat{\mathbf{H}} = \frac{1}{2m}\left[\hat{\mathbf{p}} + \frac{e}{c}\mathbf{A}\right]^2 + \mathbf{V}(\mathbf{r})$$

[4-5]

If this equation is expanded we see that,

$$\hat{\mathbf{H}} = \frac{\mathbf{p}^2}{2m} + \mathbf{V}(\mathbf{r}) + \frac{e}{2mc}(\hat{\mathbf{p}}.\mathbf{A} + \mathbf{A}.\hat{\mathbf{p}}) + \frac{e^2\mathbf{A}^2}{2mc^2}$$

[4-6]

And hence substituting equation [4-3] gives,

$$\hat{\mathbf{H}} = \hat{\mathbf{H}}_0 + \hat{\mathbf{W}}$$

[4-7]

where W is the electron-radiation interaction Hamiltonian. By applying the dipole approximation[89], only linear terms in **A** apply and hence the electron-radiation interaction Hamiltonian can be written as,

$$\hat{\mathbf{W}} = \frac{e}{2mc}(\hat{\mathbf{p}}.\mathbf{A} + \mathbf{A}.\hat{\mathbf{p}})$$

[4-8]

The transition rate between an initial state $|\psi_i\rangle$ and the final state $|\psi_f\rangle$ in relation to an electron-photon interaction can be given by the Fermi "Golden Rule" expression[89] such that,

$$\mathrm{P_{fi}} = \frac{2\pi}{\hbar}\left|\langle\psi_\mathrm{f}|\ \hat{\mathbf{W}}\ |\psi_\mathrm{i}\rangle\right|^2 \delta\ (E_\mathrm{f} - E_\mathrm{i} - h\upsilon)$$

[4-9]

where ψ_i and ψ_f are the initial state and final state wavefunctions, having energies E_i and E_f, respectively. The δ-term ensures that there is energy conservation between $h\nu$ and the transition energy $(E_f - E_i)$. The resulting photocurrent is given by the equation,

$$\mathrm{P}(E,h\upsilon) = \frac{2\pi}{\hbar}\sum_i\left|\langle\psi_\mathrm{f}|\ \hat{\mathbf{W}}\ |\psi_\mathrm{i}\rangle\right|^2 \delta\ (E_\mathrm{f} - E_\mathrm{i} - h\upsilon)$$

[4-10]

The summing over all initial states is an approximation, with a more accurate summation being one that incorporates all final states as well. However, for a large density of final states, the modulation of the photocurrent will be negligible. Only for

low final state energies ($\leq$20 eV) does this final state density become significant to the observed photocurrent and hence for XPS and SXPS experiments this effect will be trivial resulting in the photocurrent being characteristic of the initial density of states.

(ii) Step two: Propagation of the electron through the solid

Once the electrons have been excited due to the absorption of a photon, they must make their way to the surface of the solid where they will be emitted and detected. En route to the surface, it is highly likely that the electrons will be scattered and hence the resulting photocurrent will be modified. The propagation probability $T(E,h\nu)$ can be expressed in terms of the inelastic mean free path of the electron $\lambda(E)$, which is defined as the average distance an electron with energy E can travel through a solid before being inelastically scattered. If one considers the number of electrons (N_o) that are photoexcited at a distance x from the surface, then the number of electrons (N) that actually reach the surface without losing any energy is given by the equation,

$$N = N_o \exp\left(\frac{-x}{\lambda(E)}\right)$$

[4-11]

Hence the propagation probability can be written as[81],

$$T(E,h\upsilon) = \exp\left(\frac{-x}{\lambda(E)}\right)$$

[4-12]

If the penetration depth (x) of the photon is assumed to be much larger than λ, then the above equation is thought to be a constant.

(iii) Step three: Electron escape from the solid

Once the electrons have propagated to the surface of the solid, they must possess enough energy to escape into vacuum. The electrons must have a component of momentum normal to the surface and enough energy to overcome the work function of the solid. Therefore the probability of escape from the solid $D(E)$, may be described simply as zero when the electrons do not possess enough energy to escape and one

when they do such that,

$$D(E) = 0 \qquad \text{when } E_{norm} - E_{vac} < \phi$$

[4-13]

$$D(E) = 1 \qquad \text{when } E_{norm} - E_{vac} \geq \phi$$

[4-14]

where E_{norm} is the component of final state energy normal to the surface and E_{vac} is the vacuum level of the solid.

The final expression for the photocurrent can be written as a product of the three steps described previously, whereby,

$$I(E,h\upsilon) = \frac{2\pi}{\hbar}\sum_i \left|\langle \psi_f \right| \hat{\mathbf{W}} \left| \psi_i \rangle\right|^2 \delta\left(E_f - E_i - h\upsilon\right)\exp\left(\frac{-x}{\lambda(E)}\right)D(E)$$

[4-15]

The Three Step Model is relatively basic as it neglects many-body effects. However, it is useful for interpreting the EDC's obtained by the photoemission technique used in this work.

4.3 Photo-ionisation cross section

The probability of a transition per unit time for excitation of a single photoelectron from the core level of interest due to an incident photon flux of 1 $cm^{-2}s^{-1}$ is given as the photo-ionisation cross section (σ) and is related to the matrix element $|\langle \psi_f | \mathbf{W} | \psi_i \rangle|$ discussed in section 4.2. The intensity of the transition between the initial state and the final state is determined by the cross section and since the final state energy depends on the energy of the incident photon beam, σ will also vary with the photon energy[82]. The resulting intensity of a given core level emission peak will vary with photon energy and the majority of core level emission peaks encounter a minimum in σ at certain photon energies known as a Cooper minimum[90]. Experimentally observed values of σ for individual core levels have been collected and tabulated as a function of photon energy by Yeh and Lindau[82]. These tables are of great use when performing experiments using a synchrotron radiation source as it is possible to maximise the emission intensity of the core level being studied by tuning the photon

energy to exhibit the maximum possible cross section. However, this can result in a loss of surface sensitivity and hence a compromise between surface sensitivity and cross section usually needs to be found.

4.4 Surface sensitivity

4.4.1 Electron scattering and inelastic mean free path (IMFP)

As the excited photoelectrons propagate through the solid towards the surface, they can be scattered either elastically or inelastically by scattering centres within the solid. If an electron is elastically scattered it suffers no loss in energy but can experience a change in direction and upon detection will provide information on the energy state of the core level it was emitted from. Inelastically scattered electrons undergo a loss of energy and may also experience a change in direction. Typically electrons may lose up to several eV due to inelastic scattering, although scattering by phonons results in a loss of energy of only a few meV and is negligible compared to the resolution of the spectrometer. Electrons that do encounter inelastic scattering may do so on a random number of occasions and hence may lose a significant amount of energy en route to the surface. Should the electrons still have enough energy to escape from the solid surface when they arrive, they will have a kinetic energy significantly different to that of the elastically scattered electrons and will contribute in a random way to the featureless background to lower kinetic energy on the EDC. Inelastic scattering occurs due to the creation of electron-hole pairs or by the generation of plasmons, which involve a collective oscillation of conduction, valence or shallow core level electrons. The plasmon loss features are not random and result in peaks at roughly 10 to 30 eV on the lower kinetic energy side of the unscattered elastic emission peak.

The mean free path (λ) of an electron is defined as the average distance that an electron of energy E, can travel through the solid before being inelastically scattered[91]. The value of λ for electrons in a solid is greatly dependent on the kinetic energy of the electron and the relationship between the two is shown in Figure 4-2[83]. The shape of the curve is determined by the formation of electron-hole pairs and plasmons typically in the energy range 20-100 eV. At low energies (below the plasmon energy) electron scattering is dictated by single-particle electron excitations involving valence electrons and the ionisation of core levels. The associated cross sections of these processes are

small compared to other processes and hence the mean free path for such collisions is about two orders of magnitude greater than for plasmon scattering[92].

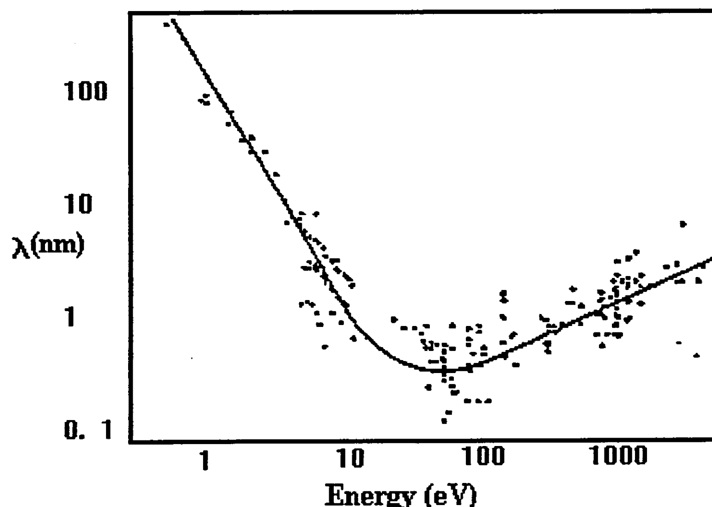

Figure 4-2: The dependence of attenuation length λ on the emitted electron energy for elements, from Ref. 83.

At energies above the plasmon energy, the plasmon scattering cross section rises sharply and hence the probability of inelastic scattering increases. This reduces the mean free path to about a few Å. When λ becomes this small, electrons emerging from the surface without loss of energy must have originated from within the first few monolayers of the solid. It is this aspect of photoemission that makes it a surface sensitive technique. As the energy of the electrons increases above ~100 eV, the MFP increases. This is due to the fact that the electrons have a greater velocity and hence are not influenced as much by scattering centres. Typically a mean free path of $\lambda \approx 5$ Å can be achieved for electrons with a kinetic energy of around 40 eV. The surface sensitivity can be altered by changing the photon energy and hence the kinetic energy (see equation [4-1]) using a tuneable synchrotron radiation source.

4.4.2 Effective escape depth: Changing the angle of detection

It was discussed in section 4.3 that the photo-ionisation cross section varies with photon energy. This fact can cause problems when comparing emission intensities of bulk and surface sensitive spectra as the probability of photoelectron emission will

change with changing photon energy. However, altering the angle of detection of the emitted photoelectrons may also increase surface sensitivity[83]. If we consider electrons escaping at an angle θ from the normal to the surface as shown in Figure 4-3, those electrons travelling a distance λ through the solid will have come from a depth normal to the surface given by,

$$d = \lambda \cos\theta$$

[4-16]

In normal emission the detector is placed 90° to the surface (i.e. 0° from normal) and hence electrons detected will have travelled from within a distance $d = \lambda$ from the surface. If the angle of detection is changed to 60° from normal, the effective distance the electrons have travelled is given as $d = \lambda/2$, hence halving the effective escape depth and increasing surface sensitivity.

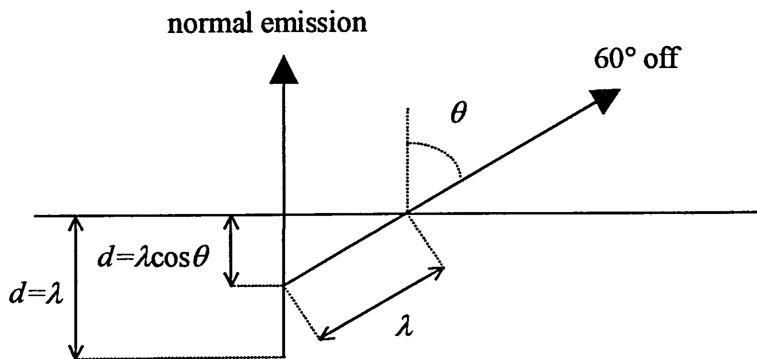

Figure 4-3: variation of the probing depth *d* with the analyser angle *θ*. here *θ*=60°. *λ* is the electron mean free path.

4.4.3 Photoelectron diffraction

Changing the angle of electron detection (i.e. rotating the sample in the surface plane) can produce variations in the observed core level intensity. This is known as photoelectron diffraction, and is due to interference (destructive and constructive) between the various coherent components of the same photoelectron wavefunctions.

4.5 Spectral interpretation

The simple picture presented in Figure 4-1 in which the EDC recorded by the electron analyser is a direct reflection of the density of electron states at the surface of a solid is experimentally never observed. There are several features present in a real XPS scan which did not arise from core level electrons but are due to Auger transitions, satellites X-ray lines and kinetic energy loss processes. It is important to distinguish the true core level peaks from these parasitic features.

4.5.1 Auger lines

The emission of an electron by the Auger process is described on Figure 4-4.

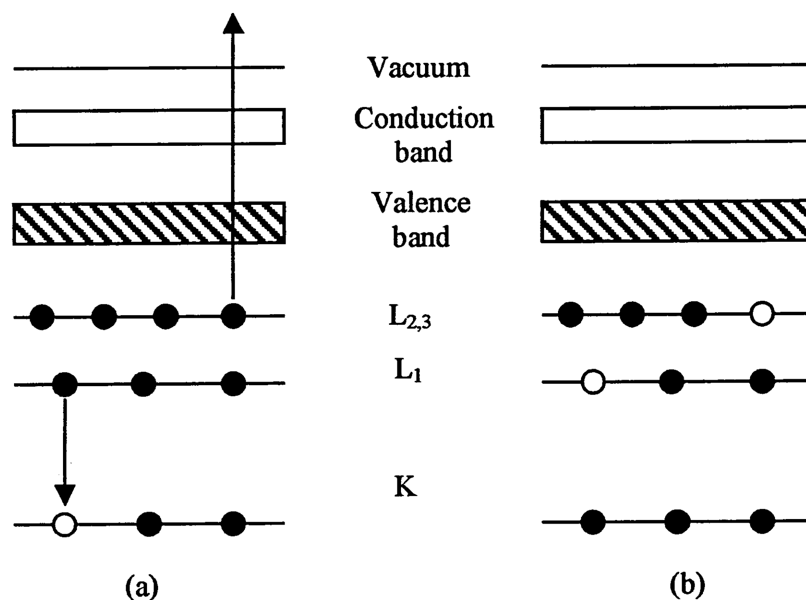

Figure 4-4: schematic diagram of the process of a KLL Auger transition in a semiconductor following emission of a photoelectron. (a) the hole left in the K shell by the photoelectron is filled by an electron from the L_1 shell and the energy from this transition is used to eject an electron from the $L_{2,3}$ shell. (b) the doubly ionised final state.

Following creation of a hole in the level K, the atom relaxes by filling the hole via a transition from an outer level, in this example shown as L_1. As a result of that transition the energy difference $(E_K - E_{L_1})$ becomes available as excess kinetic energy, and this excess energy can be used by the atom in either of two ways. It can appear as a

characteristic X-ray photon at that energy or it can be given to another electron either in the same level or in a more shallow level, ejecting this second electron (Auger electron) from the semiconductor[83]. The energy of the ejected Auger electron in the example of Figure 4-4 is .

$$E_{KL_1L_{2,3}} = E_K - E_{L_1} - E_{L_{2,3}}$$

[4-17]

Following emission of a Auger electron, the doubly ionised atom will relax and the resulting electron transitions can produce more, less energetic, Auger electrons. These electrons have discrete energies, given by equations similar to equation [4-17]. During an XPS scan, the Auger electrons are collected together with the photoelectrons and give rise to Auger lines. As shown by equation [4-17], above the excitation threshold the energy of Auger electrons is independent of the X-ray energy so that it is possible to discern Auger peaks from core level peaks by changing the photon energy.

4.5.2 X-ray satellites and ghosts

Satellites peak arise from the fact that standard X-ray sources are not monochromatic. Besides the principal $K\alpha_{1,2}$ line, ($2p_{3/2,1/2}$ to $1s$ transition) Mg and Al targets also produce a series of lower intensity lines which results in satellite peaks on the low binding energy side of the main core level peak. The line positions and intensities are given in Table 4-1.

Ghost peaks are due to excitation arising from impurity elements in the X-ray source. The most common ghost is Al $K\alpha_{1,2}$ from a Mg $K\alpha$ source. This arises from secondary electrons produced inside the source hitting the thin Al window used to prevent these same electrons from hitting the sample. This radiation will therefore produce weak ghost peaks 233.0 eV to higher kinetic energy of those excited by the dominant Mg $K\alpha_{1,2}$. Old or damaged targets can give rise to ghost peaks excited by Cu $L\alpha$ radiation, the main line from the exposed Cu base of the target.

Both satellite and ghost features can be avoided by using monochromated X-rays produced by dispersion of X-ray energies by diffraction in a crystal such as quartz.

	Separation from $K\alpha_{1,2}$ (eV) and relative intensity ($K\alpha_{1,2}$=100%)			
	Mg		**Al**	
X-ray line	**eV**	**%**	**eV**	**%**
$K\alpha'$	**4.5**	**1.0**	**5.6**	**1.0**
$K\alpha_3$	**8.4**	**9.2**	**9.6**	**7.8**
$K\alpha_4$	**10.0**	**5.1**	**11.5**	**3.3**
$K\alpha_5$	**17.3**	**0.8**	**19.8**	**0.4**
$K\alpha_6$	**20.5**	**0.5**	**23.4**	**0.3**
K_β	**48.0**	**2.0**	**70.0**	**2.0**

Table 4-1: high energy satellite lines from Mg and Al targets (from ref. 93)

4.5.3 Loss features

Even with monochromated X-rays, secondary peaks can be observed on the high binding energy side of the main peak. These features arise from kinetic energy loss processes such as plasmon loss and shake-up and shake-off effects.

Plasmon losses have been presented in section 4.4.1. These collective oscillations have fundamental characteristic frequencies and therefore need characteristic energies for excitation. Photoelectrons from a particular core level that have given up an amount of kinetic energy equal to one of these characteristic energies are said to have suffered a plasmon loss. This effect gives rise to plasmon peaks on the high binding energy side of the main peak, the energy separation between the two peaks being the plasmon characteristic energy, typically[92] 10 to 30 eV.

Shake up satellites arise when valence electrons are excited to higher unfilled levels following photoionisation. To the valence electrons, the loss of a core electron appears to increase the nuclear charge and causes substantial reorganisation, during which one valence electron might be excited to a higher level. The energy required for this transition is not available to the primary photoelectron and thus the two-electron process leads to discrete structure on the high binding energy side of the photoelectron peak. In a similar process, called ‘shake off’, valence electrons can be completely ionised instead of merely excited to a higher energy level. Shake off satellites rarely result in discrete peaks because the transition from discrete level to the continuum of unbound states above the vacuum level is not quantified.

4.6 Core level analysis

The binding energy of a particular core level peak is dependent on the chemical and electrical environment encountered by the emitting atom. If a change in environment of the emitting atom occurs, the binding energy of the core level emission peak will also change, with the difference in energy being described as a shift.

For example, the controlled deposition of a metallic species onto a semiconductor surface may induce shifts in the binding energy positions of the semiconductor core level peaks. These shifts can be due to structural, chemical or electronic changes in the surface region, with the total binding energy shift being a convolution of the various shifts. It is important that these shifts are distinguished from one another and hence the analysis of core level spectra is necessary in order to utilise photoemission as a technique to study solid surfaces and interfaces. The phenomena that give rise to such binding energy shifts are discussed in the following four subsections.

4.6.1 Structural or surface related shifts

The properties of a surface differ from those in the bulk of a material due to the abrupt termination of the bulk periodicity. The atoms at the surface therefore relax or reconstruct in order to minimise the surface energy and hence the binding energies of electrons emitted from atoms on or near the surface may be different to those emitted from bulk atoms. It is likely, therefore, that the observed emission from a given core level will be made up of a number of surface components and a bulk component. The relative intensities of these components will depend on the inelastic mean free path.

4.6.2 Chemical shifts

When a metal is deposited onto a III-V semiconductor it is possible that a chemical reaction will occur between the metal and species from the semiconductor[94]. Atoms that are involved in the reaction process will have their chemical environment modified and the redistribution of valence charge that occurs during bonding is identified in the EDC by a shift in the binding energy of the core levels. The transfer of charge may also be affected by the electronegativities of the different elements[95] consequently altering the electronic properties of the reacted species.

4.6.3 Band bending

When the position of the Fermi level shifts in a semiconductor due to the presence of surface states or the deposition of metals onto the surface, the resulting shift is known as band bending. This is an electronic effect and occurs due to the transfer of charge at the surface or interface as described in Chapter 3. This band bending induces a change in the Fermi level position at the surface compared to its position relative to the valence and conduction band edges in the bulk. The band bending occurs within the depletion region, which is usually much larger than the sampling depth of the photoemission technique. Hence all core level electrons that are detected will have been subjected to band bending with a subsequent shift in the core level peaks in the EDC. It is therefore possible to observe the development of the Schottky barrier during the initial stages of metal-semiconductor interface formation.

In order to determine accurately the extent of the core level shifts, an energy reference point must be used. In most photoemission studies it is common practice to measure the Fermi level of the system (in electrical contact with the sample) in order to obtain an exact position for the Fermi level[8]. This is easily achieved by scanning the Fermi edge of a metal, usually gold. The high density of states at the Fermi level in a metal ensures that emission from this region will be distinct and hence the Fermi level is easy to measure. Unfortunately this is not the case for a semiconductor, where the Fermi level often lies within the forbidden energy gap[8]. In this case it is more productive to determine the valence band maximum (VBM) and this is found at the cut off point of the valence band signal and the background signal. By subtracting the valence band maximum from the Fermi level position (both measured at the same photon energy) it is possible to determine the clean surface pinning position of the Fermi level within the band gap. The barrier height formed at metal-semiconductor interfaces (for low metal coverages) can therefore be estimated by adding the additional band bending due to metal deposition to the Fermi level pinning position. The meaningful determination of the energy position of the valence band and Fermi edges is however only possible when using monochromated X-rays, only relative energy shifts can be observed with a non-monochromated X-ray source.

4.6.4 Lineshape broadening effects

In some cases it may be hard to identify small core level shifts due to the

existence of peak broadening effects. The peak broadening is usually described as the full width at half maximum height (FWHM) of the photoelectron peak ΔE and is a convolution of several contributions such that[83],

$$\Delta E = (\Delta E_n^2 + \Delta E_p^2 + \Delta E_a^2)^{1/2}$$

[4-18]

where ΔE_n is the natural or inherent linewidth of the core level, ΔE_p is the linewidth of the photon source and ΔE_a is the analyser resolution.

The natural linewidth of the core level (i.e. the range in KE of the emitted photoelectrons) is due to the uncertainty in the lifetime of the ion state remaining after photoemission[83]. The broadening due to a synchrotron radiation source is affected by the beamline optics, and is usually in the range of 0.1-0.6 eV. For a conventional laboratory unmonochromated X-ray source, this broadening is 0.85 eV for the Al anode and 0.7 eV for the Mg anode[83]. The broadening due to the analyser is dependent on the analyser pass energy and this is discussed in section 4.7.1.

4.6.5 Core level intensities and overlayer growth

Up until now this chapter has dealt with the analysis of the core levels to detect surface induced, chemical and band bending shifts. These are all attributed to changes in the binding energy of the core level peaks. In addition to these shifts the intensity of core level peaks can provide information on the growth mode of a deposited metal overlayer. As the metal is deposited onto the semiconductor surface, the photoemission signal from the core levels within the semiconductor will be attenuated due to inelastic scattering in the growing overlayer.

If the metal grows in a layer by layer mode of growth, the substrate core level intensity will attenuate as governed by the equation[96],

$$I = I_o \exp\left(\frac{-d}{\lambda}\right)$$

[4-19]

where I_o is the clean surface core level emission intensity, d is the thickness of the metal overlayer and λ is the mean free path of electrons in the overlayer. Deviation from this exponential decay indicates either a non-uniform or clustering growth mode or inter-diffusion of substrate and overlayer species. Hence it is possible to identify layer by

layer growth by plotting the intensity of the attenuated signal as a function of metal overlayer thickness.

The three types of growth mode possible for a layer on a substrate are layer by layer (Franck van der Merwe mode), islanding (Volmer-Weber mode) and layer by layer followed by islanding (Stranski-Krastanov mode) and are illustrated in Figure 4-5.

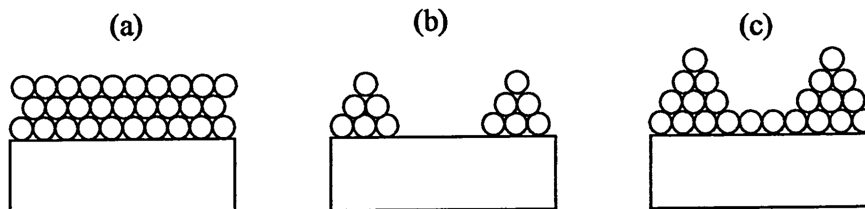

Figure 4-5: (a) Frank Der Merwe, (b) Volmer-Weber, (c) Stranski-Krastanov growth modes.

4.6.6 Spin orbit splitting

Many core level peaks split into doublets due to the coupling of the orbital and spin angular momenta of the electrons. Only core levels with an angular quantum momentum number $\ell>0$ will exhibit doublets and hence core levels such as *1s, 2s* and *3s* will be singlets. The outcome of coupling is the new total angular momentum given by,

$$j = \ell + s$$

[4-20]

where ℓ is the orbital angular momentum and s is the spin quantum number (±½)[97].

It is evident therefore that electrons with a total angular momentum of $j = \ell + ½$ will have a different energy to those with $j = \ell - ½$. Electrons with $j = \ell + ½$ are shifted to higher binding energy than those with $j = \ell - ½$. The resulting difference in energy is known as the spin orbit splitting. The relative intensities of the photoemission peaks in a doublet are given by the ratio of their respective degeneracies ($2j + 1$) as shown below,

$$R = \frac{2(\ell - s)+1}{2(\ell + s)+1}$$

[4-21]

Hence for the d core levels where $\ell = 2$, the ratio of the 3/2 spin orbit component to the 5/2 spin orbit component is 2:3.

4.6.7 Asymmetric metal core levels

The discussion so far in this chapter has concentrated on the analysis of emission from core levels in general. However the core level emission spectra will be different for a metal compared to a semiconductor. The high density of states at a metal Fermi level compared to a semiconductor results in increased electron scattering and a subsequent energy loss for those electrons emitted from the material. This has the effect of producing increased emission intensity at lower kinetic energies, which is observed as a tail to low kinetic energy side of the core level peak in the EDC.

4.6.8 Deconvolution of core level spectra

It has been discussed in this chapter that photoemission spectra can provide information on band bending and chemical reactions that occur during the formation of an interface. In order to interpret the reactions and shifts that take place, it is necessary to separate the raw photoemission data into its bulk, surface and reacted components. This can be done using a curve fitting routine on a computer. A mathematical technique developed by A.A. Cafolla, incorporating the conjugate gradient[98] and Levenberg-Marquardt[99] curve fitting methods was used to generate the basic shape of a single core level, and then the curve fitting routine performed a least squares minimisation to produce the best fit. A mix of Lorentzian and Gaussian functions, or Voigt function[100], was used to fit core level spectra. The Lorentzian function models the natural linewidth of the core hole lifetime and is given by the equation,

$$L(E) = \frac{1}{1 + 4\left(\frac{E - E_L}{\Gamma_L}\right)^2}$$

[4-22]

Where E_L is the energy centroid of the peak and Γ_L is the full width at half maximum (FWHM) of the peak.

The Gaussian function represents instrumental and other factors such as phonon broadening, and is given by the equation,

$$G(E) = \exp\left[-4\ln 2\left(\frac{E - E_G}{\Gamma_G}\right)^2\right]$$

[4-23]

Where E_G is the centroid of the peak and Γ_G is the full width at half maximum (FWHM) of the peak.

The Voigt function can be modified by changing various parameters such as the Lorentzian or Gaussian broadening, the spin orbit splitting of the core level, the intensity of individual components or the kinetic energy peak position of the components. Prior to any fit a suitable background must be removed. Inaccurate removal of the background can lead to discrepancies in peak intensities and positions and hence distort quantitative data analysis. The removal of the background must take into account the contribution made by secondary processes such as satellites and asymmetries. In general, there are two types of background subtraction. The first is a simple linear background, which is removed by taking a straight line between the first and last set of points in the spectrum. This method is useful when the signal to noise ratio is large. The second method is the removal of a non-linear background either in the form of a polynomial or derived from the method described by Shirley[101].

Once a suitable background has been removed, the fitting can begin. The clean surface spectrum is fitted with an estimate first, keeping the number of components as low as possible. Each individual component has a number of parameters that contribute to its lineshape. These are L(E), G(E), the spin orbit splitting (SOSP) of the core level being probed and their relative intensities, the peak position and the peak intensity. L(E), SOSP and relative spin orbit peak intensities were kept fixed during the fitting routine, as they are inherent of the core levels being probed. The fit of the overall spectrum is then iteratively refined using the least squares method, and the quality of the fit is gauged by the Chi-squared (χ^2) value. In comparing different fits of the same spectra, the fit with the lowest χ^2 value is usually best, with a value of χ^2 in the range 10^{-5} - 10^{-4} units. Once a clean surface has been fitted, the spectrum from the next incremental metal deposition should be fitted, starting with the same components as the clean surface fit. This procedure is then repeated for subsequent spectra. If the same components do not satisfy the lineshape of the new spectrum, it may be the case that new components need to be added, or others taken away. However it must be noted that although a fit may have a low χ^2 value, and look alright, in order to be of any use at all, the fit must make chemical and spectroscopic sense in the context of the metal-semiconductor material system being studied.

4.7 XPS at the Material Research Institute

4.7.1 Experimental set-up

A schematic description of the Microlab system is given on Figure 4-6. The instrument is comprised of an analysis chamber, a preparation chamber and a custom built metallisation chamber. The vacuum inside the analysis and preparation chambers is maintained by two LN_2 trapped oil diffusion pumps to a base pressure of 10^{-10} mbar while the metallisation chamber is connected to a turbo molecular pump. Samples are loaded into the preparation chamber through the load-lock and can be transferred to the metallisation and analysis chambers by ways of a system of railtrack, linear drive and wobblesticks. The analysis chamber is equipped with a dual anode (Al/Mg) X-ray gun and a concentric hemispherical analyser (CHA), which will be described in more details in the next section. An electron lens is used to collect the photoelectrons from the sample.

The metallisation chamber was specially designed for this work and is described on Figure 4-7. The sample is placed on the manipulator and is shown facing up. A quartz crystal used to monitor the flux of metal atoms thermally evaporated from the Ga and Au sources is shown facing down. The shield function is to prevent metal deposition on the top viewport. Once the metal flux has stabilised the manipulator is rotated 180° so that the sample faces down and is exposed to the metal flux. This design therefore allows controlled *in-situ* deposition of metal onto the sample surface.

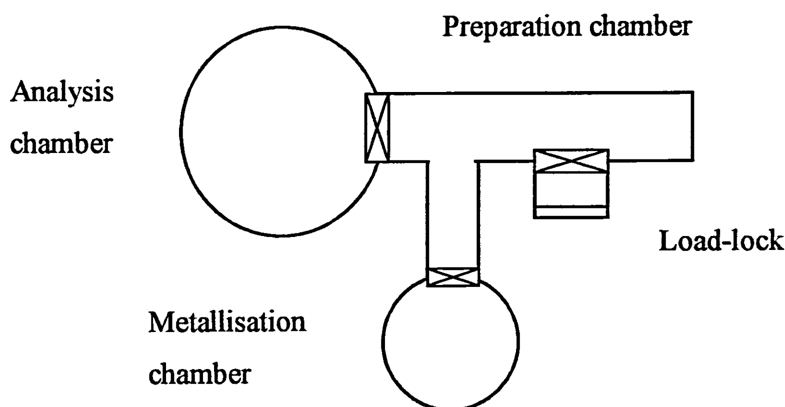

Figure 4-6: schematic of the Microlab set-up (top-view).

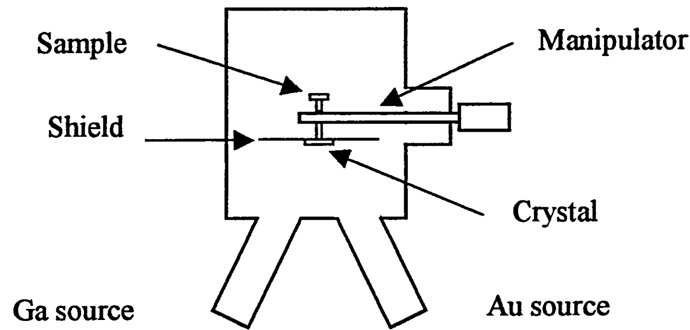

Figure 4-7: side view of the custom-built metallisation chamber of the Microlab.

During the course of this work it was necessary to evaporate Ga onto a heated GaN substrate so the samples were mounted on a low resistivity (0.005 Ωcm) silicon heater plate and held in place by Tantalum clips on specially designed heater stubs that allowed resistive heating of the silicon strip (Figure 4-8). The stub casing acts as an earth contact and the isolated screw passing through the body of the stub acts as the other electrical contact. The sample was heated by passing electric current through the silicon plate. The relationship between applied current and the temperature of the silicon was calibrated by way of an Landmark IV infra-red pyrometer operating at a wavelength of 1.2 μm. An emissivity of 0.4 was used for the silicon. A typical calibration curve is shown in Figure 4-9 with the accuracy of the temperature measurement using this technique estimated to be ±25°C.

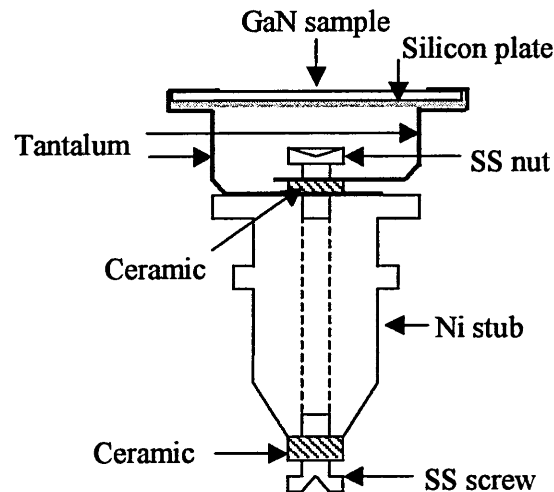

Figure 4-8: heater stub designed for *in-situ* annealing of GaN samples.

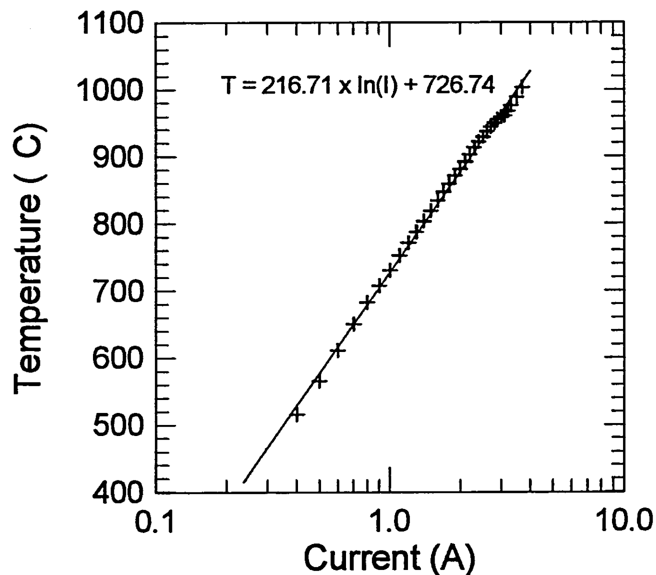

Figure 4-9: temperature versus current calibration curve for the Si plate.

4.7.2 Electron energy analyser

The basic form of a CHA is illustrated in Figure 4-10 and consists of two concentric hemispheres of radius R_1 and R_2. A potential difference is applied between the two hemispheres so that only electrons entering with a selected energy known as the pass energy (E_p) reach the detector array of channeltrons via the two hemispheres.

An electrostatic field is set up within the two plates by applying potentials $-V_1$ and $-V_2$ to the inner and outer plates, respectively, with V_2 greater than V_1. An electrostatic lens focuses the photoelectrons so that they can pass through the entrance slit (width w) on the Herzog plate. The median equipotential surface between the two hemispheres has a radius R_0 and the entrance and exit slits are centred on this surface. The potential V_0 along the equipotential surface is given by[83],

$$V_0 = \frac{V_1R_1 + V_2R_2}{2R_0}$$

[4-24]

The Herzog plate retards or accelerates the electrons to the pass energy and the electrons travel in a circular orbit of radius R_0 through the hemispheres to the exit slit where they are detected. The relationship between analyser pass energy (E_p) and the potential

difference *(ΔV)* across the hemispheres is given by[83],

$$e\Delta V = E_p\left(\frac{R_2}{R_1}+\frac{R_1}{R_2}\right)$$

[4-25]

If the pass energy is kept constant during an experiment, the voltage on the Herzog plate must be scanned in order to obtain an EDC. For example, to scan an energy range of 35-45 eV with a pass energy of 20 eV, the retard voltage would have to vary from 15-25 eV in accordance with the equation[102],

$$E_k = E_p + eV_r$$

[4-26]

In this case the EDC's are acquired in constant analyser energy (CAE) mode and the resolution of the spectra is kept constant for all core levels since the detected electrons all have the same energy, E_p. The resolution of a CHA is given by,

$$\frac{\Delta E}{E_p} = \frac{w}{2R_o} + \frac{(\delta\alpha)^2}{4}$$

[4-27]

Here, w is the entrance slit width, R_0 is the radius of the electrons circumventing the hemispheres and $\delta\alpha$ is the acceptance angle of the analyser. From equation [4-27] it can be seen that the resolution of the analyser can be improved by either reducing the pass energy or the slit width. However, a reduction in the slit width will also reduce the intensity of detected photoelectrons, and hence a compromise between resolution and intensity must be found.

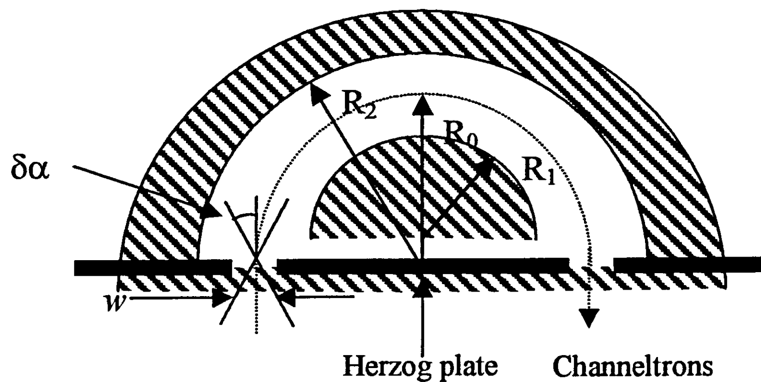

Figure 4-10: details of the concentric hemispherical analyser from the Microlab system. The electron path is represented by the dotted line.

4.8 SXPS at Daresbury laboratory

The experimental set-up of beamline 6.1 used during the SXPS experiment at Daresbury Laboratory is presented on Figure 4-11. The sample holder can be rotated 360° so that the sample can be exposed to the incoming photons or to either of the metal sources. The sample holder also allowed electron bombardment heating of the sample plate. The electron analyser is a cylindrical mirror analyser (CMA) which working principle is similar to the CHA described in the previous section.

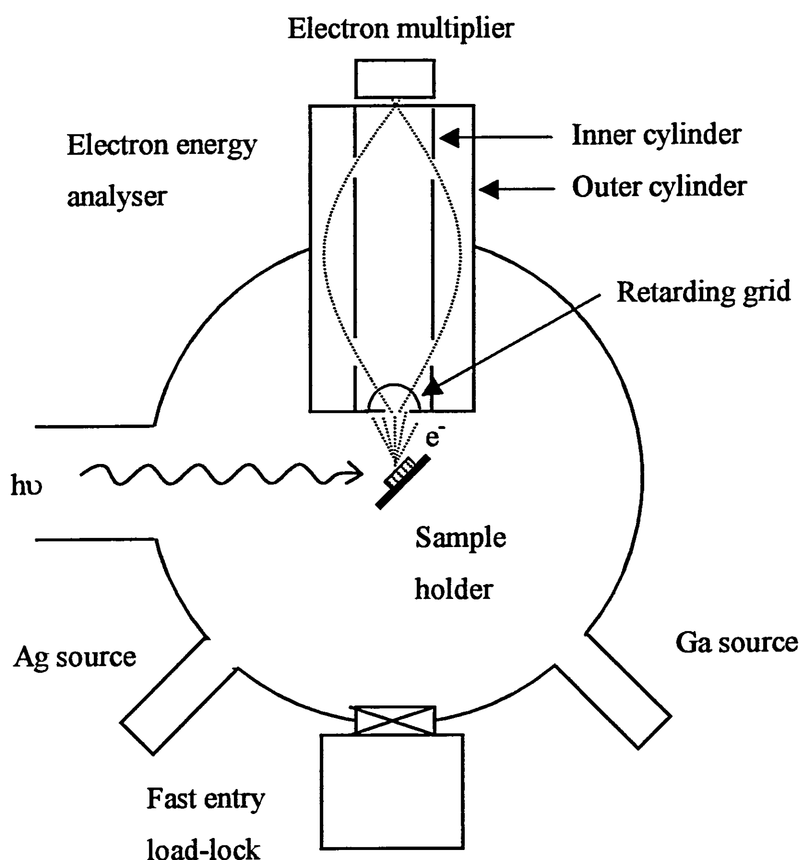

Figure 4-11: schematic of the beamline 6.1 analysis chamber. The dotted lines represent electron trajectories.

Two cylinders are arranged coaxially, with the inner at ground potential and with a negative potential on the outer. Electrons emitted from the sample are retarded or accelerated to the pass energy E_P by the spherical grid and move in field-free space towards an annular aperture in the inner cylinder. Electrons with the right angular

spread $\delta\alpha$ pass into the space between the cylinders and are deflected by the negative potential on the outer cylinder through a second aperture and are collected by an electron multiplier. For small values of $\delta\alpha$ the energy resolution of the CMA is :

$$\frac{\Delta E}{E_P} = 2.75(\delta\alpha)^3$$

[4-28]

4.9 Transmission Electron Microscopy

The cross-section TEM observations were carried out on a Hitachi H800-NA electron microscope operating at 200 keV at Barcelona University. This section gives a brief description of the fundamental principle of TEM and sample preparation.

4.9.1 Principle

Transmission electron microscopy can be used for the structural characterisation of metal-semiconductor interfaces. In the technique of TEM electrons are emitted by a hot tungsten wire and accelerated through a potential difference of ~50-200 kV resulting in fast electrons ($\lambda \sim 5\text{-}2.5 \times 10^{-12}$ m). Three lenses as shown in Figure 4-12 control the beam of electrons. The condenser lens produces a nearly parallel beam that is incident on a very thin sample. The sample must be very thin so that the electrons do not lose energy as they pass through it. The transmitted electrons are collected at the objective lens of the microscope and a magnified image is produced which acts as the object for the projector lens. This lens magnifies the image even further, and projects the final image onto a fluorescent screen or photographic plate. In a TEM micrograph contrast between adjacent areas is produced because the electrons are scattered by differing amounts in areas with differing lattice parameters. The system must be maintained at a high vacuum of ~10^{-7}mbar.

The resolution of the system is essentially defined as the smallest separation of two points in an object that can be distinctly reproduced in the image. The limit of resolution can be given as[103],

$$(\Delta) = 1.22 f\lambda/D$$

[4-29]

where λ is the De Broglie wavelength of the electrons, f is the focal length of the lens and D is the lens aperture diameter. Hence a reduction in the wavelength of the electrons will result in better resolution for a system with fixed dimensions. The De Broglie wavelength can be given as,

$$\lambda = \frac{h}{\sqrt{2mE}}$$

[4-30]

hence an increase in the energy of the electrons (E) will result in a reduction in the wavelength of the electrons. Increasing the applied potential difference can therefore enhance the resolution in a TEM. A typical resolving power of a TEM is ~0.5 nm while the best attain < 0.2 nm[104].

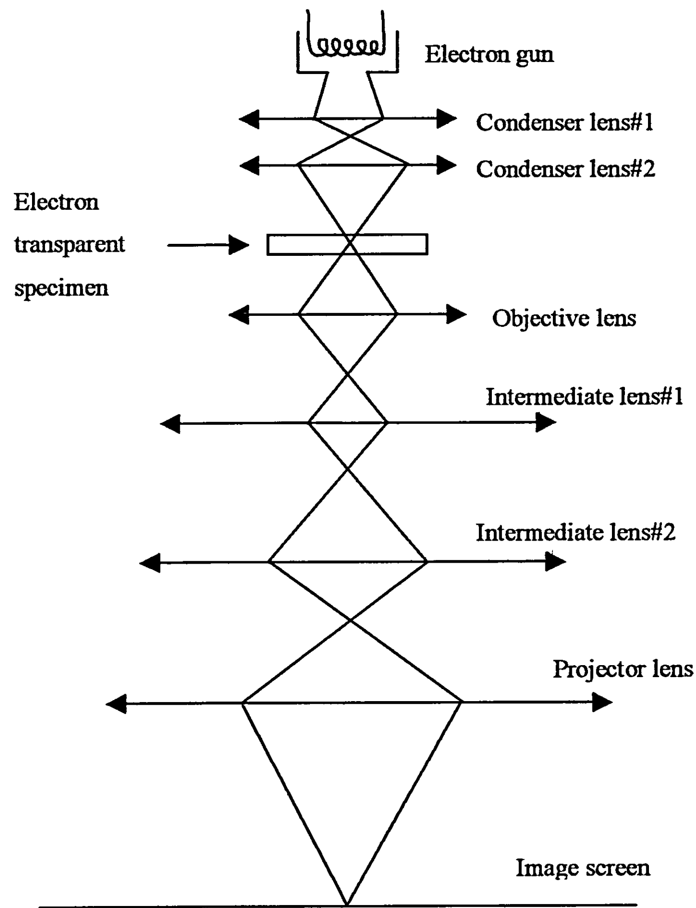

Figure 4-12: ray diagram of the main components of a transmission electron microscope (TEM)

4.9.2 Sample preparation

Cross sectional samples were produced by cutting the metallised samples resulting from the XPS experiments into thin strips and then bonding them together metal overlayer to metal overlayer as in Figure 4-13. The sandwiches were then subjected to a mechanical flat polish, which reduced them to a thickness of about 50 μm. A subsequent mechanical concave polish reduced the thickness further to 20-25 μm. Once at this thickness, the sample was mounted on to a copper ring of 3.05 mm diameter and centred over a 600 μm diameter hole in the middle of the ring. It was then transferred to a Gatan ion milling machine where it was Ar^+ etched until it became perforated. During ion milling, a low energy (4 keV), low intensity (0.15 mA) ion beam was used. Once the samples had been ion milled to a stage where they were transparent, they could be transferred to the electron microscope for TEM studies.

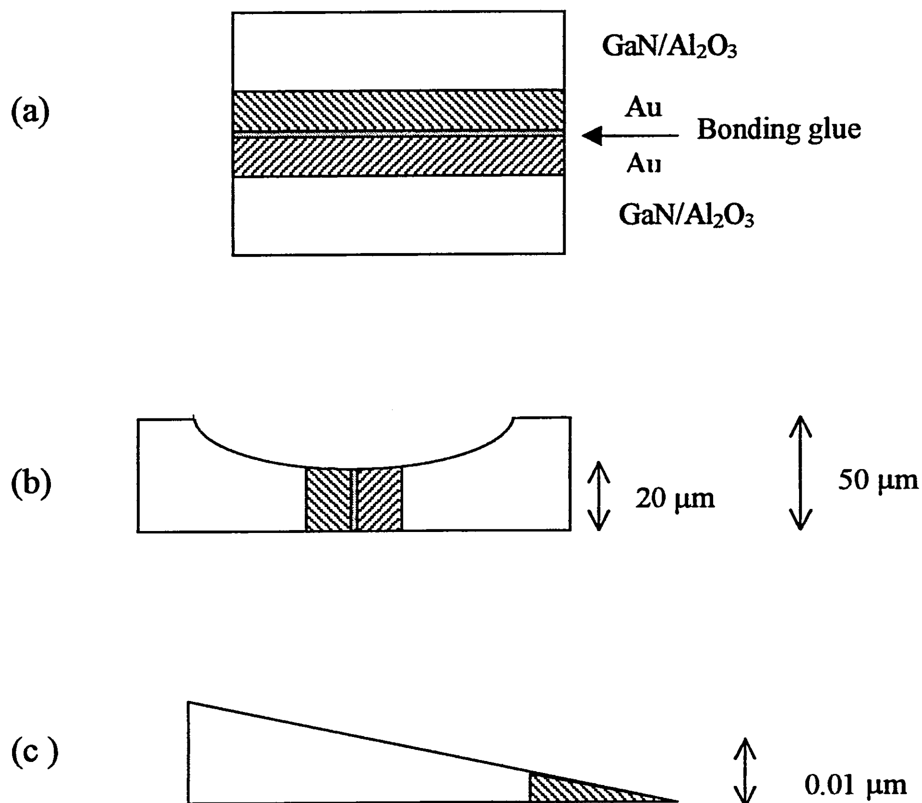

Figure 4-13: schematic of TEM sample preparation, (a) "sandwich" of two Au-GaN contacts, (b) after mechanical polishing and (c) after ion beam milling.

4.10 Transport measurement

The experimental set-up of the I-V measurement rig is schematically described on Figure 4-14. Two sharp probes are placed into contact with the processed sample, one probe on the diode to be measured and the other on the large area contact used as an Ohmic contact. Micrometric Verniers and binoculars allow accurate positioning of the probes. A voltage source applies a bias across the probes and a Keithley pico-ammeter measures the current flowing between the diode and the Ohmic contact. The voltage source and the pico-ammeter are controlled by a personal computer. The software allows the selection of voltage range, step size, acquisition time and noise reduction filters. Finally, the I-V characteristic is saved as an ASCII file.

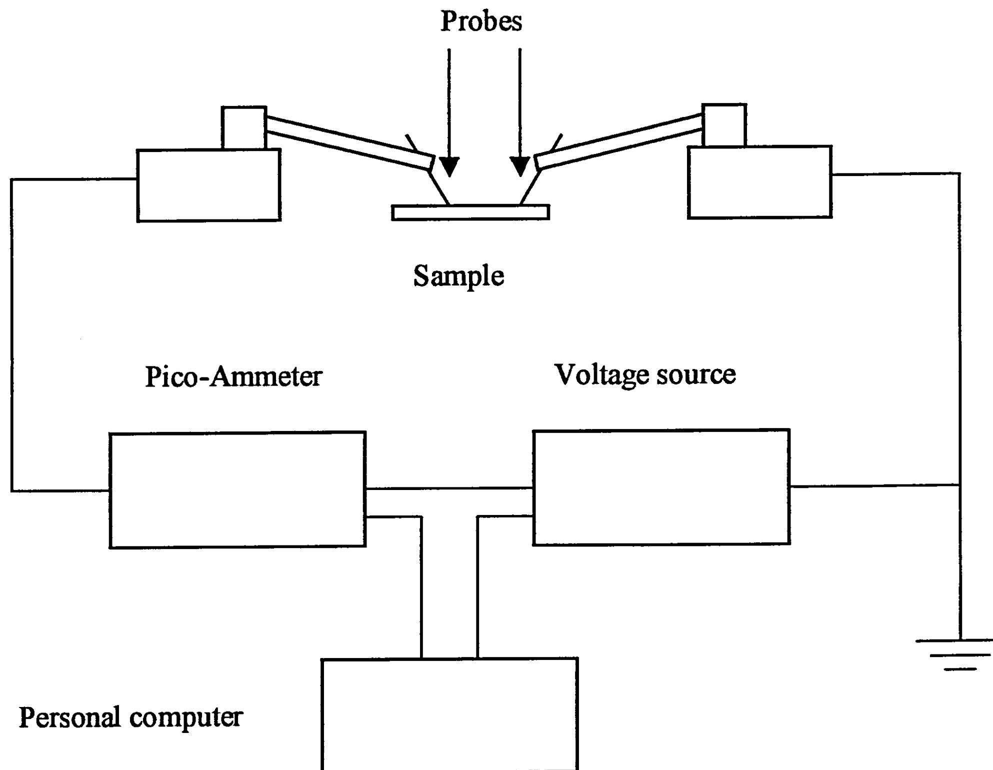

Figure 4-14: schematic of the I-V measurement experimental set-up.

Chapter 5: Cleaning of GaN

5.1 Introduction

Pre-metallisation surface treatment is a crucial step in semiconductor-metal contact formation. For practical contacts, used in device manufacture, metal layers are normally deposited without *in-situ* cleaning in UHV. The typical procedure consists of degreasing in organic solvents followed by acid etching. Ellipsometry studies[105] conducted on GaN epilayers showed that this treatment is efficient in removing a 20-50Å thick overlayer. 50 % of this layer consists of transparent organic and inorganic contamination, which was readily removed by H_2O and solvents while the other half, presumably oxide, was removed by the acid. We have seen in Chapter 2 that a wide range of chemical solutions have been used in an effort to improve the electrical behaviour of practical contacts[37-46] to GaN. In a recent review[47], it was found that HF:DI H_2O solution yielded the best results in terms of removing O and C contamination from the surface.

Practical surfaces are, however, far from being atomically clean. Even if most of the native oxide layer has been removed by the chemical treatment, the GaN surface has to be exposed to air prior to metal deposition, thus leading to re-oxidation of the surface. As discussed in section 2.2, atomically clean GaN surfaces have been produced by a number of *in-situ* cleaning techniques, such as gallium deposition, reduction and re-evaporation. Several groups[48-51] have used this technique, also referred to as Ga reflux, to prepare clean, well ordered GaN surfaces. The underlying principle is highlighted in Figure 5-1: Ga atoms are deposited onto the contaminated GaN surface (a), Ga atoms bond with O atoms while C contaminants 'float' on top of the metallic Ga layer[52] (b), both O and C are removed during re-evaporation, leaving a clean GaN surface (c). The substrate temperatures quoted in the literature for step (c) range from 700°C to 950°C. This wide variation may be due in part to the difficulty of measuring temperature accurately in UHV. Ga deposition has been conducted at room temperature[49], at the same temperature as for step (c)[48,50] and intermediate temperature[48,51].

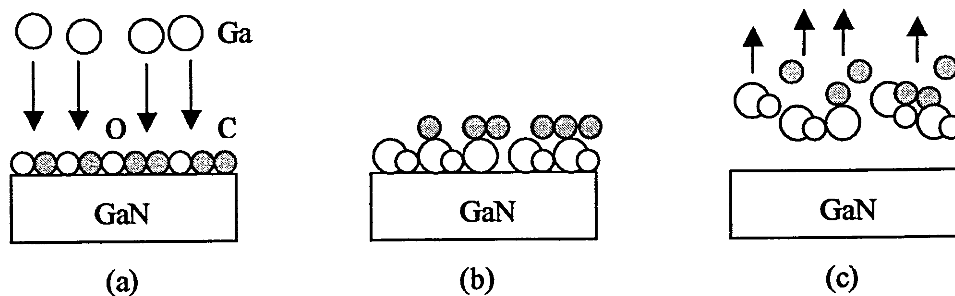

Figure 5-1: the three steps of the Ga reflux cleaning process, (a) Ga deposition, and (b) reduction and (c) re-evaporation.

In this chapter, we present an SXPS and XPS investigation of three, increasingly complex, cleaning procedures. The first surface preparation method is similar to that used in practical contact formation and consists of solvent degreasing and acid etching in an HF solution. The second method involves high temperature ($T \approx 600°C$) annealing in UHV while the third surface under investigation was cleaned by the Ga reflux method. Finally, transport measurements from Ag-nGaN contacts formed on the third surface are presented and compared to the photoemission results.

The 1.8 μm thick GaN epilayer used during the SXPS and I-V experiments was grown by MBE on sapphire. The layer was n-type, non-intentionally doped with an

electron concentration of about $6x10^{16}$ cm^{-3} and a mobility of 240 $cm^2V^{-1}s^{-1}$ at room temperature. The XPS experiments were conducted on 1.1 μm thick GaN epilayers, grown on sapphire by MOCVD; with an electron concentration of $2x10^{15}$ cm^{-3} and a mobility of 41 $cm^2V^{-1}s^{-1}$ (at room temperature), as determined by Hall measurement.

5.2 Wet chemical etching in an HF solution

Figure 5-2 shows the effect of HF etching on the elemental composition at the surface of GaN. The surface labelled 'oxidised' was merely cleaned in organic solvents (acetone, ethanol and H_2O) while the sample labelled 'as etched' was in addition dipped in a HF solution for 1 minute. The HF (45%, *Aristar* grade) was diluted 10 times in de-ionized (18 MΩcm) water.

The O *1s* to Ga *3d* ratio following the HF dip decreases from 0.5 to 0.3 at normal emission and from 0.81 to 0.53 at 60°off normal emission, indicating that O contamination has been effectively reduced at the surface. The amount of C, however, remains the same. The N *1s* normalised intensity from the oxidised surface is less at 60°off normal emission than at normal emission, suggesting that the surface is Ga rich. The ratio increases after etching, possibly indicating that the surface is becoming more stoichiometric. One of the samples also showed signs of Na contamination, which the HF etch removed.

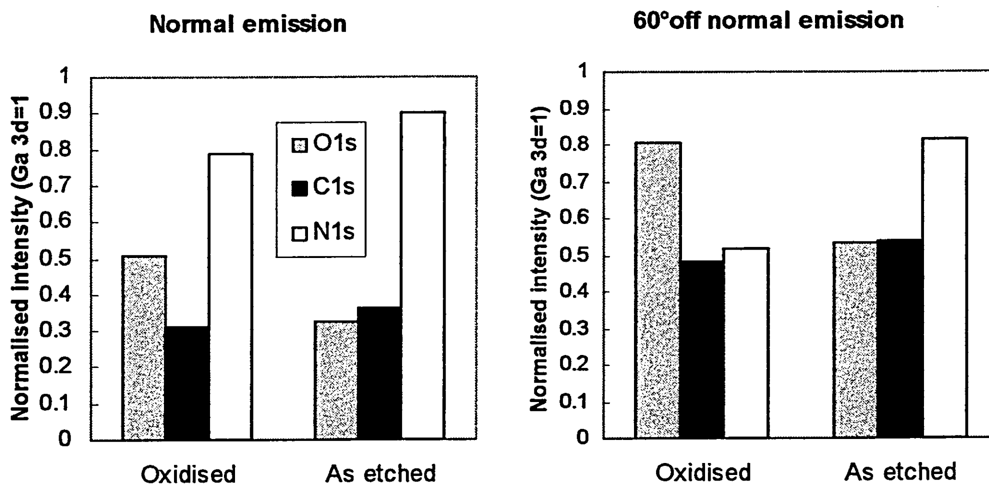

Figure 5-2: normalised XPS core level intensity from the oxidised surface and the HF etched surface at normal and 60°off normal emission. The intensities have been weighted by an empirical sensitivity factor and normalised to the Ga *3d* intensity.

Figure 5-3 shows that etching altered the peak shape of the O *1s* core level, indicating a change in the chemical phases of O at the surface, possibly partial removal of the native oxide. The difference in the peak shapes at normal and 60°off normal emission also suggests that O from the uppermost layers exists in a different chemical state to those underneath. This could be interpreted by a layer of adsorbed molecules, such as water vapour, on top of the native oxide.

The effect of HF etching on the Ga 3d core level is shown on Figure 5-4. The SXPS raw spectra have been fitted with Voigt functions, using the curve fitting software, TCFIT. A Lorentzian parameter of 0.18 eV was used. Several groups have used Lorentzian parameter ranging from 0.1 eV to 0.2 eV[106,107,108,109] to fit Ga 3*d* core level SXPS scans taken on GaAs material, but to the best of our knowledge, no such work has been done on GaN. The resulting Gaussian broadening was 0.86 eV.

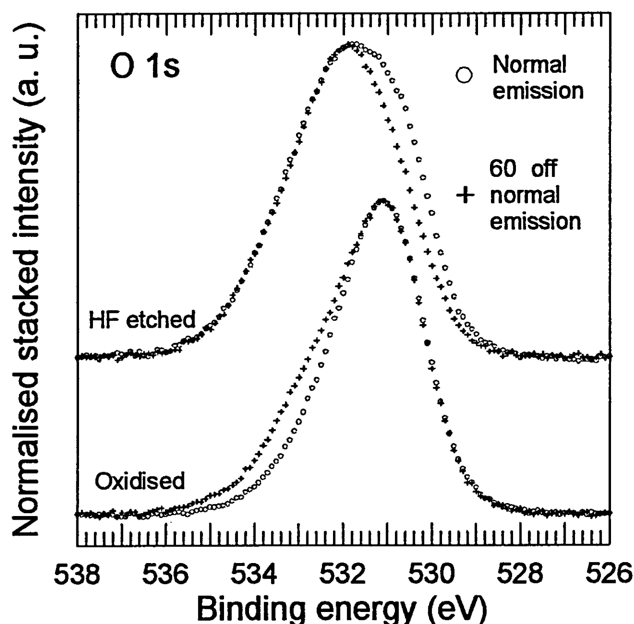

Figure 5-3: O *1s* XPS spectra at normal emission (o) and 60°off normal emission (+) from the oxidised surface and the HF etched surface.

The number of components was kept to a minimum and both spectra were fitted with two peaks. The main peak is thought to be related to Ga-N bonding. The secondary peak on the low kinetic energy side of the main peak might arise from Ga-O bonding as it is reduced by the etch, although the energy offset between the two components is different: 0.6 eV for the oxidised surface and 0.87 eV for the etched surface.

A possible interpretation is that several chemical phases of Ga oxide could coexist on the oxidised surface such as Ga_2O_3, GaOOH or $Ga(OH)_3$ resulting in a large component 0.6 eV away on the low kinetic energy side of the Ga-N peak. Some of these oxide phases could then be etched away by the HF dip, resulting in the observed drop of the O *1s* normalised intensity and changes in the O *1s* peak shape. As the surface was exposed to air between etching and loading in UHV, it is likely that a fresh oxide layer was formed, containing oxide states different from the thick original oxide layer, thus resulting in a smaller secondary component 0.87 away from the Ga-N peak. The Ga-N peak was also shifted 0.25 eV to higher kinetic energy by the HF etch.

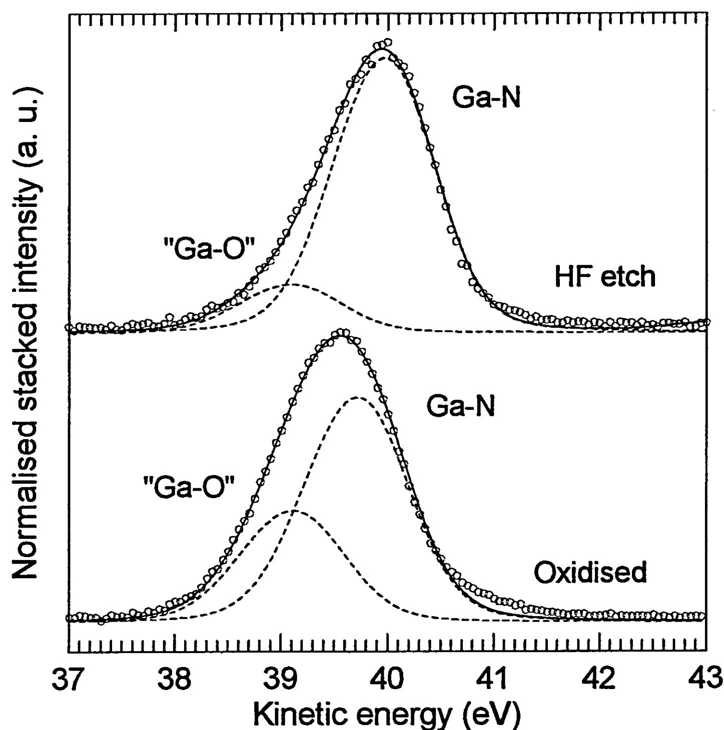

Figure 5-4: Ga *3d* SXPS core level spectra for the oxidised and HF etched surfaces. The scans have been recorded using a photon energy of 66 eV and the kinetic energy scale has been corrected so that the energy position of the Fermi level is the same for both spectra (61 eV). The raw data (open circles) have been fitted with two components (dashed line). The resulting fit is shown as a solid line.

5.3 UHV annealing

Figure 5-5 gives the intensity of the N *1s* and O *1s* core levels normalised to the Ga *3d* core level intensity (intensities extracted from XPS scans) after annealing at 600°C (±50°C) in UHV for 10 min. The O *1s* normalised intensity is lowered to 0.15 at normal emission and 0.38 at 60° off normal emission, indicating that the amount of oxygen contamination is less than for the chemically treated surface. This is in good agreement with Auger Electron Spectroscopy studies performed by Smith *et al.*[110].

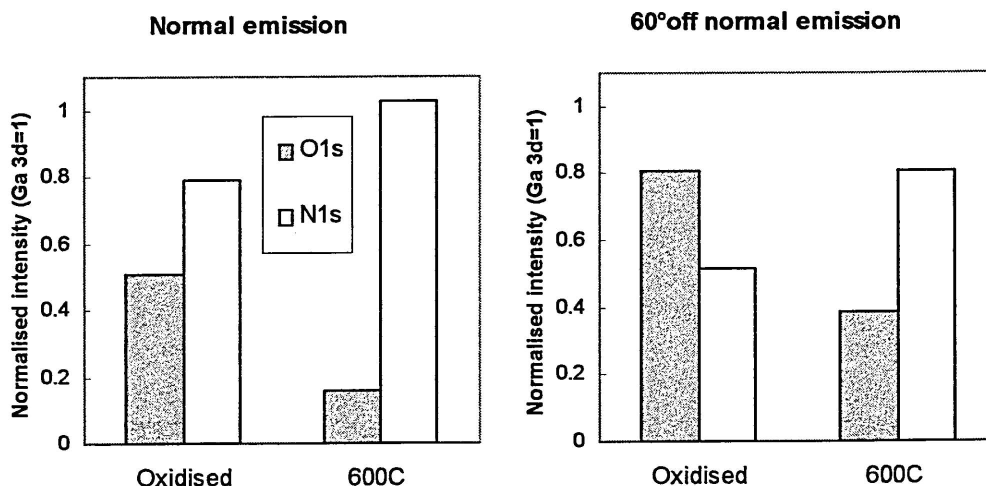

Figure 5-5: normalised N *1s* and O *1s* core level intensity from the oxidised and 600°C annealed surfaces at normal and 60°off normal emission. The intensities have been weighted by an empirical sensitivity factor and normalised to the Ga *3d* intensity.

Figure 5-6 shows the SXPS spectra of the Ga *3d* core level from the oxidised surface and after annealing at 830°C. The 830°C spectrum has been fitted with the same two components as the spectra from the etched surface of Figure 5-4. Annealing at 830°C causes the Ga-N component to shift by +0.7 eV to high kinetic energy. As the valence band spectra, shown on Figure 5-7, display a similar shift, it is likely that this shift is a rigid Fermi shift corresponding to upward band bending at the surface. Upward band bending has been observed before as a result of annealing in UHV[111] and has been tentatively attributed to the creation of Ga vacancies, which act as acceptor states.

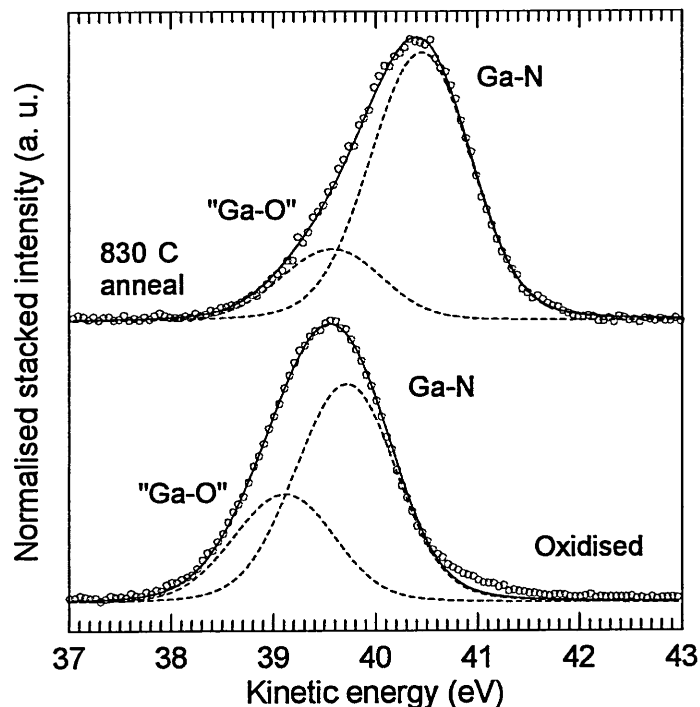

Figure 5-6: Ga *3d* SXPS core level spectra for the oxidised and 830°C annealed surfaces. The scans have been recorded using a photon energy of 66 eV and the kinetic energy scale has been corrected so that the energy position of the Fermi level is the same for both spectra (61 eV). The raw data (open circles) have been fitted with two components (dashed line). The resulting fit is shown as a solid line.

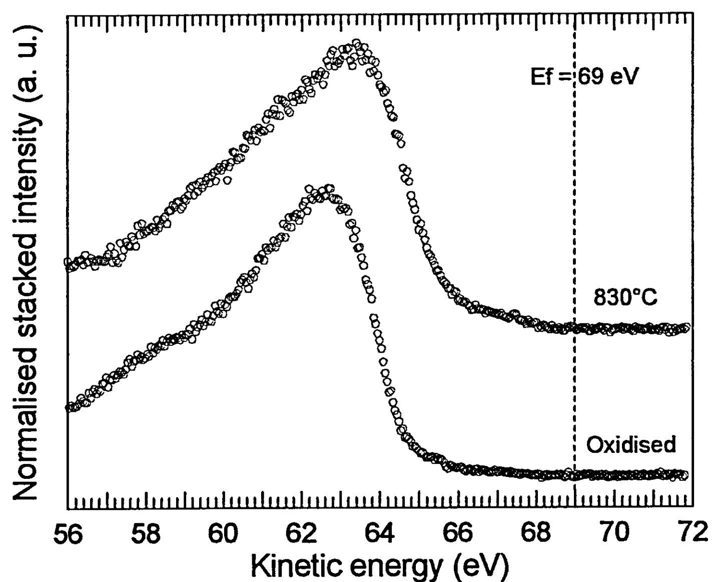

Figure 5-7: SXPS valence band spectra for the oxidised and 830°C annealed surfaces. The scans have been recorded using a photon energy of 74 eV and the kinetic energy scale has been corrected so that the energy position of the Fermi level is the same for both spectra (69 eV).

The secondary component appears slightly larger for the 830°C surface than for the etched surface (Figure 5-4), which suggests that it might not be oxide related as the O content is reduced by the anneal. Alternatively, chemisorbed O could be incorporated into the oxide layer during the annealing process[111], which would explain the increased intensity of the secondary component. According to this interpretation, the drop in O content at the surface could be explained by the desorption of physisorbed O during the anneal and/or removal of O chemically bonded to N rather than Ga. Figure 5-8 shows that annealing at 600°C results in a significant reduction of the high binding energy shoulder of the N *1s* XPS peak, which could be attributed to the diminution of a N-O component.

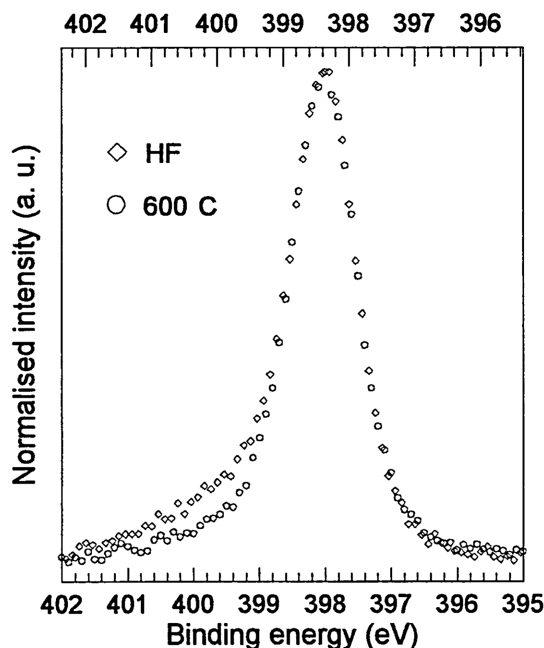

Figure 5-8: N *1s* XPS spectra, taken at 60° off normal emission after HF etching (diamond shape) and annealing at 600°C in UHV (open circle). The annealed scan is plotted using the top binding energy x-axis which has been shifted 0.35 eV so that the two peaks are superposed.

5.4 Ga reflux cleaning

Figure 5-9 compares the elemental composition, extracted from XPS scans, at the surface of the oxidised sample and the sample subjected to 2 cycles of cleaning by the Ga reflux technique: 30 Å of metallic Ga were deposited onto the sample, which was held at a temperature of 600°C, then the sample temperature was ramped up to 900°C in order to re-evaporate the deposited Ga. The O *1s* normalised intensity is drastically reduced by the cleaning technique, such that the amount of O left on the surface is barely above the detection threshold of the instrument (0.1-1 %). The C *1s* normalised intensity is also significantly reduced although not to the same extent as the O *1s* normalised intensity.

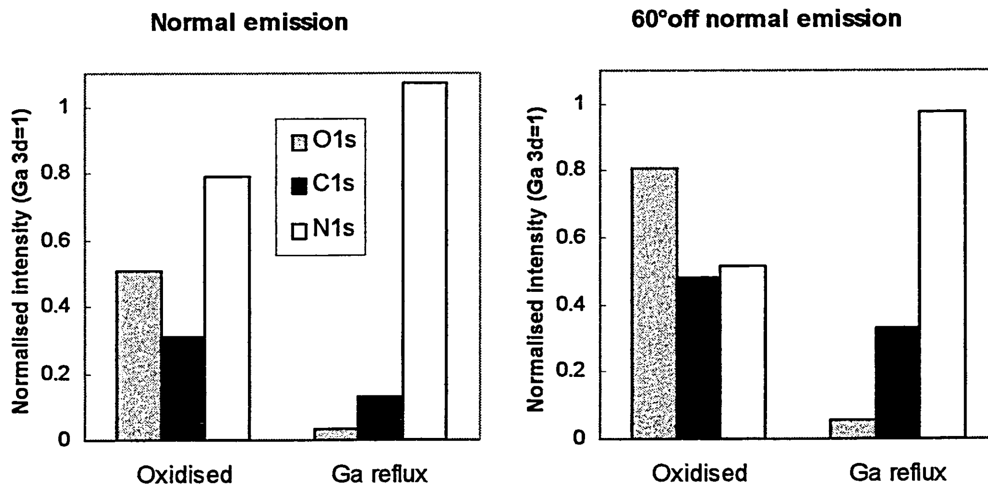

Figure 5-9: normalised XPS core level intensity from the oxidised surface and the surface cleaned by the Ga reflux technique at normal and 60°off normal emission. The intensities have been weighted by an empirical sensitivity factor and normalised to the Ga *3d* intensity.

The cleaning process has in addition caused a Fermi shift to lower binding energy, as indicated by the peak position of the Ga *3d* and N *1s* core level on Figure 5-10. The binding energy shift from HF etch to Ga reflux for both core levels is 0.45 eV.

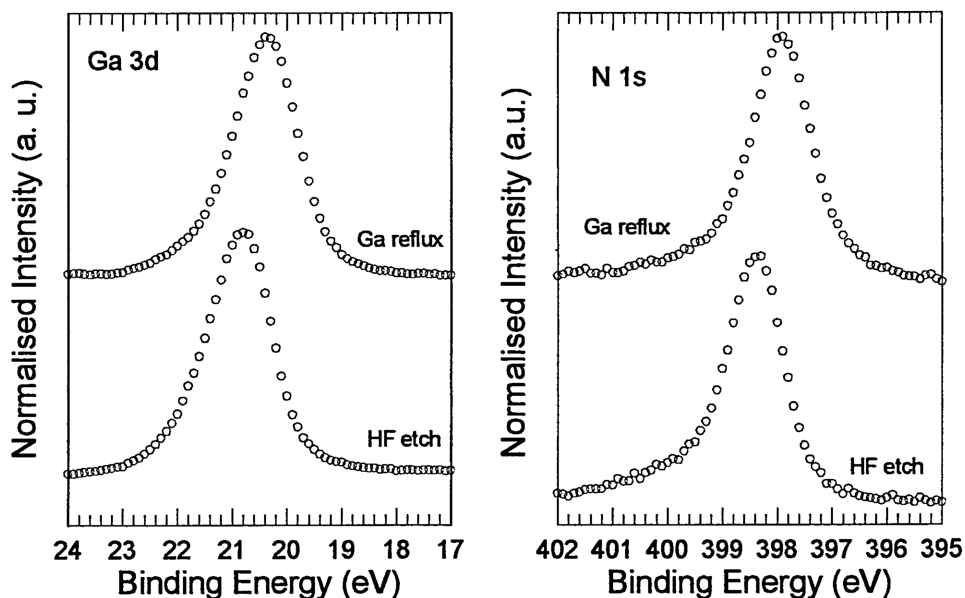

Figure 5-10: Ga *3d* and N *1s* XPS spectra, taken at 60° off normal emission after HF etching and 2 cycles of Ga reflux cleaning.

In order to gain more insight into the origin of this 0.45 eV Fermi shift, a SXPS experiment was performed which focussed on the effect of metallic Ga deposition and subsequent re-evaporation. Figure 5-11 shows the evolution of the SXPS Ga 3*d* core level spectra throughout this experiment. The sequence of surface treatments was as follows:

a) The sample was dipped in HF:DI H_2O solutions (1:10) and (1:40) for 1 and 2 min., respectively.

b) 40Å of high purity Ga were deposited at 600°C, the sample was then annealed at 700°C for 10 min.

c) As metallic Ga remained on the surface, the sample was annealed at 775°C for another 10 min.

d) Second 40Å Ga deposition at 600°C and anneal at 775°C.

e) 30Å Ag deposition at room temperature.

It can be noted that the temperature at which Ga desorption is achieved is considerably lower than for the XPS experiment. This is probably a consequence of the different temperature measurement methods, pyrometer for the XPS experiment and thermocouple for the SXPS experiment.

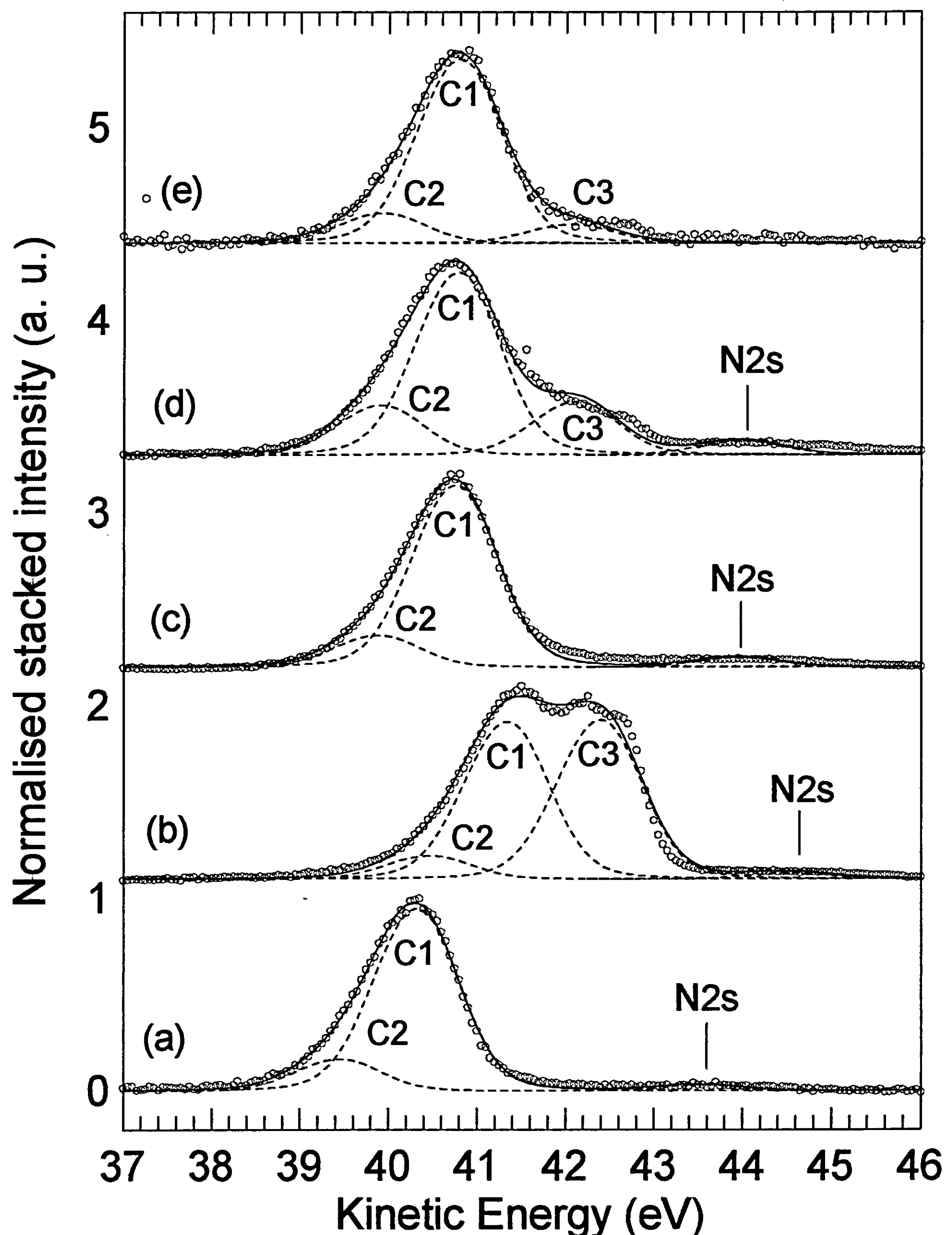

Figure 5-11: SXPS spectra of the Ga *3d* core level taken using a photon energy *h* ν = 66 eV from the GaN surface after: (a) HF etching, (b) 40Å Ga deposition at 600°C and anneal at 700°C, (c) anneal at 775°C, (d) second 40Å Ga deposition and anneal at 775°C and (e) Ag deposition.

The two components labelled C1 and C2 used to fit the HF etched peak are the same as in section 5.2. The energy offset of 0.87 eV between the two components was kept constant while fitting the raw data from the other steps of the experiment. A third component C3 was introduced 1 eV on the high kinetic energy side of the main component for scans (b), (d) and (e). The main component C1 is thought to be related to

Ga atoms bonded to N while the higher kinetic energy satellite C3 is likely to arise from Ga to Ga bonding[61,55]. The lower energy satellite C2 could be caused by Ga–O bonding[49,52], or it could be a surface component. The N 2*s* peak (although of very low intensity due to its small ionisation cross-section at this photon energy) is also apparent 3.2 eV away from the Ga-N peak, as has been reported previously[52,112]. The deposition of metallic Ga on the surface causes the Ga-N component (C1) and its low energy satellite C2 to shift by +1.0±0.1 eV (plot (b)) toward higher kinetic energy. Following the 775°C anneal, and the removal of metallic Ga, the two components shifted back by -0.6±0.1 eV (plot (c)). The second Ga deposition and following anneal at 775°C produced a negligible shift (0.05 eV), even with a small coverage of Ga remaining (plot (d)). Similarly, no further shift was resolved following the deposition of 30Å of Ag (plot (e)), implying that the Fermi level is firmly pinned.

Valence band scans, obtained following each treatment stage are shown in Figure 5-12. Comparing the evolution of the valence band with the Ga 3*d* core level (Figure 5-11), it is clear that shifts are generally comparable in trend and magnitude. This, added to the fact that the N *2s* core level seems to follow the shifts undergone by the Ga *3d* peak, suggests that the shifts observed are genuine Fermi shift and correspond to rigid band bending at the surface. Table 5-1 gives a summary of the shifts undergone by the Ga *3d* core level, from the oxidised surface to Ag deposition. The total shift from oxidised surface to Ag deposition is 0.7 eV while the shift from HF etched surface to Ga reflux surface is 0.45 eV, in excellent agreement with the XPS results presented earlier.

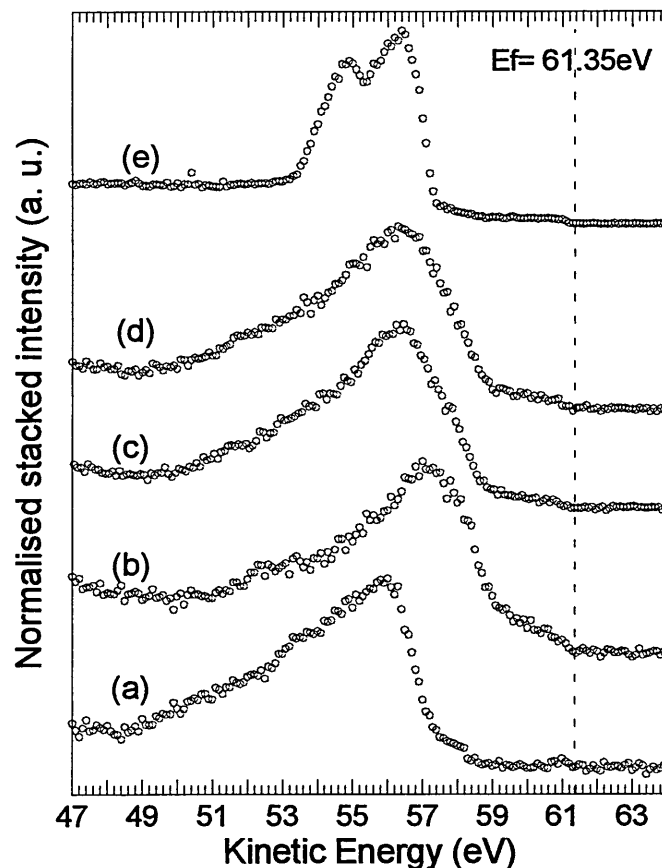

Figure 5-12: SXPS valence band spectra taken using a photon energy $h\nu = 66$ eV from the GaN surface after: (a) HF etching, (b) 40Å Ga deposition at 600°C and anneal at 700°C, (c) anneal at 775°C, (d) second 40Å Ga deposition and anneal at 775°C and (e) Ag deposition.

Surface treatment	Kinetic energy shift (eV)	Absolute kinetic energy shift (eV)
Oxidised		0.0
HF etch	+0.25	+0.25
40 Å of Ga at 600°C and 700°C anneal	+1.0	+1.25
775°C anneal	-0.6	+0.65
40 Å of Ga at 600°C and 775°C anneal	+0.05	+0.70
30 Å of Ag at RT	0.0	+0.70

Table 5-1: summary of the relative and absolute kinetic energy shifts of the Ga-N component from the oxidised surface to the final Ag deposition.

The partially reversible band bending and subsequent pinning of the Fermi level can be interpreted with a combination of the Metal Induced Gap State (MIGS) model and the Unified Defect Model (UDM) described in section 3.1.3. MIGS are associated with the tails of the conduction electron wave functions in the deposited metal penetrating into the semiconductor. They can be created at the interface in sufficient density to replace any intrinsic electron states which might have been present on the free surface and pin the Fermi level[67]. Considering the origin of MIGS, the pinning of the Fermi level is a reversible event: removal of the metal would cause the surface to revert to its intrinsic states. One interpretation is that the initial Ga deposition creates MIGS at the interface as well as irreversible structural defects, both factors contributing to produce a shift in the Ga3*d* core level of 1 eV towards higher kinetic energy. The subsequent 775°C anneal removed the Ga and therefore the MIGS, not only causing a shift of 0.6 eV to lower energy but possibly also creating more defects, since further Ga and Ag metallisation left the Fermi level unchanged.

5.5 Ag contacts: transport measurements

A thick layer (>500 Å) of Ag was deposited *in-situ* at the end of the SXPS experiment and circular diodes (diameters of 170 μm, 220 μm, 440 μm, 640 μm and 880 μm) were then fabricated using conventional lithography. The Ohmic contact was provided by the large area gold contact deposited before the SXPS experiment in order to prevent surface charging.

The contacts clearly exhibit rectifying behaviour as shown on Figure 5-13. The Schottky parameters, zero-bias barrier height and ideality factor, have been extracted by fitting the linear region of the forward current curve with equation [3-35] for diodes with a linear region large enough to permit an accurate fit (linear for 2 or more decades). The I-V characteristics of the best diode (with the lowest ideality factor of 1.56), and a typical diode where determination of the Schottky parameters is impossible are given in Figure 5-13 (a) and (b), respectively. About half of the diodes measured belong to the latter case, some of them even having Ohmic-like I-V characteristics.

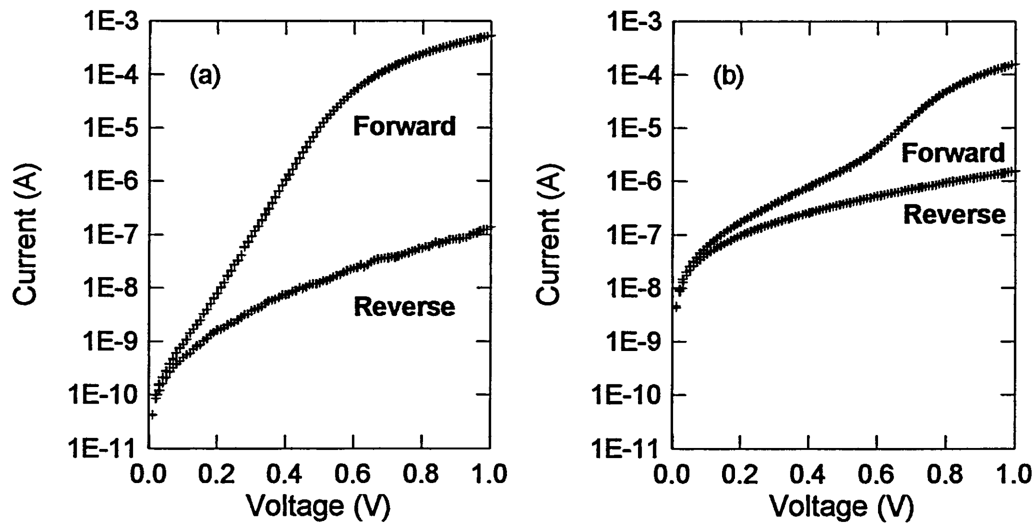

Figure 5-13: I-V characteristics of (a) the best and (b) a typical Ag-nGaN circular diodes (diameter 170 μm). The ideality factor and zero-bias barrier height extracted from (a) are 1.56 and 0.80 eV, respectively.

It is worth noting that small diameter diodes (170 μm and 220 μm) tend to yield better I-V curves than large diameter diodes. The curves of Figure 5-13 display evidence of recombination and tunnelling current at low forward bias which is more apparent for the typical diode. The reverse current is also more important than expected from equation [3-32]. This is probably due to generation and tunnelling currents. Figure 5-14 shows the evolution of the I-V curve of a typical diode with temperature. The thermionic emission current steadily decreases with decreasing temperature, as expected from equation [3-32], but the fact that there is still a significant amount of current even at 13 K, confirms the presence of recombination and tunnelling contributions to the total current. As seen in sections 3.2.2 and 3.2.3 (equations [3-27] and [3-29]), these transport mechanisms are far less temperature dependant than thermionic emission.

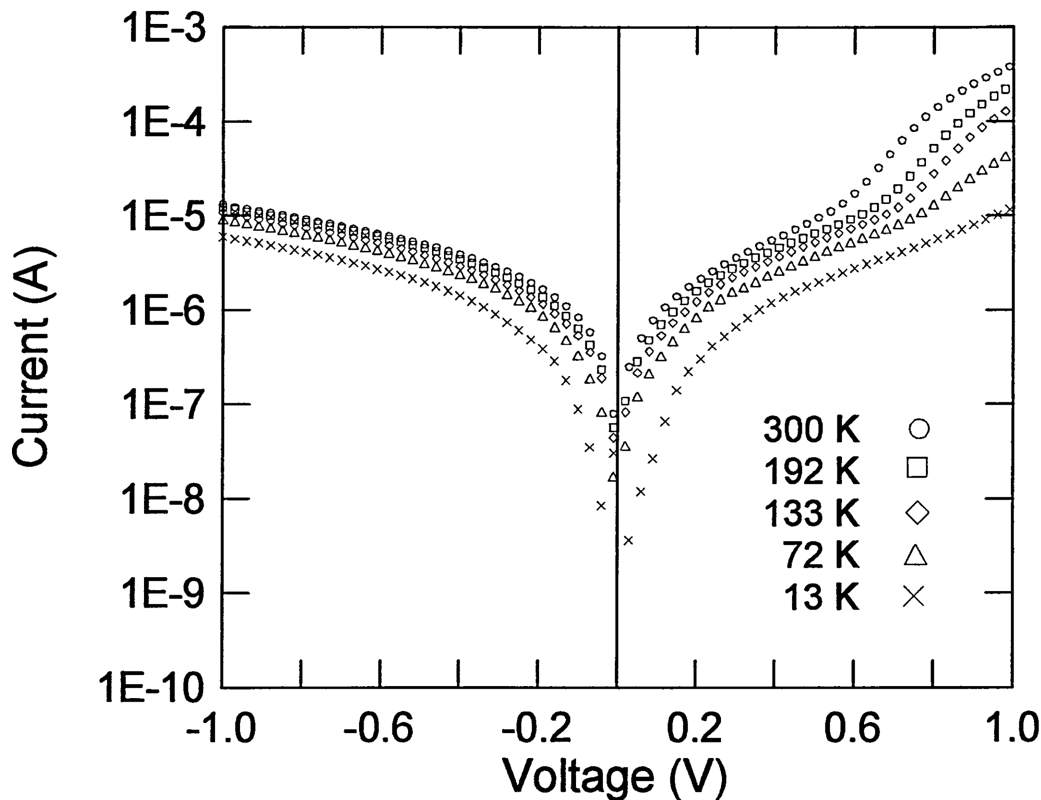

Figure 5-14: I-V characteristics of an Ag-nGaN Schottky diode at various temperatures.

The zero-bias barrier height and ideality factor of all the diodes from which determination of the Schottky parameters was possible are given in Figure 5-15. The barrier heights and ideality factors range respectively from 0.52 eV to 0.80 eV and 1.56 to 3.35. The measured barrier heights are in reasonable agreement with the 0.7 eV upward band bending observed by XPS. The departure from ideality is attributed to tunnelling and recombination currents. Figure 5-15 also shows that ideality factor and zero-bias barrier heights are correlated. The high barriers correspond to low ideality factors, which is to be expected since tunnelling and recombination currents lower the measured barrier because of the extraction method. This wide range of values for both Schottky parameters has been observed before for Ag-nGaN and Pb-nGaN diodes[50] and has been interpreted in terms of laterally non-uniform Schottky barriers[113], the origins of which remain an open question. It is possible that the high density of threading dislocations caused by the substrate lattice mismatch results in a random distribution of surface point defects acting as tunnelling and recombination centres. Structural defects have been put forward as a possible origin of tunnelling and recombination currents in

metal/semiconductor systems such as Au-Si-GaAs[114] or metal-InAlAs[115,116]. This random distribution of tunnelling and recombination centres could explain the large differences in transport characteristics observed from diode to diode as well as the fact that large dots are more likely to have a higher contribution from tunnelling and recombination currents than small area contacts.

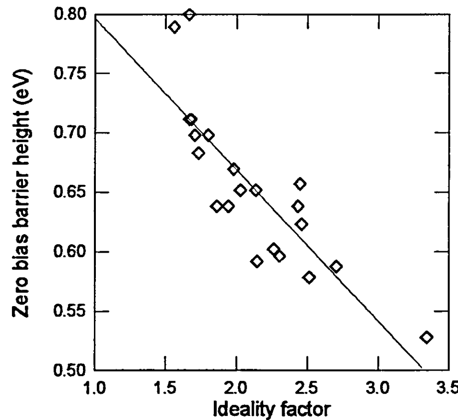

Figure 5-15: zero-bias barrier height versus ideality factor for a number of Ag-*n*GaN Schottky diodes. The solid line is a least-square fit to the data points.

The variation of the zero-bias barrier height with the ideality factor has prompted researchers to find a better method to determine the barrier height. Wagner *et al.*[78] proposed a way of finding the flat-band barrier height from the ideality factor and the zero-bias barrier height (equation [3-43]), thus providing a more universal value for the barrier height, independent of tunnelling and recombination effects. Alternatively, Kampen and Mönch[50,113] found that the dependence of the barrier height on the ideality factor was roughly linear, so that by extrapolating the linear fit to the value of $n=1.01$ (where the departure from ideality is only due to image force lowering) one would obtain a value of the barrier height free of recombination and tunnelling effects. The flat-band barrier height method has been used widely in the past, while the extrapolation method is much more recent. Since the contacts studied in this work present a linear correlation between barrier height and ideality factor (Figure 5-15), a comparison of the two methods is attempted on Figure 5-16 where only results from diodes with ideality factors less than 2 have been used. The flat-band barrier height distribution is fairly constant although the spread in values is quite large (0.15 eV). The average flat-band barrier height is 1.21 eV while the extrapolated barrier height is 0.92 eV. Since Ag

possesses a relatively low work function (4.1 eV), both these values seem much higher than expected according to the published results presented in Figure 2-1 and Table 2-6. It is probable that the high ideality factors observed in this work make it difficult for these methods to yield realistic values. As a result, the zero-bias barrier height of the best diode and the mean barrier height of diodes with ideality factors lower than 2 seem more realistic and representative. These values are given in Table 5-2.

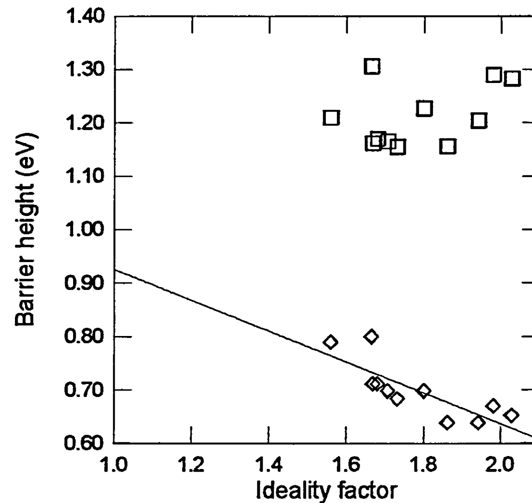

Figure 5-16: distribution of the zero-bias barrier height (diamond shapes) and flat-band barrier height (squares) versus ideality factor for Ag-nGaN Schottky diodes. The solid line is a least-square fit to the data points.

Parameter	Mean	Standard deviation	Best diode
ϕ_{b0} (eV)	0.70	0.054	0.80
n	1.78	0.15	1.56

Table 5-2: summary of transport measurements on Ag-nGaN diodes. Statistics are derived from 11 diodes.

5.6 Summary

In this chapter we have studied the effect of three different, increasingly complex surface treatments on the GaN surface. The following points can be made:

i. Wet chemical etching, performed using a HF:DI H_2O solution, reduces the amount of O contamination at the surface but fails to remove C contamination. Additionally, etching causes a 0.25 eV upward band bending.

ii. UHV annealing lowers the amount of O further, possibly by removing adsorbed molecules and O chemically bonded to N. Annealing the oxidised surface at 830°C produces a 0.7 eV upward band bending, while annealing the HF etched surface at 600°C results in a 0.35 eV upward band bending.

iii. The Ga reflux cleaning method reduces O contamination to levels barely detectable by XPS and causes a significant drop of C contamination. The Ga reflux cleaning also causes an upward band bending of 0.45 eV. Ga deposition at 600°C induces a 1.0 eV upward band bending from the HF etched surface, which corresponds to the formation of a Schottky barrier. Upon desorption of the Ga, the bands bend back 0.6 eV, which seems to indicate that the barrier formation mechanism can be explained by a combination of the MIGS and unified defect models.

iv. Ag-nGaN contacts were formed in UHV after two cycles of Ga reflux cleaning and characterised by I-V measurements. The best diode yielded a barrier height of 0.80 eV for an ideality factor of 1.56. These results are in good agreement with the band bending measured by SXPS and very similar to those reported by Kampen and Mönch[50] for their Ag contacts formed on atomically clean nGaN.

Chapter 6: Au-nGaN contact formation

6.1 Introduction

Gold is one of the most important metal in semiconductor device fabrication because of its excellent electrical conductivity and its resistance to oxidation. Additionally, its high work function (5.2 eV) means gold is an ideal choice for Schottky rectifiers on nGaN and Ohmic contact to pGaN. We have seen in Chapter 2 that gold contact formation has been widely investigated by current-voltage and capacitance measurement techniques. These works report that gold does indeed form rectifying contacts on nGaN with measured barrier heights ranging from 0.80 eV to 1.1 eV. This wide range of values is thought to be a consequence of different growth techniques and parameters, surface polarity and/or surface treatment.

Koyama *et al.*[46] recently reported the influence of pre-deposition surface treatment on the electrical characteristics of Au contacts on nGaN. They found that diodes formed after cleaning in organic solvents exhibited high leakage currents and

poor ideality factors, while those formed after an HF/HCl treatment were nearly Ohmic. On the other hand, contacts thermally deposited after cleaning in a warm NH_4OH solution or electro-deposited exhibited near ideal electrical behaviour. This study, as well as the wide range of values reported for Au-nGaN Schottky barrier heights, highlight the relevance of a systematic investigation of the influence of pre-deposition surface treatment.

Furthermore, only two groups[57,59] have reported XPS studies of Au deposition on atomically clean nGaN, and while the XPS measured barrier heights are similar in both cases, the mechanisms by which this barrier is reached differ widely. Wu *et al.* found that their 1.2 eV barrier was due to an initial upward band bending at the bare GaN surface of +0.7 eV and to a further +0.5 eV, as a result of Au induced band bending. Sporken *et al.* reported a bare surface band bending of +2.2 eV and a –1.05 eV downward band bending following Au deposition.

The divergence between the two experiments clearly calls for further XPS investigations in order to clarify the Au-nGaN contact formation mechanisms. Furthermore, the effect of surface preparation prior to metallisation has not yet been investigated by XPS. In this chapter, we compare the XPS results and I-V characterisations of Au contacts deposited on nGaN after three different surface treatments: *ex-situ* chemical cleaning in HF solution, *in-situ* annealing at 600°C for 10 minutes, and *in-situ* cleaning by the Ga reflux technique.

6.2 Experimental details

The samples used in all three experiments were cut from the same GaN epilayer. The 1.1 μm thick GaN layer was grown by MOVPE on sapphire along the c-axis. Hall measurements yielded a carrier concentration of 2×10^{15} cm^{-3} and a mobility of 41 $cm^2V^{-1}s^{-1}$ at room temperature. The experimental procedure was as follows:

- ***Ex-situ* surface treatment**

Prior to loading in UHV, all three samples were degreased in acetone and dipped in HF:DI H_2O (1:10) for 1 minute. Two strips of Au were evaporated on the edge of the sample using a conventional Edwards evaporator (base pressure of 10^{-6} mbar) in order to prevent charging during the XPS experiments. Figure 6-1 shows that these contacts clearly exhibit Ohmic-like behaviour.

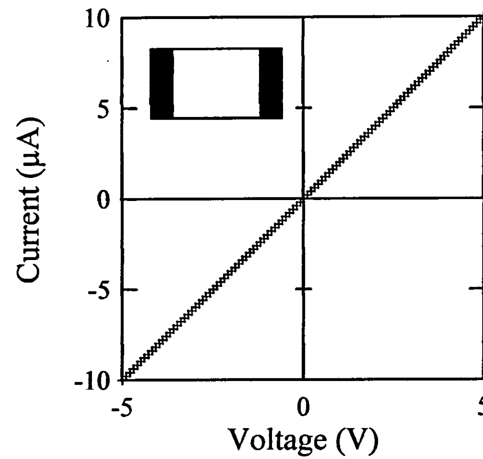

Figure 6-1: current-voltage characteristic of two large area Au contacts deposited on both edges of the GaN sample, as shown by inset diagram.

- ***In-situ* surface treatment**

After loading in UHV, two of the three samples underwent an additional *in-situ* surface treatment: the first sample was annealed at 600°C for 10 minutes while the second sample was subjected to two cycles of Ga reflux cleaning. The third sample was used for the control experiment. The sample temperature was monitored with an optical pyrometer.

- **Au deposition**

Au was deposited in steps of increasing thickness from sub-monolayer coverage to several monolayers, as shown on Table 6-1. The thickness was measured by a quartz crystal monitor (see section 4.7). XPS scans of the Ga *3d*, Ga $2p_{3/2}$, N *1s*, and Au *4f* core levels and the valence band were recorded at normal emission and 60° off normal emission before and after every deposition. A thick layer of Au was deposited at the end of the experiment to facilitate the processing of the samples into circular diodes for I-V characterisation.

Incremental deposition thickness (Å)	0.5	0.5	1	2	3	5	8	15	20	1500
Total coverage (Å)	0.5	1	2	4	7	12	20	35	55	2000

Table 6-1: sequence of Au depositions.

- **Diode processing**

The Au-GaN samples were patterned by conventional lithography with circular dots of diameters of 0.17 µm, 0.22 µm, 0.44 µm, 0.64 µm and 0.84 µm. A KI:DI H_2O solution was used to etch the Au and expose the underlying GaN surface. The Ohmic contact was provided by a large area Au contact left on the sample during lithography (see Figure 6-1).

6.3 Deposition on *in-situ* annealed surface

6.3.1 Core level intensity

The core level attenuation plots for the Ga *3d*, $2p_{3/2}$ and N *1s* core levels are displayed on Figure 6-2. As expected, the intensity drop with Au coverage is sharper at 60° off normal emission because of the shorter photoelectron escape depth. Similarly, the Ga $2p_{3/2}$ core level intensity drops faster than the Ga *3d* or N *1s* because of the difference in photoelectron kinetic energy, which makes the Ga $2p_{3/2}$ core level more surface sensitive.

The escape depth, or photoelectron mean free path λ can be calculated from the atomic mass A of the element, the bulk material density ρ, the Avogadro number N and the photoelectron kinetic energy E_{Kin} with the following equation[117]:

$$\lambda(nm) = 0.41\left[\frac{A(gmol^{-1})10^{24}}{\rho(kgm^{-3})N(mol^{-1})}\cdot E_{Kin}(eV)\right]^{\frac{1}{2}}$$

[6-1]

Both graphs of Figure 6-2 clearly shows two different attenuation regimes: below 5 Å Au coverage the intensity falls rapidly while above 10 Å, the drop is less steep. This behaviour is indicative of layer by layer growth followed by islanding, also called the Stranski-Krastanov mode. Layer by layer (or 2D) growth leads to exponential decay of the XPS core levels intensity I, from the substrate as the metal overlayer thickness z increases:

$$I \propto \exp\left(-\frac{z}{\lambda}\right)$$

[6-2]

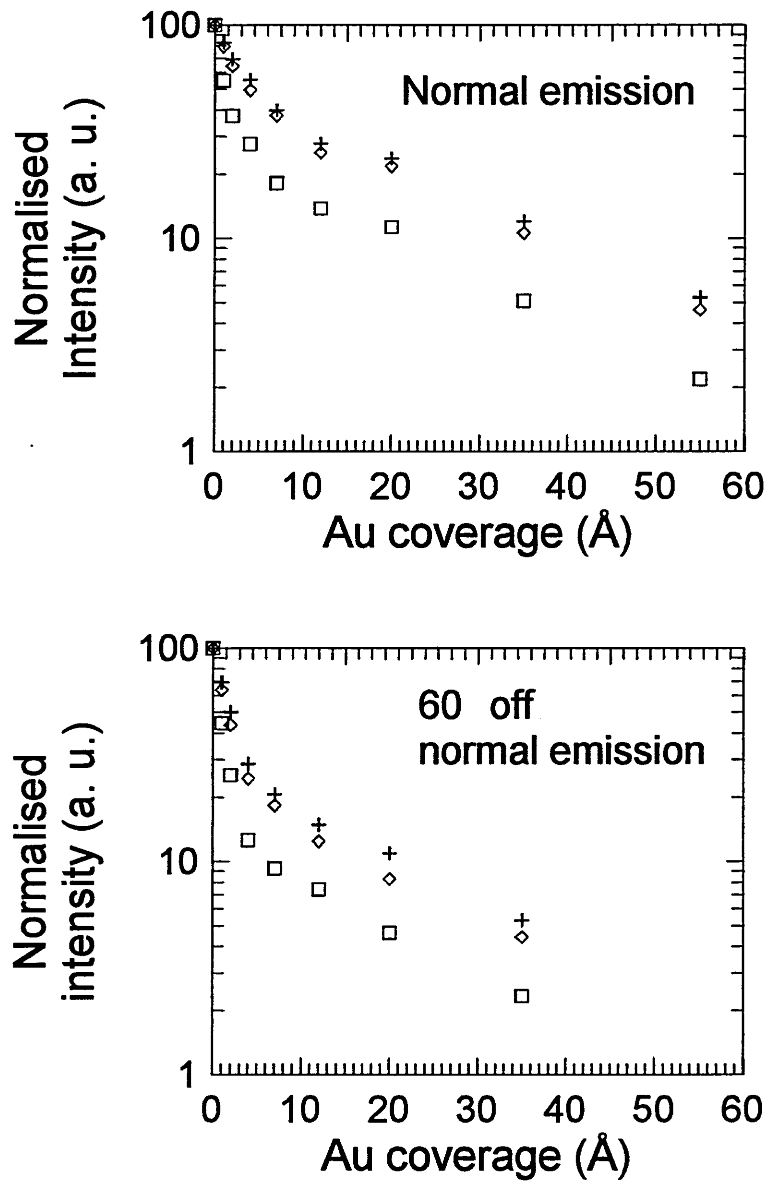

Figure 6-2: Ga *3d* (crosses), N *1s* (diamond shapes) and Ga $2p_{3/2}$ (squares) integrated core level intensity as a function of Au coverage at normal emission and 60° off normal emission. The data points are normalised to the same intensity at 0 Å Au coverage.

where λ is the attenuation length, which is equal to the photoelectron mean free path. Similarly, the Au core level intensity is expected to increase exponentially:

$$I \propto 1 - \exp\left(-\frac{z}{\lambda}\right)$$

[6-3]

Fitting equations [6-2] and [6-3] to the experimental data points from the initial stages of Au deposition therefore yields an experimental estimate of the mean free path calculated with equation [6-1]. Figure 6-3 shows an example of this fitting procedure for the Ga *3d* core level and Table 6-2 gives the results of the experimental fits compared to the calculated values. The experimental attenuation length is roughly four times smaller than the theoretical value, but the dependence of the attenuation length on kinetic energy and angle of emission is consistent with theory:

(i) The attenuation length at normal emission value is twice that of the 60° off normal emission case for the Ga *3d*, N *1s* and Au *4f* core levels. The fact that the Ga $2p_{3/2}$ mean free path at normal emission is not double that of the 60° off normal emission value is probably a consequence of the very small values involved.

(ii) $\lambda_{Ga3d} > \lambda_{N1s} > \lambda_{Ga2p}$, as predicted by equation [6-1].

It is therefore likely that the quartz crystal monitor consistently underestimated the Au thickness. This might be a consequence of the design of the manipulator, which shields part of the crystal area from the Au flux, and the source to sample geometry. Additionally, the thickness measured relies on the calibration of the crystal and assumes a sticking coefficient of 1.

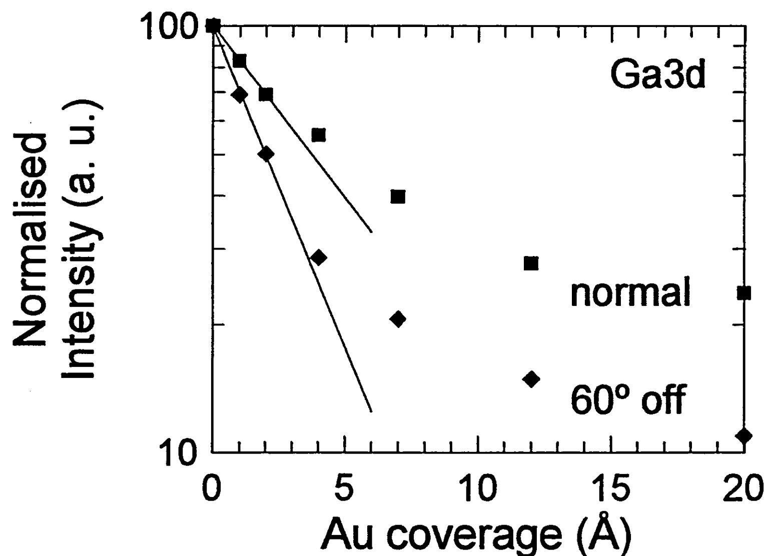

Figure 6-3: integrated intensity of the Ga *3d* core level at normal emission and 60° off normal emission as a function of Au coverage. Lines are least square fits to data points in region 0-2 Å.

	Calculated value (Å)		Experimental value (Å)	
	Normal emission	60° off	Normal emission	60° off
Au *4f*	18	9	7.4	3.6
Ga *3d*	19	9.5	5.4	2.6
N *1s*	16	8	4.3	2.4
Ga $2p_{3/2}$	6	3	2	1.5

Table 6-2: comparison between calculated values and measured values of the photoelectron mean free path for the GaN and Au core levels at normal and 60° off normal emission.

6.3.2 Core level binding energy

Figure 6-4 and Figure 6-5 present the variation of the Ga *3d* and N *1s* core levels with Au coverage. The peaks have been normalised to the same intensity after removal of a linear background. Curve fitting the experimental lineshapes indicated that the GaN core level peakshapes remain unchanged by Au deposition. The binding energy position of the peak centroïds of the two core levels behave in the same way:

(i) All core level are shifted 0.35 eV towards lower binding energy after annealing at 600°C compared to the HF etched surface.

(ii) The first Au deposition, of 1 Å according to the quartz crystal monitor, caused a further 0.25 eV shift in the same direction.

(iii) Subsequent Au depositions did not induce any more variations.

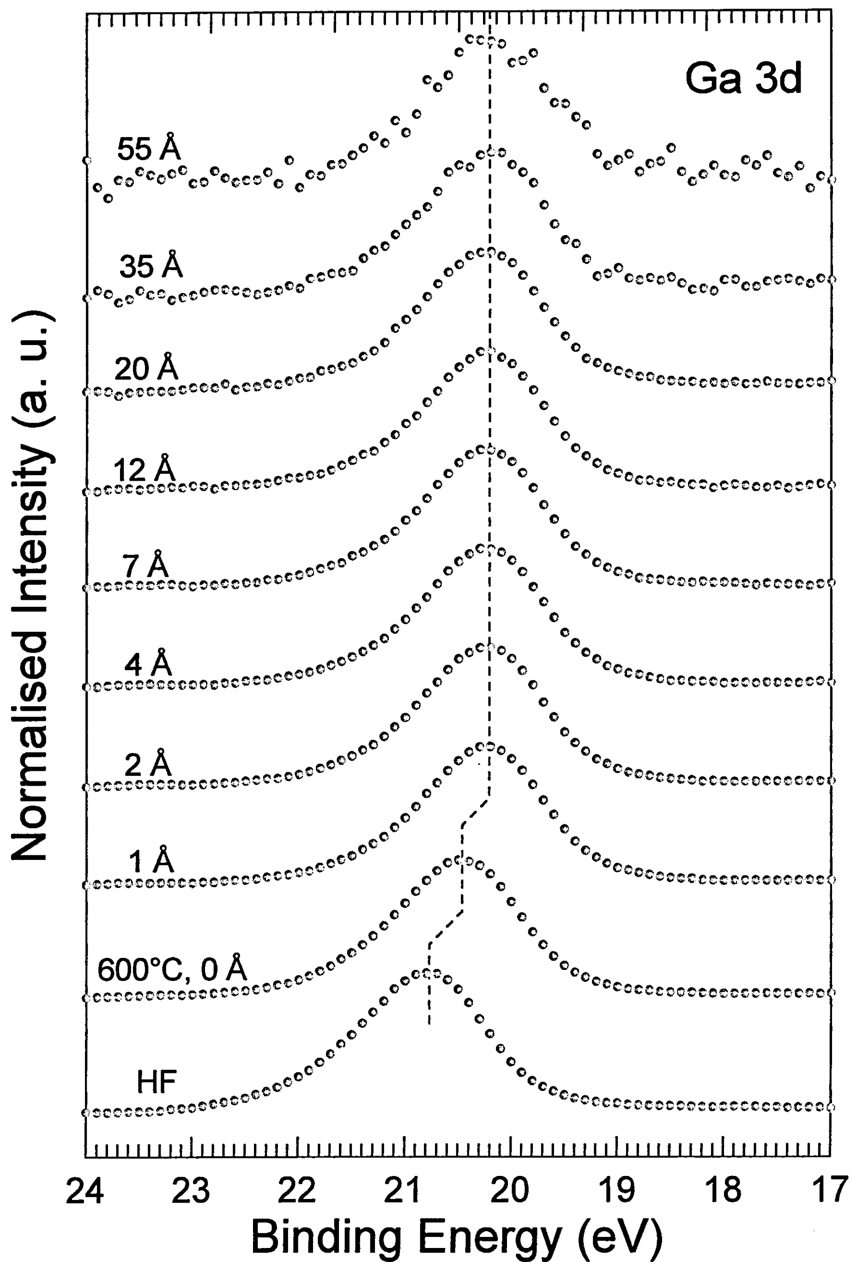

Figure 6-4: evolution of the Ga *3d* core level peakshape with Au coverage at normal emission.

The absence of chemical changes combined with the fact that the GaN core levels all behave in the same way, indicates that the binding energy shifts correspond to a total upward band bending at the surface of 0.6 eV, mainly due to annealing (0.35 eV) and to the first Au deposition (0.25 eV). As seen in Chapter 5, partial desorption of surface contaminants and the native oxide by the anneal might account for the initial 0.35 eV energy shift, since cleaning of nGaN surfaces has been shown to induce significant upward band bending[52,53,118].

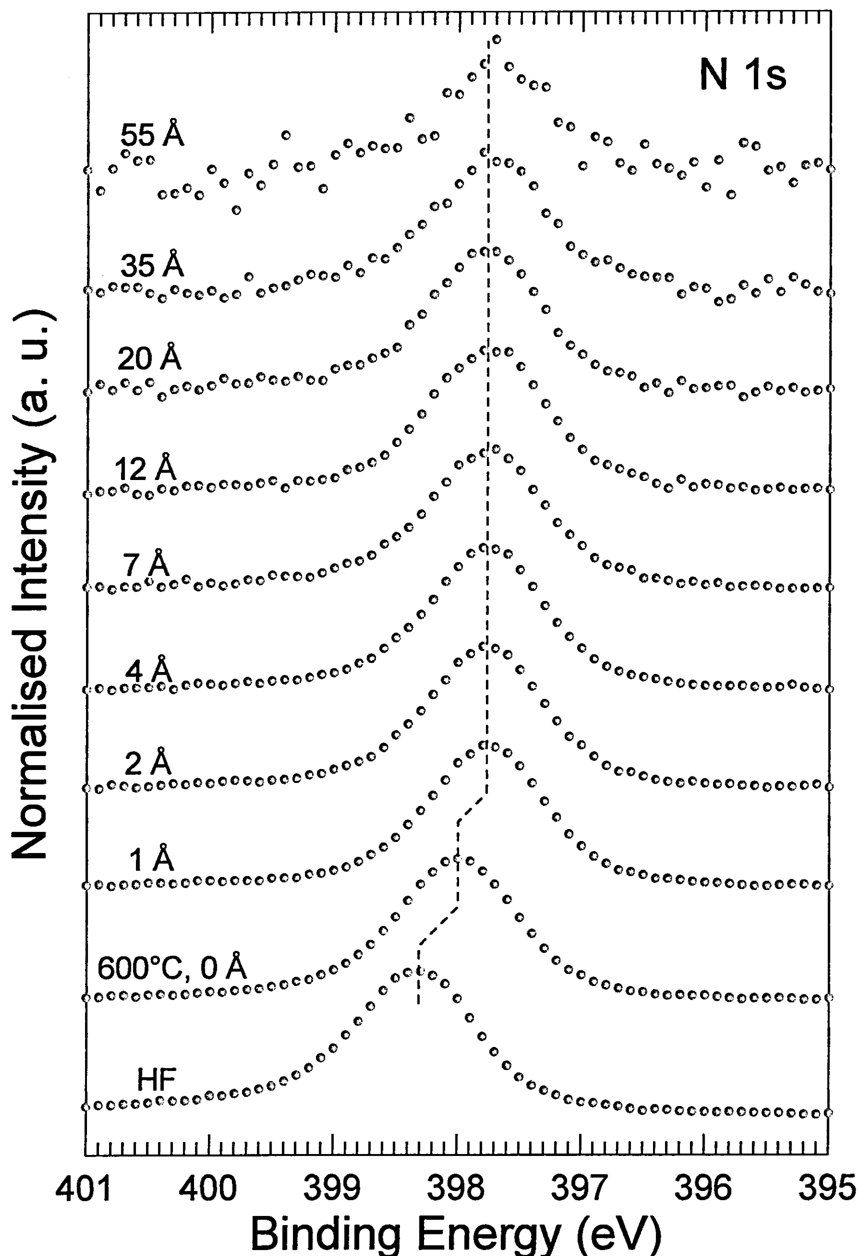

Figure 6-5: evolution of the N *1s* core level peakshape with Au coverage at normal emission

The Au $4f_{7/2}$ binding energy also changes with increasing Au thickness, from 84.3 eV at 1 Å to 84 eV at 55 Å, as shown on Figure 6-6. 84 eV is the binding energy of clean, metallic Au, used to calibrate the instrument before the experiment. Since the Au peak is significantly broader at low coverage, the shift is likely to be related to changes in the chemical state of Au. This has been observed before by Sporken *et al*[57], who linked this broadening to a high binding energy additional component attributed to

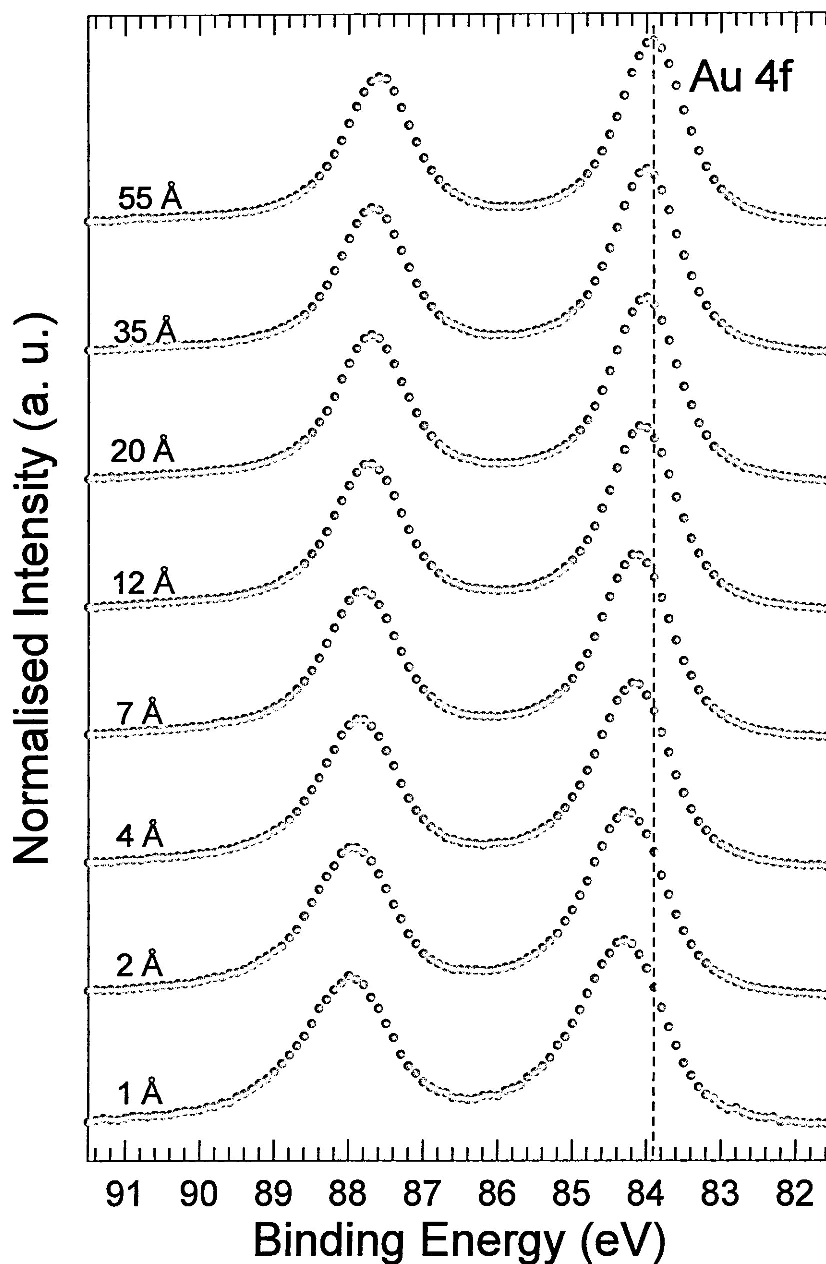

Figure 6-6: evolution of the Au *4f* core level peakshape with Au coverage.

Ga-Au bonding. They reported that this component probably corresponded to only one atomic plane, indicating an abrupt interface.

The Au $4f_{7/2}$ core level binding energies of Ga-Au alloys have been measured using XPS by Jayne *et al.*[119] and are given in Table 6-3. Crucially, they found that the Ga *3d* binding energy shifted less than 0.3 eV over the whole range of alloy compositions whilst the Au $4f_{7/2}$ binding energy spanned over 1.5 eV. This could explain why no chemical shift was observed on the Ga 3d scans while the Au $4f_{7/2}$ core

level shifted 0.3 eV as the Au coverage increases. The interface is therefore likely to consist of a thin Au-Ga alloy layer, which is rapidly buried under pure Au.

Au-Ga alloy	Binding energy (eV)
$AuGa_2$	85.5
AuGa	85.2
γ Au_9Ga_4	84.9
β $Au_{0.78}Ga_{0.22}$	84.6
α $Au_{0.88}Ga_{0.12}$	84.4
Pure Au	83.95

Table 6-3: binding energies of Au $4f_{7/2}$ core level emission from five Au-Ga alloys (ref. 119)

6.3.3 I-V results

Current-voltage measurements of some of the diodes fabricated on the 600°C annealed sample are presented on Figure 6-7. The contacts clearly exhibit strong rectifying behaviour. The reverse current was below the detection limit of the pico-ammeter (10^{-12} A) up to a reverse bias of -6 V.

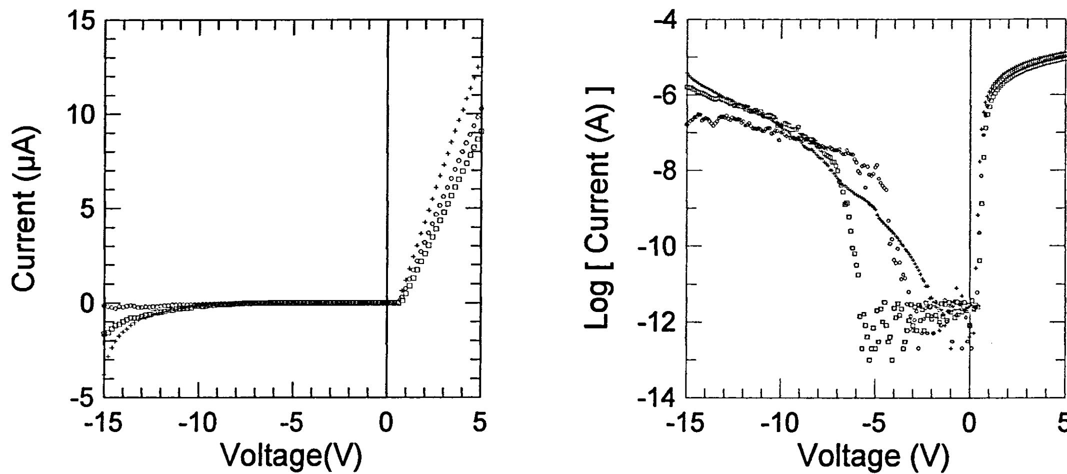

Figure 6-7: linear (left hand side) and semi-log I-V characteristics of three of the diodes measured.

The ideality factors and barrier heights were extracted by fitting equation [3-35] to the linear region of the forward current characteristic as shown on Figure 6-8. The theoretical value[37] of the Richardson constant for GaN of 26 $Acm^{-2}K^{-2}$ was used.

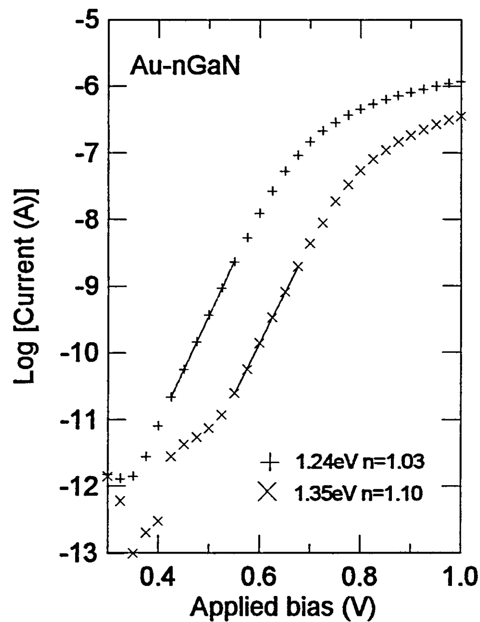

Figure 6-8: forward bias characteristics of two diodes, showing the linear region used to extract the Schottky parameters.

The Schottky parameters (ϕ_{bo} and n) are given in Figure 6-9 and summarised in Table 6-4, where "best" and "highest" refer respectively to the diode with the lowest ideality factor and highest barrier height. The very low ideality factors indicate that most of the current flow across the barrier is governed by thermionic emission, with minimal contributions from tunnelling and generation-recombination processes. It also ensures the validity of the barrier height extraction method[8]. The small standard deviations in ϕ_{bo} and n values are indicative of high contact uniformity. Indeed, only 5 out of the 41 measured diodes yielded an ideality factor above 1.2 (these diodes are not included in the statistics presented in Table 6-4). The mean and highest values for the zero-bias barrier height are 1.24 eV and 1.35 eV, respectively and are the highest reported to date for Au-nGaN contacts. As seen in section 2.1.3, values from the literature for barrier heights of practical Au-nGaN contacts range from 0.84 eV to 1.1 eV, as measured by I-V. In these studies, the GaN samples were subjected to various surface treatments such as boiling in *aqua regia*[37,48], $HCl:H_20$[44,120], $HF:H_20$[121] and $KOH:H_20$ dips[42], and oxygen plasma asher cleaning[44]. In each case, the substrates were then exposed to air prior to metallisation at room temperature. He *et al.*[120] reported a typical barrier height and best barrier height of respectively 1.08 eV and 1.22 eV for their Au contacts deposited at 77K.

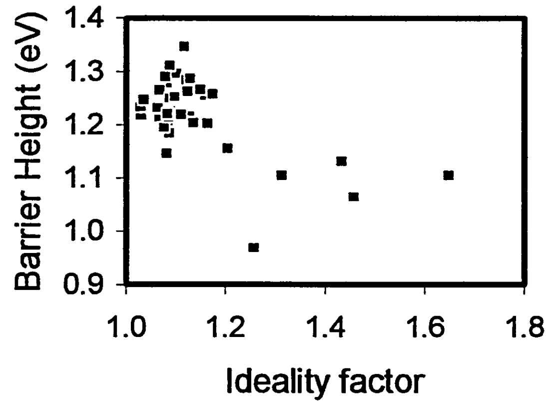

Figure 6-9: distribution of the barrier heights plotted versus the ideality factor, for 41 diodes.

	Mean	Standard deviation	Best[a)]	Highest[b)]
ϕ_{b0}(eV)	1.24	0.041	1.24	1.35
n	1.10	0.040	1.03	1.10

[a)] refers to the diode with the lowest ideality factor
[b)] refers to the diode with the highest barrier

Table 6-4: Schottky parameters of Au/nGaN contacts

As the I-V curves displayed a high series resistance, the experimental data were also analysed using the Norde and small signal conductance methods described in section 3.3.1 and 3.3.2. An example of the Norde method is given in Figure 6-10, where the coordinates of the minimum { $V_0, F(V_0)$ } yield the barrier height from equation [3-38] and the corresponding I_0 yields the series resistance from equation [3-39]. The series resistance extracted using this method range from 135 kΩ to 930 kΩ. The barrier heights proved to be somewhat larger than those extracted using the conventional method. Figure 6-11 plots the difference between barrier heights extracted from the two methods as a function of the ideality factor. The plot shows that as the diodes become less ideal, the difference between the two methods gets wider. A linear fit of the data points nearly passes through the origin, indicating that the two methods would yield identical values for the barrier height at n=1. This behaviour is probably due to the fact that the Norde method has been derived assuming a unity ideality factor, so that it is

quite normal that the barrier height difference widens as n>1. This, however, reinforces the validity of the conventional extraction method.

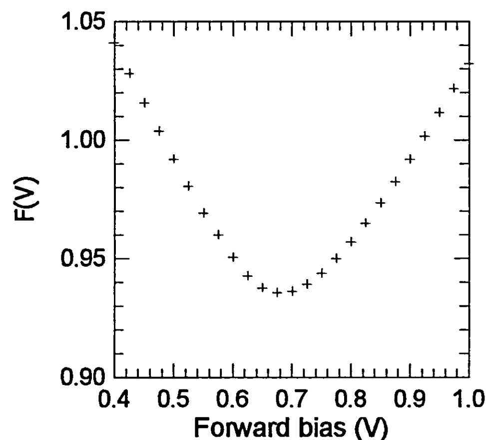

Figure 6-10: example of the application of the Norde plot. The coordinates of the plot minimum yield barrier height and series resistance.

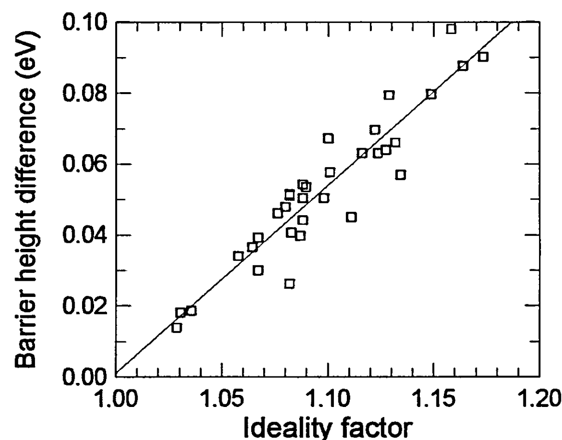

Figure 6-11: barrier height determined with the Norde plot minus conventionally determined barrier height plotted as a function of the ideality factor (also extracted using the conventional method). The solid line is a least-square fit to the data points.

An example of the small signal conductance method is presented in Figure 6-12 (a), where the ideality factor and series resistance are extracted from the linear fit of the I/G versus I plot. The series resistance thus obtained is then used to correct the voltage axis so that the voltage drop caused by the series resistance is removed. The experimental data points are then re-plotted using this corrected voltage scale on Figure 6-12 (b). The corrected curve is therefore free of series resistance effects and can be

fitted with equation [3-35] over the whole voltage range, instead of only a few data points. For the diode used in this example, the conductance plot on the left hand side yields an ideality factor of 1.074 and a series resistance of 359 kΩ, while the fit of the corrected $I(V\text{-}IR_S)$ curve yields an ideality factor of 1.082. This good agreement between the two methods was verified for most of the diodes under investigation. The series resistances extracted with the conductance method range from 185 kΩ to 575 kΩ.

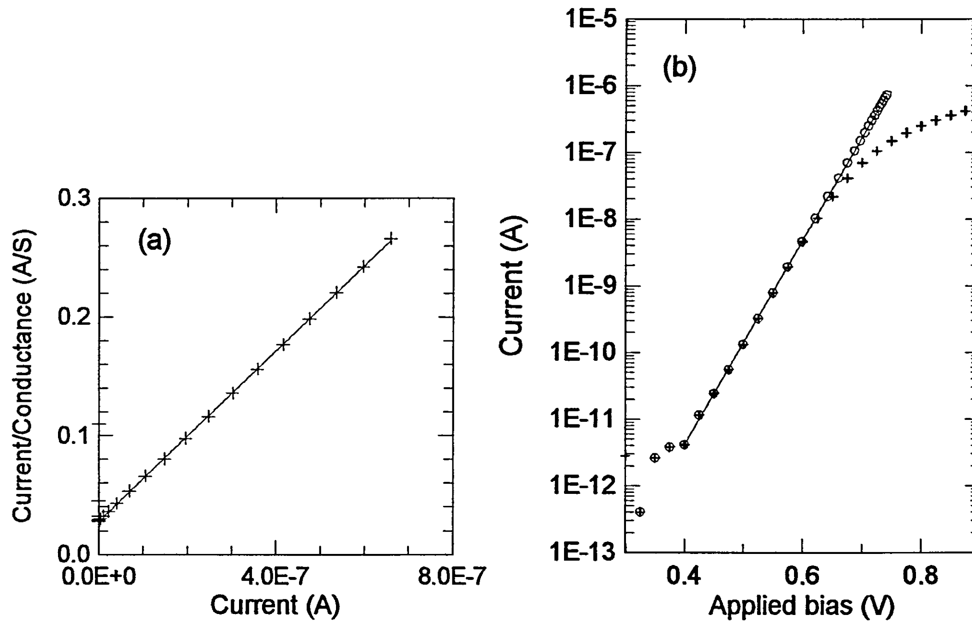

Figure 6-12: (a) application of the small signal conductance method. The y-axis intercept and slope of the linear fit respectively yield the ideality factor and series resistance. (b) experimental *I(V)* curve (+) and corrected *I(V-IR_S)* curve (o).

6.4 Deposition on *in-situ* Ga reflux cleaned surface

6.4.1 Core level intensity

The core level attenuation plots are presented in Figure 6-13.

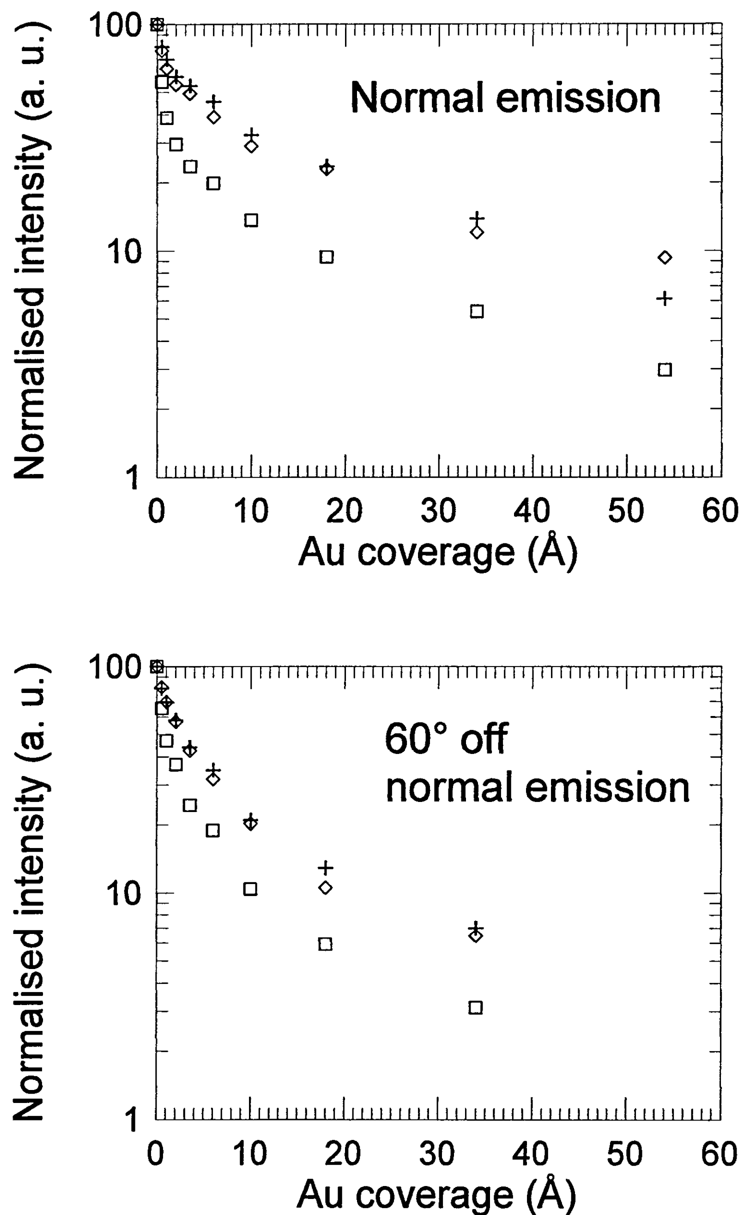

Figure 6-13: Ga *3d* (crosses), N *1s* (diamond shapes) and Ga $2p_{3/2}$ (squares) integrated core level intensity as a function of Au coverage at normal emission and 60° off normal emission. The data points are normalised to the same value at 0 Å Au coverage.

As for the 600°C annealed surface, the Ga $2p_{3/2}$ core level intensity drops faster with Au coverage than the Ga *3d* and N *1s* core levels and the intensities on the 60° off normal emission plot are smaller than the normal emission plot at high Au coverage (z >10 Å). The plots also seem to exhibit two regions indicative of layer by layer growth followed by clustering. Assuming a Stransky-Krastanov mode of growth, the data points from the initial stages of Au deposition were fitted in the same manner as described in section 6.3.1 and the resulting fit for the Ga *3d* core level is shown on Figure 6-14. In contrast to the 600°C annealed surface (Figure 6-3), the slope of the normal emission fit is as steep as that of the 60° off normal emission fit instead of being half as steep. Photoelectron mean free paths extracted from all the core levels under investigation are given on Table 6-5. The Au *4f* core level is the only core level yielding larger attenuation length at normal emission than at 60° off normal emission but the expected 2:1 ratio is not demonstrated. The Ga *3d* core level yields similar values for the mean free path at both angles of emission while the N *1s* and Ga $2p_{3/2}$ mean free paths were marginally larger at 60° off normal emission.

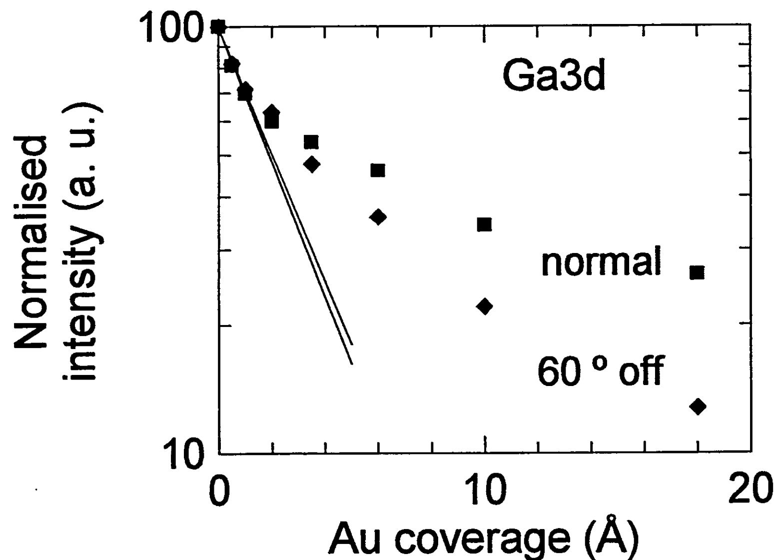

Figure 6-14: attenuation plot of the N *1s* core level 60° off normal emission and normal emission. The lines are least square fits of the data points in the region 0-2 Å.

The anomaly in the core level attenuation length seems to indicate that the Au-GaN interface is not abrupt, possibly as a result of chemical reactions or Au in-

diffusion. Another possibility is that the *in-situ* Ga reflux cleaning caused roughening of the GaN surface. Alternatively, the assumption of Stransky-Krastanov growth might not be justified, in which case Au growth would be purely three dimensional. The main point, however, is that attenuation plots for the Ga reflux cleaned surface display fundamental differences from the well behaved 600°C annealed surface.

	Calculated value (Å)		Experimental value (Å)	
	Normal emission	60° off	Normal emission	60° off
Au *4f*	18	9	6.2	4.6
Ga *3d*	19	9.5	2.8	2.8
N *1s*	16	8	2.2	2.8
Ga $2p_{3/2}$	6	3	1.1	1.3

Table 6-5: comparison between calculated values and measured values of the photoelectron mean free path for the GaN core levels at normal and 60° off normal emission.

6.4.2 Core level binding energy

The evolution of the binding energy spectra for all core levels is shown on Figure 6-15 (a) and Figure 6-16 (a). Once again, the peaks have been normalised to the same intensity after removal of a linear background.

The binding energy of the centroïd of the GaN core level peaks, extracted from the stack plots, are given as a function of Au coverage on Figure 6-15 (b) and Figure 6-16 (b). The shifts undergone by the two core levels are similar in trend and magnitude and since curve fitting showed no significant change in the shapes of the photoelectron peaks of the GaN core levels, it is likely that these shifts are rigid Fermi shifts.

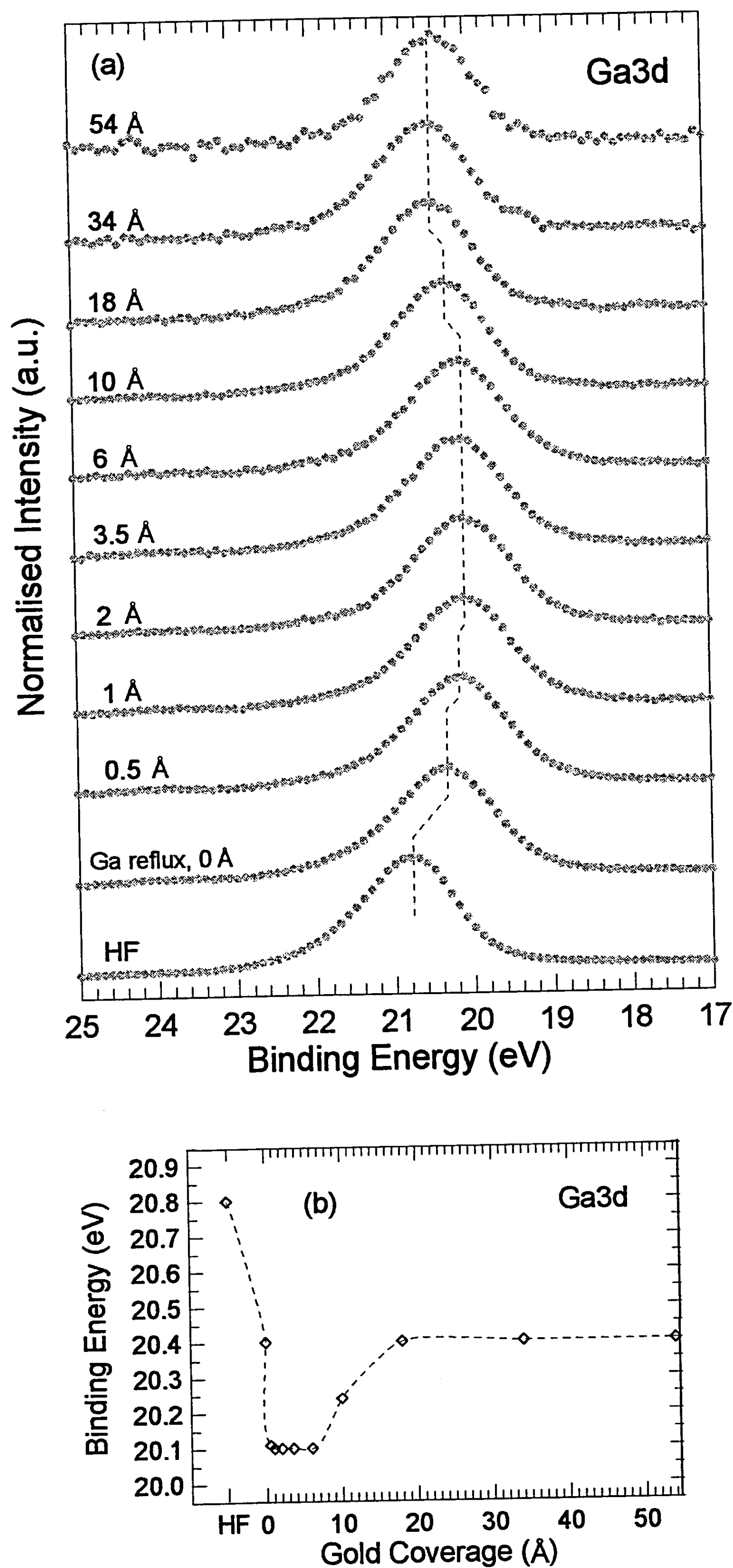

Figure 6-15: evolution of the (a) Ga *3d* core level peakshape and (b) binding energy of the peak centroïd with Au coverage at normal emission. Lines are intended to be a guide to the eye.

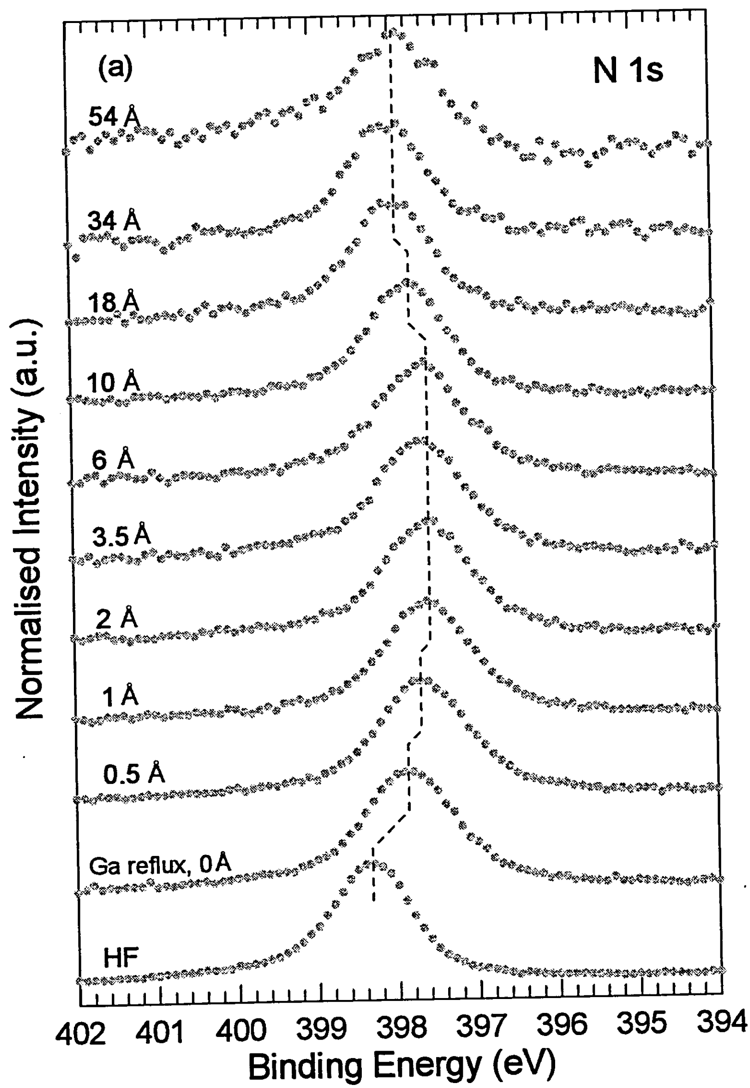

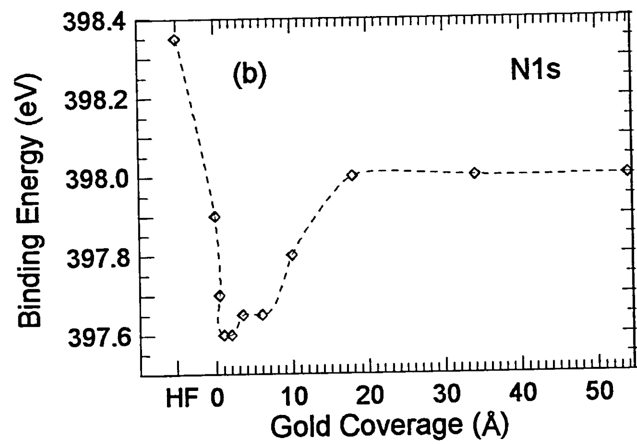

Figure 6-16: evolution of the (a) N *1s* core level peakshape and (b) binding energy of the peak centroïd with Au coverage at normal emission. Lines are intended to be a guide to the eye.

Cleaning of the GaN surface by the Ga reflux process induced a shift of about 0.45 eV to lower binding energy, as seen in section 5.4. The first two Au depositions (0.5 Å and 1 Å) induced a further shift of 0.3-0.4 eV in the same direction. The peaks then remain at the same binding energy up to 6 Å Au coverage. The next two depositions (10 Å and 18 Å) caused the peaks to shift back to high binding energy by 0.35 eV whilst the last two depositions did not induce any further shift. The binding energy of the GaN core levels after the last Au deposition is therefore back to its pre-deposition level. This behaviour is strikingly different from the 600°C annealed surface.

The Au *4f* core level binding energy variation (Figure 6-17) also presents strong differences when compared to the 600°C annealed surface. The binding energy position of the Au $4f_{7/2}$ peak is 84 eV after the first Au deposition instead of 84.3 eV for the 600°C annealed surface. The peak position then moves slightly to lower binding energy at low Au coverage (1 Å to 3.5 Å) and to higher binding energy at high Au coverage (10 Å to 34 Å) but is back to 84 eV after the last deposition (54 Å). The peak also becomes sharper with increasing Au coverage.

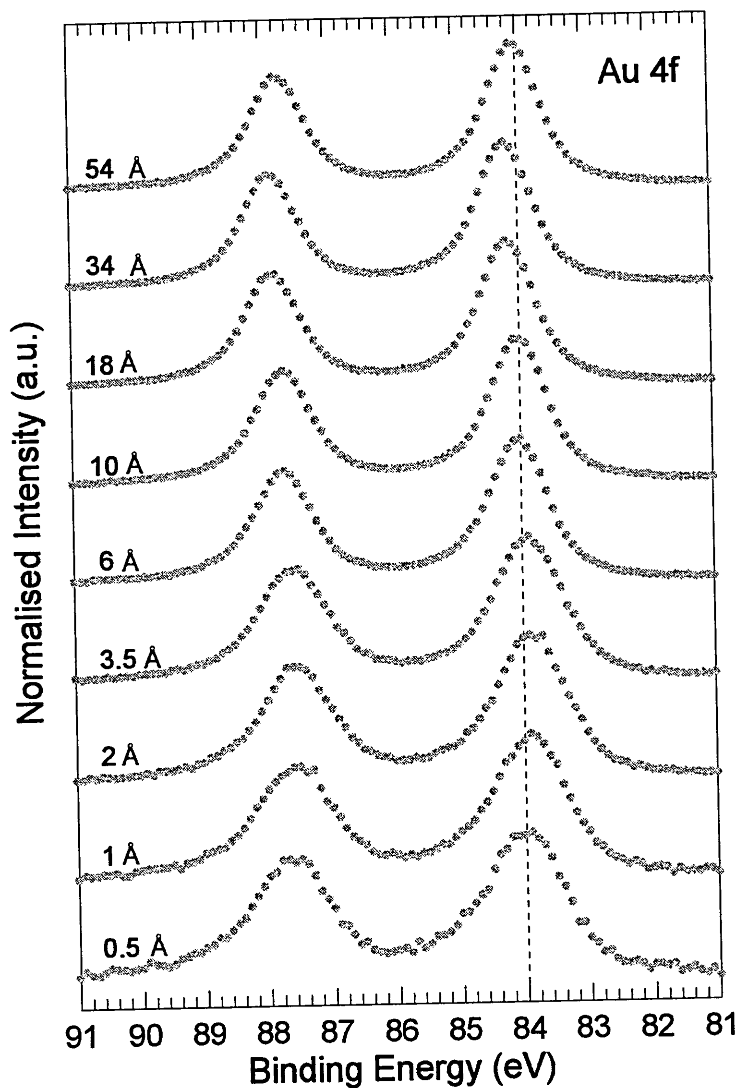

Figure 6-17: evolution of the Au *4f* core level peakshape with Au coverage at 60° off normal emission.

6.4.3 I-V results

Figure 6-18 gives the results of the current-voltage characterisation for a selection of the 35 diodes measured. The electrical behaviour ranges from Ohmic to rectifying. The rectifying contacts show different forward bias thresholds, indicating a wide range of Schottky barrier heights.

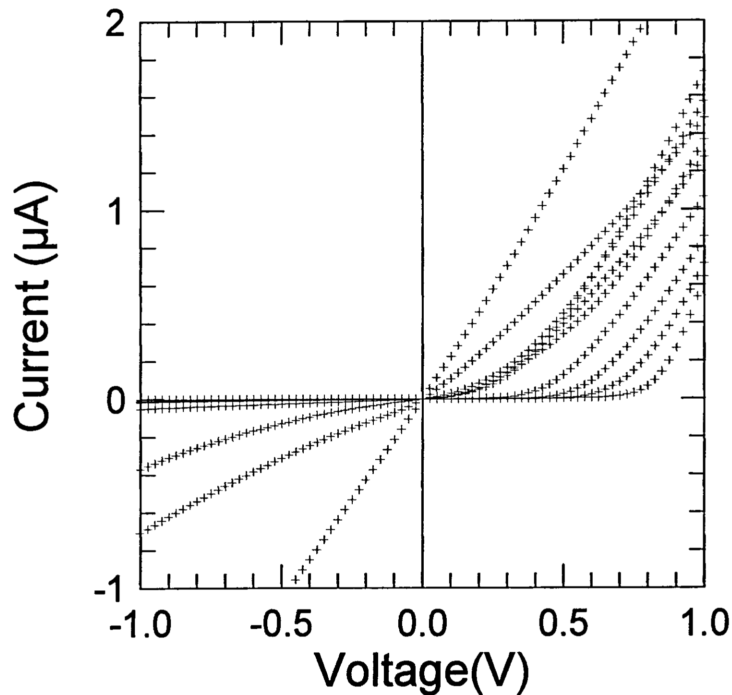

Figure 6-18: current voltage characteristics of a selection of Au-GaN circular contacts formed after 2 cycles of Ga reflux cleaning.

The barrier heights and ideality factors were extracted from current voltage characteristics using the conventional method for the 15 diodes with a linear region long enough to permit fitting (2 orders of magnitude). Figure 6-19 (a) shows the *I(V)* semi-log plot of the diode with the lowest ideality factor of 1.18 and a barrier height of 0.89 eV. Despite this low ideality factor, the diode exhibits a large leakage current at reverse bias. At first glance, this may appear to be due to a strong tunnelling component. However, Figure 6-19 (b) shows the influence of white light illumination while recording the current voltage characteristics. The reverse current of the measurement under illumination at low reverse bias is an order of magnitude higher than that of the measurement in the dark. The forward current is also higher in the illuminated case. The ideality factors for the illuminated and dark measurements were 1.66 and 1.61, for a barrier height of 0.87 eV and 0.88 eV, respectively. This behaviour could be explained by light-enhanced surface generation-recombination current contributions even though the GaN layer should be transparent to white light because of its 3.4 eV band gap. It is possible however that deep traps within the band gap could act as generation-recombination centres. The fact that the sample glowed white under X-ray illumination during the XPS experiment seems to confirm the presence of radiative recombination in the visible range of the electromagnetic spectra. Brillson *et al.*[122] detected the presence

of several deep states at native GaN surfaces using low-energy electron-excited nanoscale luminescence spectroscopy. They also found that new states are created after annealing at high temperature in UHV or after metal deposition. Additionally, Deep Level Transient Spectroscopy measurement of Au contacts[123] fabricated by thermal evaporation on MOVPE grown nGaN revealed two defects at energy levels at 0.27 eV and 0.61 eV below the conduction band minimum.

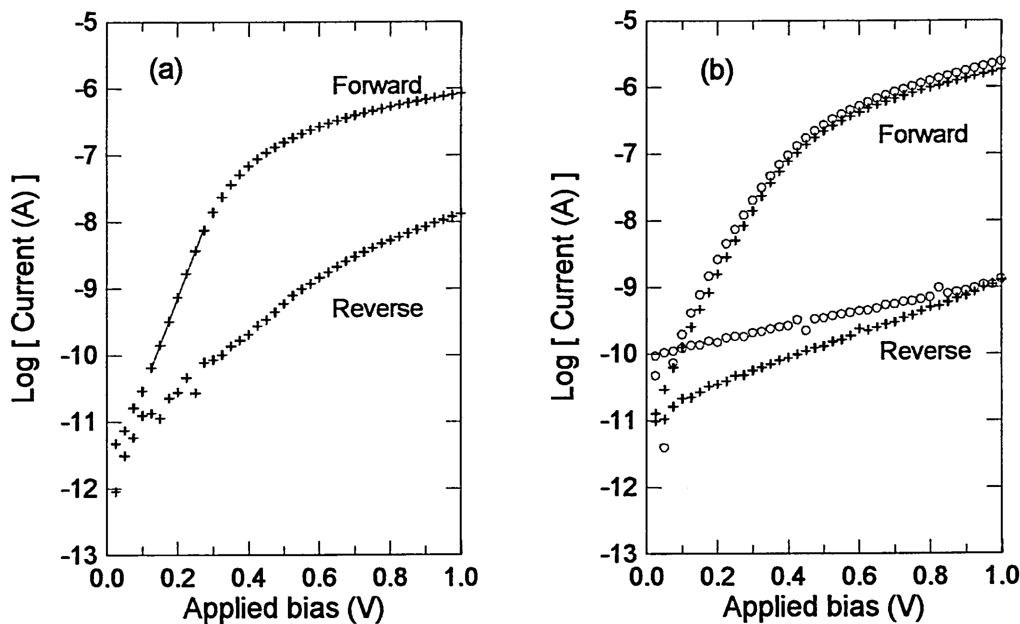

Figure 6-19: (a) semi-log plot of the current voltage characteristic of the diode with the lowest ideality factor of 1.18, and (b) dark (+) and illuminated (o) I-V characteristics of a 0.62 mm diameter diode.

The high series resistance combined with significant tunnelling and recombination current left only a few data points to determine the Schottky parameters by the conventional method and in some cases the linear region was entirely hidden. As seen in the previous section, different methods have been devised to analyse I-V data. The Norde method did not yield any physically relevant results for the diodes studied in this section, probably because of the high ideality factors.

The small signal conductance method was applicable to a number of diodes as shown on Figure 6-20 (a). In this case, the conventional method could not be used confidently because the linear region was hidden by recombination current contribution at low bias. The plot of the forward current divided by the conductance versus forward current can however, be fitted very well by a straight line, as predicted by the method.

The fit yielded a series resistance of 310 kΩ and an ideality factor of 2.10. The series resistance was used to correct the voltage axis and the $I(V\text{-}IR_S)$ curve is plotted alongside the $I(V)$ curve on Figure 6-20 (b). The slope of the corrected $I(V\text{-}IR_S)$ gave n=2.12, which is very close to the value of 2.10 from the fit of Figure 6-20 (a). The Schottky barrier height was found to be 0.80 eV.

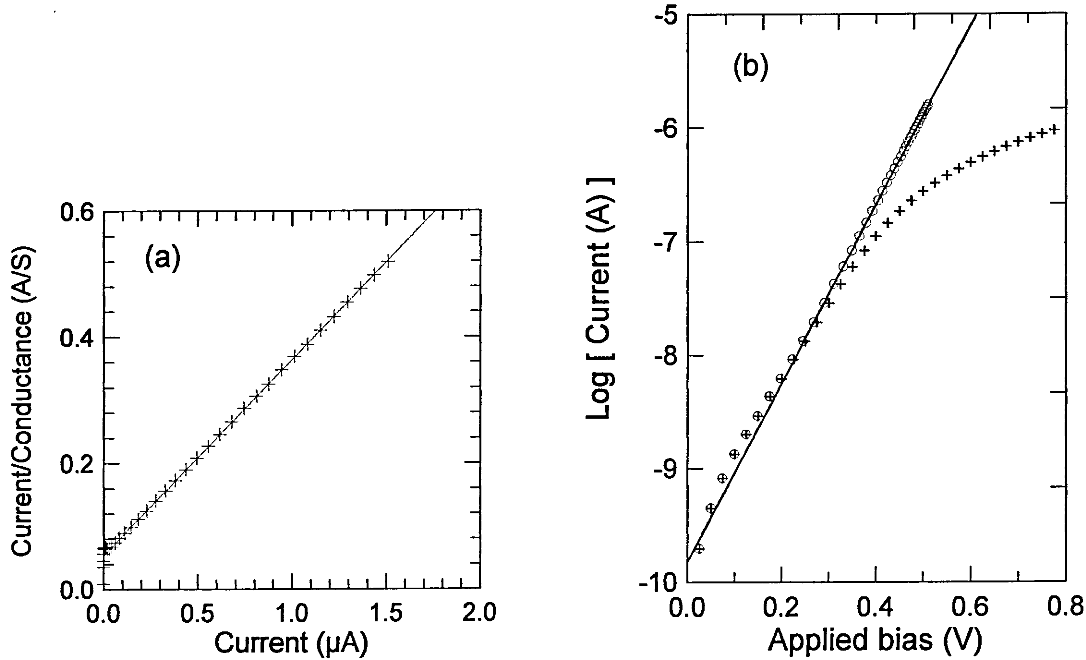

Figure 6-20: application of the small signal conductance method on a 0.17 mm diameter diode. (a) the slope and y-axis intercept of the linear fit yield series resistance and ideality factor. (b) experimental *I(V)* and corrected *I(V-IR_S)* curves.

The small signal method was however, not applicable to the diode for which the standard $I(V)$ curve yielded n=1.18 (Figure 6-20 (a)), because the I/G versus I plot was not linear. 13 diodes could be analysed using this method, yielding ideality factors and barrier heights ranging from 1.88 to 3.82 and 0.66 eV to 0.95 eV, respectively. The average barrier height was 0.78 eV. Results from the conventional method, extracted from 15 diodes, gave ideality factors and barrier heights ranging from 1.18 to 3.32, and 0.74 eV to 0.94 eV, respectively. The average barrier height was 0.84 eV.

Both methods yielded mean barrier heights that are 0.4-0.45 eV lower than the mean barrier height of the contacts formed on the 600°C annealed surface.

6.5 Deposition on chemically treated surface

6.5.1 Core level intensity

The normalised intensity of the N *1s* and Ga $2p_{3/2}$ core levels is plotted as a function of Au coverage on Figure 6-21. As before, the intensity drops sharply with the first few depositions, and then decreases less steeply. This pattern is indicative of layer by layer growth followed by clustering. The intensities fall more rapidly in the surface sensitive case.

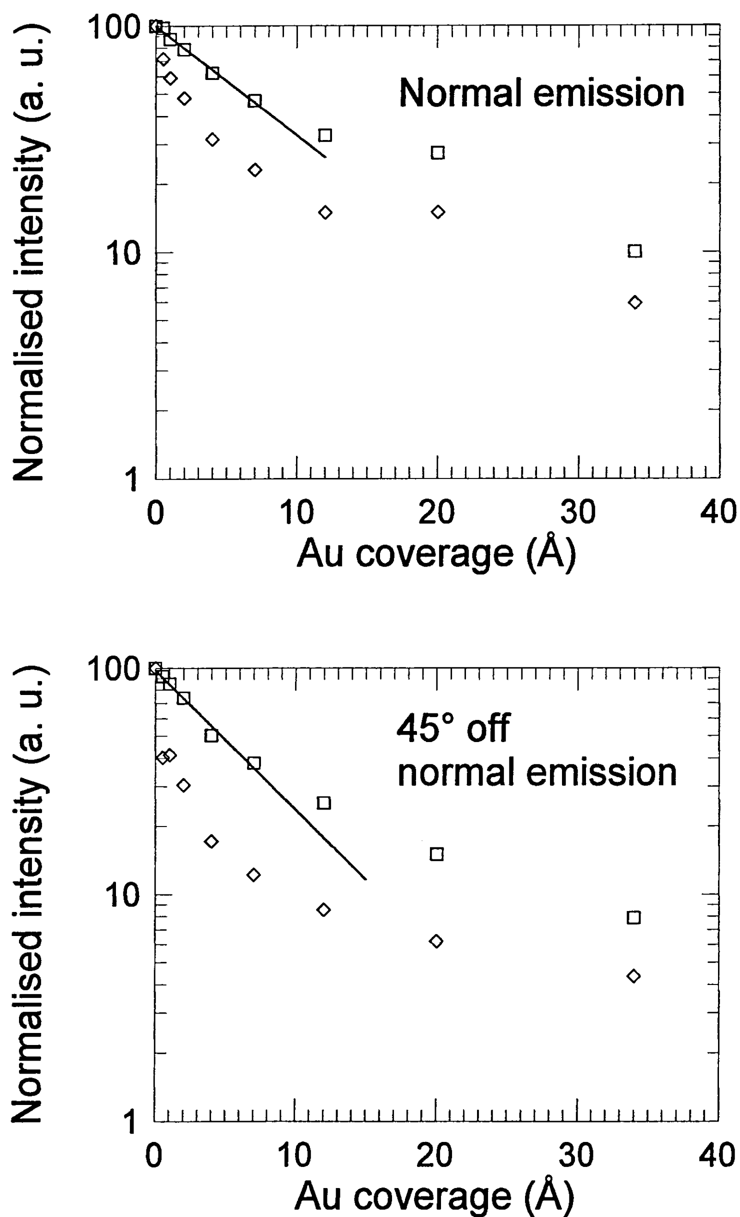

Figure 6-21: attenuation plots of the N *1s* (squares) and Ga $2p_{3/2}$ (diamond shapes) core levels at normal emission and 45° off normal emission. Lines are least-square fits to data points in the region 0-7 Å.

The initial drop of the core levels was fitted by an exponential curve in order to extract the attenuation lengths, given in Table 6-6. The exponential fit is in good agreement with the experimental data up to 7 Å Au coverage. The ratios of the experimentally determined attenuation lengths at 45° off normal emission and normal emission are close to the expected theoretical ratio of 1.41.

	Calculated value (Å)		Experimental value (Å)	
	Normal emission	45° off	Normal emission	45° off
Au *4f*	18	13	8.1	6
Ga *3d*	19	13.5	10	8
N *1s*	16	11	9.1	5.9

Table 6-6: theoretical and experimentally determined attenuation lengths for the GaN and Au core levels.

6.5.2 Core level binding energy

Figure 6-22 shows the variation of the Ga *3d* core level XPS peakshape with increasing Au coverage.

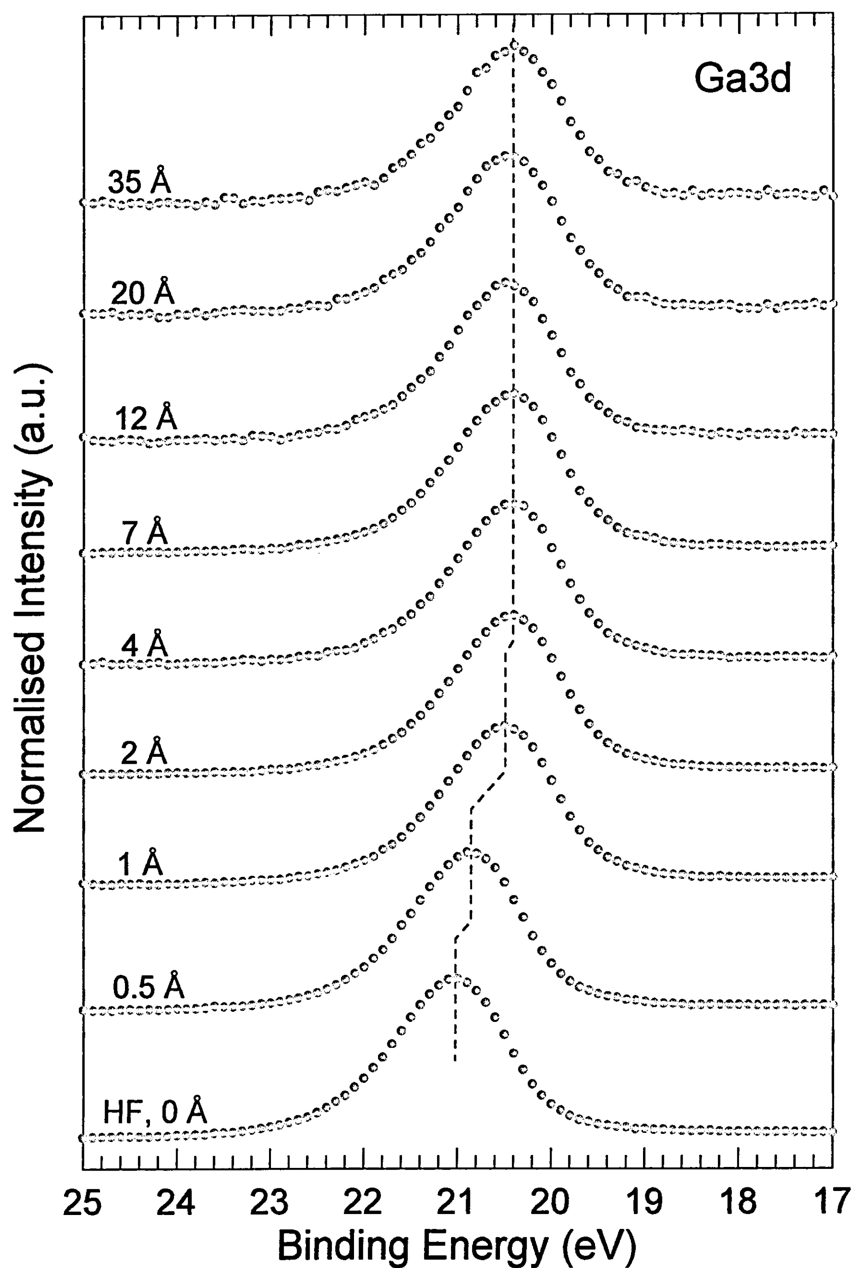

Figure 6-22: evolution of the Ga *3d* core level with Au coverage.

The Ga *3d* peak is shifted 0.15 eV to lower binding energy by the first Au deposition (0.5 Å). The second deposition (1 Å) and third deposition (2Å) induce further shifts of 0.35 eV and 0.1 eV, respectively. The Ga *3d* peak then remained at a fixed binding energy following subsequent Au depositions.

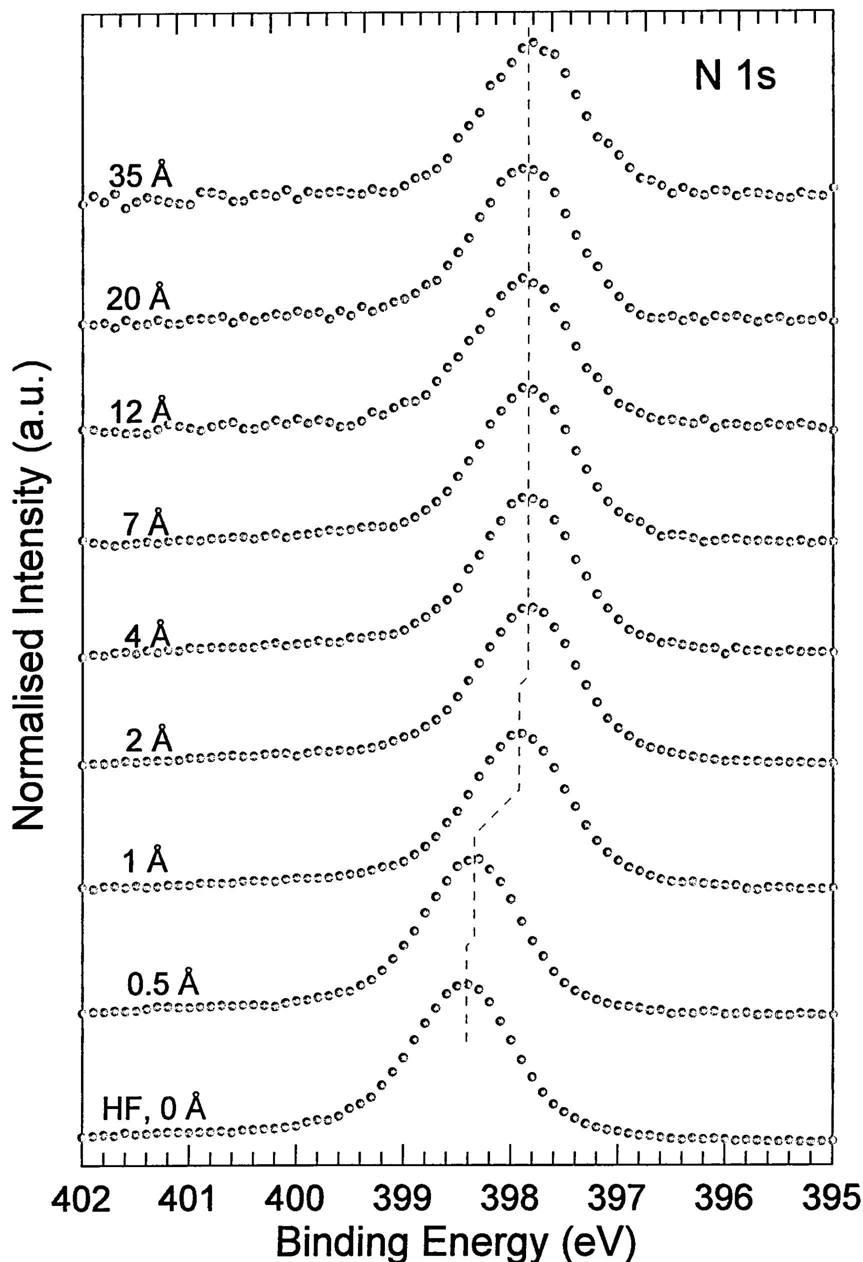

Figure 6-23: evolution of the N *1s* core level peakshape as a function of Au coverage.

Scans of the N *1s* core level, presented on Figure 6-23, display shifts similar to the Ga *3d* core level. Since curve fitting showed that there was no change in the shape of the peaks that could be related to chemical shift, it is likely that the observed shifts are Fermi shifts. Therefore, the total upward band bending induced by the Au deposition on the chemically treated surface is 0.6 eV.

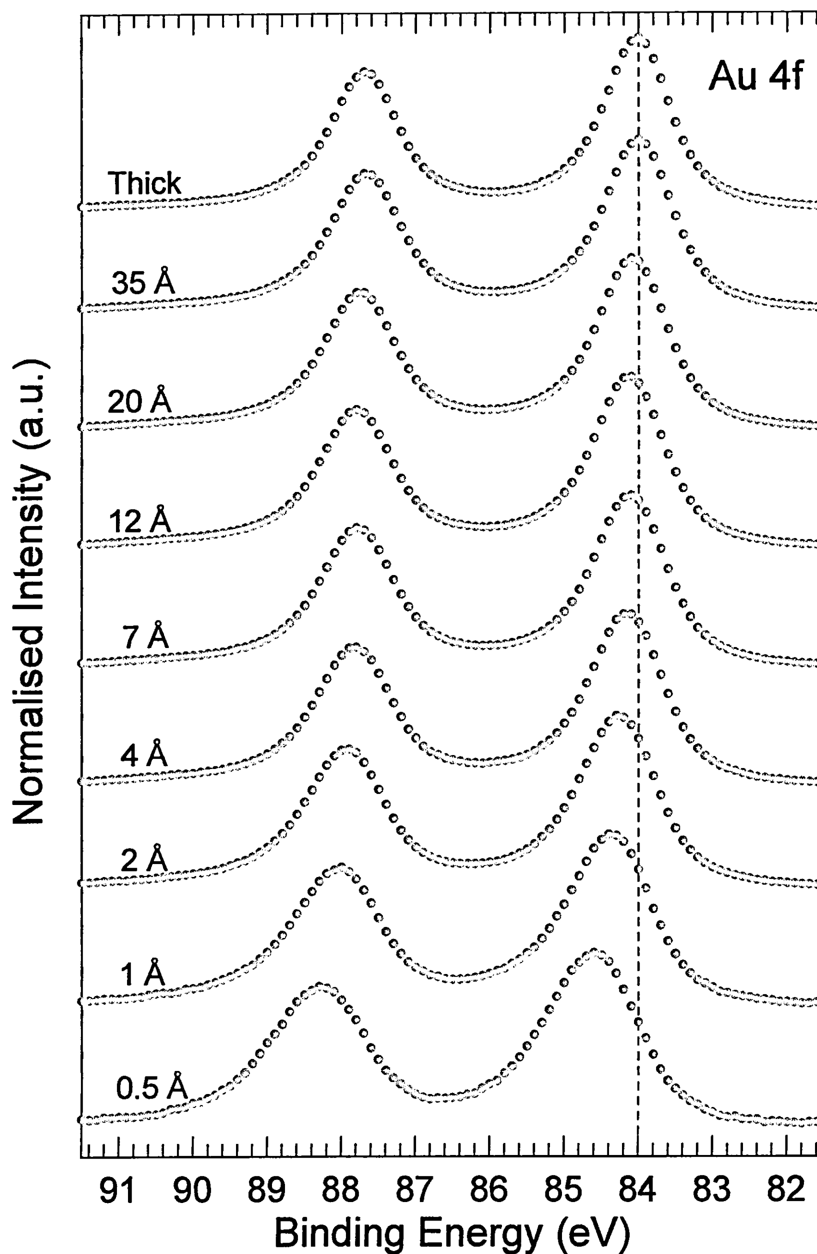

Figure 6-24: evolution of the Au *4f* core level with increasing Au coverage. The top scan was taken after deposition of a thick layer of Au (>500 Å).

The behaviour of the Au *4f* core level (Figure 6-24) is similar to that observed on the 600°C annealed surface. The Au $4f_{7/2}$ peak becomes sharper with increasing Au coverage, shifts to lower binding energy and stabilises at 84 eV, the binding energy of metallic Au. These two facts were thought to be related to chemical changes, from Au-Ga alloy near the interface to pure Au at high Au coverage. As before, this suggests that the interface is abrupt since the high binding energy component related to Au-Ga quickly disappears with Au coverage and cannot be observed after only 35 Å of Au.

6.6 Discussion

An XPS and I-V investigation of the formation of Au contacts on nGaN after three different pre-metallisation surface treatments has been presented. Analysis of the results revealed striking differences in the interface formation mechanisms and electrical properties of the contacts. It is important to stress that the three samples used in the study have been cut from the same wafer and subjected to the same HF etch, so that the number of variable parameters have been kept to a minimum. It is particularly important in the case of GaN, as growth techniques are not as well established as for other semiconductor materials and samples from different growth runs might differ widely.

6.6.1 Interface formation

The evolution of the GaN and Au core levels intensity with increasing Au coverage suggests that Au growth on all three surfaces follows the Stransky-Krastanov mode, namely layer by layer growth followed by clustering. This is to some extent in contradiction with the results reported by Sporken *et al.* who found that Au growth is two dimensional on nGaN at room temperature. Assuming the Stransky-Krastanov mode of growth, the core level intensity versus Au coverage data points from the first Au depositions can be fitted by an exponential curve yielding the attenuation length, or photoelectron escape depth of the core level. As the core level spectrum were recorded at two emission angles, giving a 'bulk sensitive' and a 'surface sensitive' spectrum, the experimentally determined escape depth should be smaller in the surface sensitive case. This is however only verified for the chemically etched and the 600°C annealed surfaces, where the experimental and theoretical values are in reasonable agreement, although the thickness measured by the quartz crystal monitor appeared to have been underestimated by a factor between 2 and 4. The Ga reflux surface, however, yielded similar escape depths at both emission angles, possibly as a result of surface roughening induced by the Ga reflux cleaning cycles. However, Atomic Force Microscopy (AFM) measurements performed on both the 600°C annealed and Ga reflux surfaces yielded similar surface roughness, as shown on Table 6-7.

	600°C anneal	Ga reflux
Mean roughness (nm)	1.042	1.127

Table 6-7: mean surface roughness measured by AFM over a 5x5 μm^2 area after two different *in-situ* surface treatment.

The evolution of the Au $4f_{7/2}$ core level binding energy, shown on Figure 6-25, provides more information about the difference between the Ga reflux surface and the two other surfaces.

The Au $4f_{7/2}$ binding energy for the 600°C annealed (84.3 eV at 1 Å) and HF etched (84.6 eV at 0.5 Å) surfaces at low coverage is greater than that of pure Au (84 eV). As the Au thickness increased the binding energy decreased and finally stabilised at 84 eV. This shift was interpreted by a change in the chemical phase of Au, from Au-Ga bonding near the interface to pure Au at high coverage. Since the theoretical escape depth of Au $4f_{7/2}$ photoelectrons is about 20 Å, the fact that the high binding energy component related to Au-Ga alloying is negligible at coverages greater than 35 Å indicates that the interface is abrupt and well-defined.

The Ga reflux surface, on the other hand, followed a very different behaviour. The binding energy of the Au $4f_{7/2}$ core level was near that of pure Au after the first few depositions, increased at higher coverage (20 and 34 Å) and shifted back again at 55 Å. This behaviour seems to indicate that chemical changes occurred within a thick interfacial layer.

In an attempt to gain a better understanding of the interface structure, the two surfaces were also investigated by cross section TEM. The HF etched interface could not be examined because of a poor Au adherence, which made sample preparation extremely difficult. Figure 6-26 shows that the 600°C annealed surface results in an well-defined, abrupt Au-GaN interface, in good agreement with the core level attenuation plots and the Au $4f_{7/2}$ binding energy shift.

The Ga reflux interface, however, presents a much more complex structure. Figure 6-27 shows the presence of an intermediate layer about 600 Å thick between GaN and polycrystalline Au. This layer consists of Au grains embedded in a GaN matrix. The structural differences between the two interfaces can be correlated to the difference in binding energy shifts observed using XPS during the formation of the two interfaces. These are discussed in more details in the next section.

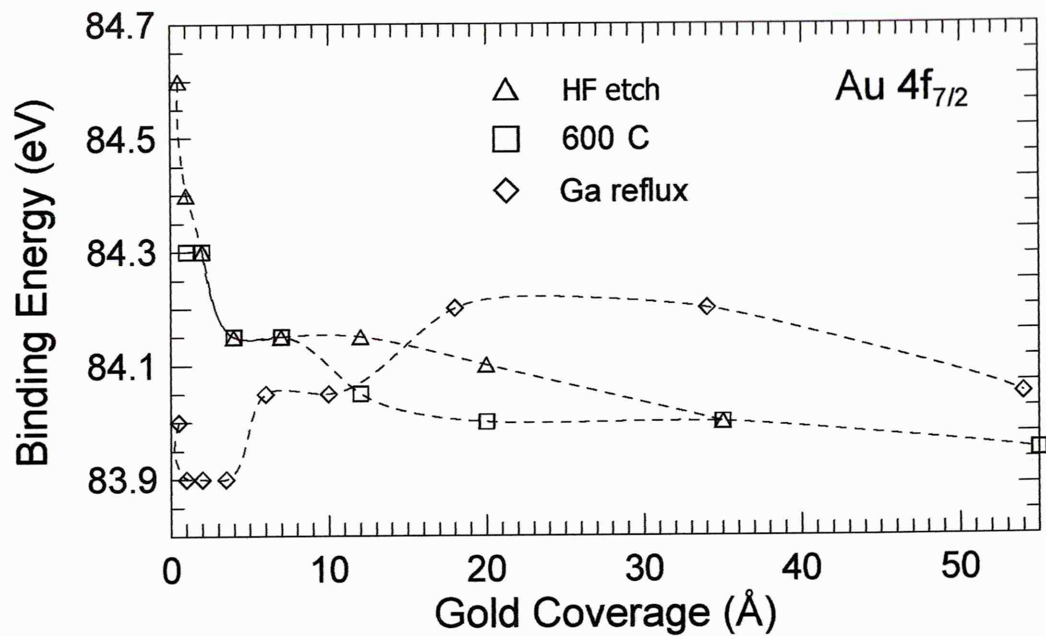

Figure 6-25: variation of the Au $4f_{7/2}$ core level binding energy with increasing Au coverage for the three surfaces. Dashed lines are intended as a guide to the eye.

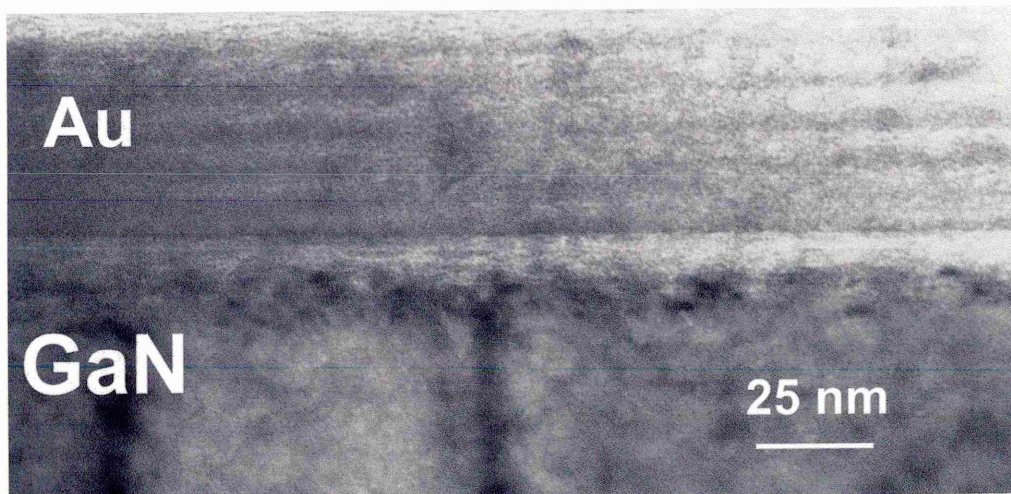

Figure 6-26: cross section micrograph of the Au-GaN interface formed after an *in-situ* 600°C anneal.

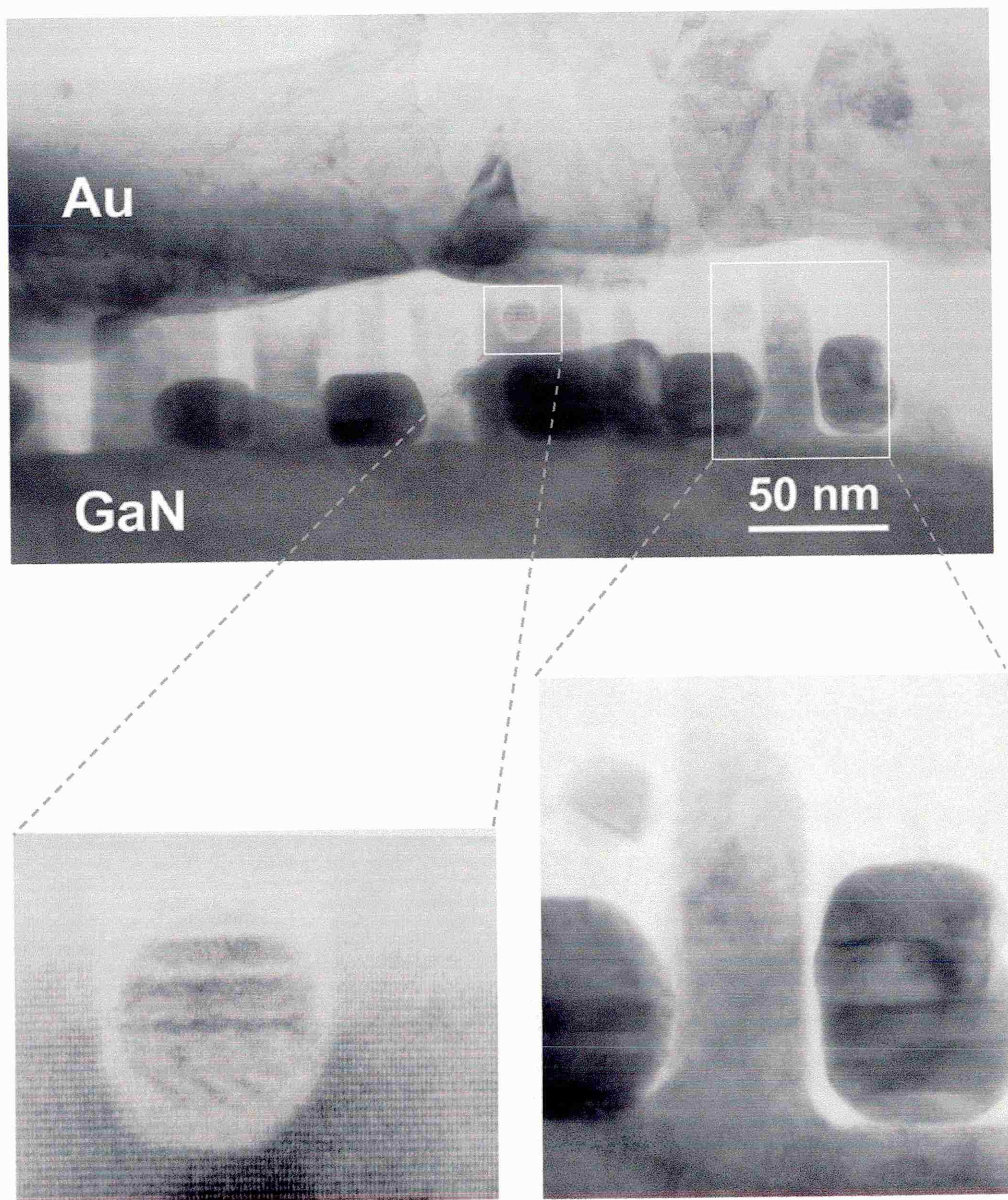

Figure 6-27: cross section micrographs of the Au-GaN interface formed on the Ga reflux surface.

6.6.2 Schottky barrier formation

Transport measurements have been conducted on the diodes formed on the 600°C annealed and Ga reflux surfaces. Unfortunately, it was not possible to measure the contacts formed on the HF etched surface. The diodes formed on the 600°C annealed surface yielded an average barrier height of 1.24 eV, which compares to 0.84 eV for the Ga reflux surface.

Figure 6-28 shows the evolution of the Ga *3d* core level binding energy for the three surfaces. We have seen throughout this chapter that the N *1s* binding energy follows the same variation and that no significant changes in the shape of both peaks were observed. Therefore, it is likely that these shifts are rigid Fermi shifts and correspond to band bending at the surface.

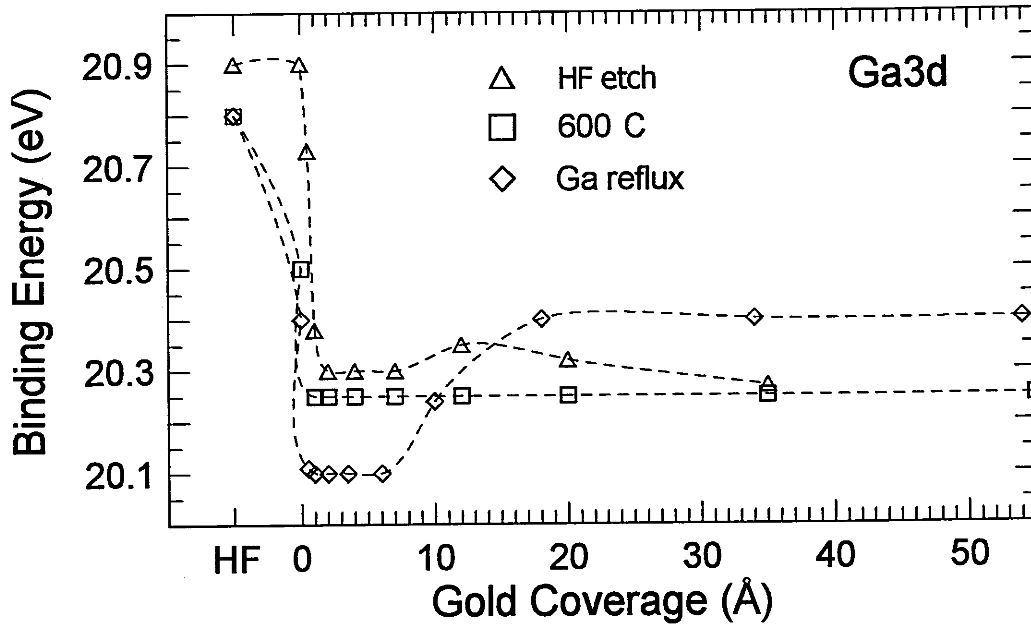

Figure 6-28: variation of the Ga *3d* core level binding energy with increasing Au coverage for the three surfaces. Dashed lines are intended as a guide to the eye.

The 600°C annealed surface and the HF etched surface followed the same trend: the first few Au depositions induced upward band bending and further Au depositions did not induce any further band bending. The Ga reflux surface also exhibited a slight upward band bending after the initial depositions but the bands bent back down at higher Au coverage. The total band bending for the three surfaces, from HF etch to final Au deposition, are given in Table 6-8. The total XPS band bending for the Ga reflux surface is less than that of the 600°C annealed surface, which is consistent with the barrier heights measured by I-V. However, the difference in barrier height (0.4 eV) is greater than the band bending difference (0.15 eV). This point will be discussed later in the text.

	HF etch	600°C anneal	Ga reflux
Band bending after:			
In-situ surface treatment	N/A	0.35 eV	0.45 eV
Au deposition	0.6 eV	0.25 eV	0 eV
Total	0.6 eV	0.6 eV	0.45 eV

Table 6-8: summary of Fermi level variation at the Au-GaN interface for the three surfaces.

The fact that the total XPS band bending (0.6 eV) for the 600°C annealed surface is much less than the barrier height measured by I-V (1.24 eV) suggests that the HF etched surface presents an initial band bending of about 0.65 eV.

As seen in section 2.2.2, Bermudez[63] has suggested that the behaviour of metal-GaN contacts could be interpreted within the Cowley-Sze model[64], where the barrier height is expressed as a sum of the "bare surface barrier height" and a Schottky-Mott term. This model, described in section 3.1.7, assumes an uniform distribution of surface states, the density of which, in the case of GaN[63], is strongly dependent on surface preparation.

Wu *et al.*[59] and Sporken *et al.*[57] have respectively reported a bare surface barrier height of 0.7 eV and 2.2 eV and an Au induced band bending of 0.5 eV and –1.05 eV, as measured by photoemission. The final barrier heights are similar (1.2 eV) and compare well with our results, though the mechanisms of interface formation are different. The Cowley-Sze model cannot account for Sporken's result, since Au deposition caused the bands to bend in the opposite way of that predicted by the Schottky-Mott theory.

According to the Cowley-Sze model, the bare surface barrier height at the 600°C annealed surface would be about 1 eV and the Schottky-Mott contribution 0.25 eV. This leads to a density of surface states of about 2.3×10^{13} $cm^{-2}eV^{-1}$, derived using equations [3-15] and [3-16], and by taking a value of 3.3 eV for the GaN electron affinity[52,59,63]. This high density of surface states reflects the fact than most of the final barrier height is due to initial band bending, which occurs prior to metal deposition. Similarly, the Schottky-Mott contribution for the HF etched surface would be 0.6 eV, indicative of a lesser degree of Fermi level pinning than for the annealed surface, whilst the initial band bending was found to be 0.65 eV.

The anneal therefore caused an increase in the density of surface states which enhanced band bending at the surface, from 0.65 eV for the HF etched surface to 1 eV. The initial band bending at the HF etched surface is somewhat unexpected as practical surfaces are thought to display near flat-band condition[61]. The surface states responsible for this band bending might be caused by structural defects created during GaN growth, such as threading dislocations spreading to the surface. The low mobility and carrier concentration of the layer does indicate a high defect density[124], which might explain the high final Schottky barrier.

Spicer *et al.*[68] suggested that Schottky barrier heights are nearly always determined by defects at the interface. In the so called 'Unified Defect Model' (UDM), it is assumed that defects are generated near the semiconductor surface when the metal contact is deposited on that surface. These defects in turn lead to Fermi level pinning. According to this model, our results for the two surfaces could be interpreted as follows:

- Au deposition on the HF etched surface induces defects and causes a 0.6 upward band bending.
- Annealing at 600°C induces defects and an upward band bending of 0.35 eV, then Au deposition pulls the bands a further 0.25 eV up by creating more defects.

Since the band bending is the same in both cases, annealing and Au deposition seem to induce similar defects on the surface.

The Ga reflux surface resulted in a more complex interface, which cannot be described fully by the Cowley-Sze model. The initial Au depositions induce upward band bending and could be interpreted in terms of the Schottky-Mott model, but the downward band bending at higher Au coverage calls for a different model. Downward band bending has been observed by Sporken *et al.*[57]. They found that their XPS measured Au-nGaN Schottky barrier height (1.15 eV) was in good agreement with that predicted by the MIGS and electronegativity model (0.96 eV). Our I-V measured barrier height (0.84 eV) is also in good agreement with this model. However, the MIGS model does not take into account reacted interfaces.

The effective work function model (EFW) was found to give good predictions for a number of reacted Au contacts to III-V and II-VI semiconductor compounds. This model states that chemical reactions during metal deposition tend to generate excess anion at the interface and therefore the Schottky barrier height could be given by the

difference of the anion work function and the electron affinity. This model is however not applicable to contacts to GaN since the work function of N is not defined.

Finally, Figure 6-29 highlights another important difference between the two *in-situ* surface treatments. The barrier heights are plotted as a function of the ideality factors for a number of diodes from the 600°C annealed and Ga reflux surfaces. The spread in values for the Ga reflux surface indicates poor contact uniformity, only 9 of more than 40 diodes had ideality factors below 2 and some contacts exhibited Ohmic-like behaviour. The 600°C annealed surface resulted in a much better contact uniformity, with most of the diodes having ideality factors below 1.2. The difference in the electrical properties for the two surface treatments reflects the structural and chemical differences of the two interfaces.

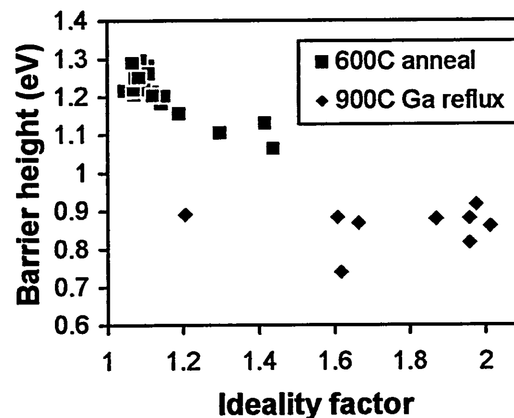

Figure 6-29: barrier height versus ideality factor for Au-nGaN diodes formed on two different surfaces. The Schottky parameters have been extracted by the conventional method.

We have mentioned that the difference in barrier heights is greater than the difference in XPS band bending between the two surface treatments. It could be a consequence of the poor uniformity and high ideality factors, which might lead to underestimation of the barrier height. Indeed, when the interface presents local variation of the barrier height as it seems to be the case for the Ga reflux surface, the I-V technique tends to yield the lowest value while XPS gives an average of the band bending.

We have seen previously that both surfaces are likely to present a high density of defects, which usually results in tunnelling and recombination current. However, these defects do not seem to be electrically active in the case of the 600°C annealed surface as indicated by the low ideality factors and good uniformity of the contacts. This changes drastically when the surface is cleaned by the Ga reflux technique prior to metallisation. A similar behaviour was observed for the Ag-GaN diodes fabricated on nGaN after Ga reflux cleaning (section 5.5). It is possible that the cleaning technique activated the defects and/or created additional, electrically active defects since annealing at high temperature has been shown to induce defects state within the band gap[122,123].

It is also possible that the high temperature annealing steps involved in the Ga reflux cleaning process resulted in loss of N at the surface[47]. As N vacancies act as donors[5], this loss of N would render the surface highly n-type, therefore enhancing tunnelling.

Another possible explanation lies with the O content at the surface. Surface O has been reported to diffuse along threading dislocations to form a GaO layer underneath the interface. The yellow luminescence band observed on MBE grown GaN has been linked to this GaO layer. It is therefore possible that the surface defects could be affected by the GaO layer and perhaps neutralised in the case of the annealed surface, but not for the Ga reflux surface as it contains less O.

6.6.3 Conclusions

Pre-metallisation surface treatment was found to play a very important role in the structural and electrical properties of Au-nGaN contacts.

XPS and TEM studies showed that Au contacts formed after an *in-situ* 600°C anneal exhibited a smooth, abrupt interface while contacts formed after *in-situ* cleaning by the Ga reflux method displayed a reacted, more complex interface, with evidence of Au-GaN mixing. Analysis of the XPS core level binding energy position showed that both surface treatments caused upward band bending at the surface. The first few Au depositions induced further upward band bending in both cases but the Ga reflux surface underwent reverse band bending as the Au coverage increased while the 600°C annealed surface did not change. The total band bending induced by Au deposition was 0.25 eV and 0 eV for the 600°C annealed surface and Ga reflux, respectively.

Transport measurements performed on the same samples after processing confirmed the fundamental difference between the two surfaces. Contacts formed on the 600°C annealed surface and Ga reflux exhibited an average Schottky barrier height of 1.24 eV and 0.84 eV, respectively. The lowest ideality factors were 1.03 and 1.18, respectively. The contact uniformity was very good in the case of the annealed surface and poor for the Ga reflux surface, in good agreement with XPS and TEM studies.

XPS study of Au deposition on the third surface, which was only subjected to a *ex-situ* cleaning in a HF:DI $H_2$0 solution showed a similar behaviour to the 600°C annealed surface. The total band bending induced by the Au deposition was 0.6 eV, which is equal to the sum of the band bending caused by the 600°C anneal and the subsequent Au deposition.

The Cowley-Sze and unified defect models were put forward to interpret the behaviour of the HF etched and annealed surfaces and suggest a high density of acceptor states at the surface. The high barrier reported is possibly a consequence of this high density of states, themselves caused by a high density of defects. These defects did not seem to act as recombination or tunnelling centres for the 600°C annealed surface as opposed to the Ga reflux surface, whose electrical behaviour suggests electrically active defects. The complexity of the interface in the latter case means that no single model of Schottky barrier formation can interpret the results in a satisfactory manner.

Chapter 7: Conclusion

GaN has attracted considerable interest over the last 10 years, mainly because its direct, 3.4 eV band gap has allowed the development of high brightness, blue LEDs and LDs[5]. However, GaN is also a very promising semiconductor material for the fabrication of high frequency microelectronics devices able to operate at high temperature, such as HEMTs and MESFETs. The working principle of these devices relies on the properties of metal Schottky contacts. Hence, the fabrication of reproducible, reliable high barrier Schottky contacts is crucial.

As GaN is a relatively recent material, the issue of metal contacts to GaN is not as well understood as for more established semiconductor materials such as Si, GaAs or InP. As discussed in Chapter 2, several independent studies[37-46] have shown that the barrier potential at metal Schottky contacts to nGaN increases with the metal work function, although the slope of the increase varies from study to study. This discrepancy, and the additional fact that measured barrier heights from different works on the same metals yielded significantly different values, indicates that other factors such as growth method, surface polarity and pre-metallisation surface treatments play an

important role in determining the final barrier height. In particular, vacuum deposited metal contacts prepared *in-situ* after high temperature annealing yielded higher barriers than contacts prepared after an *ex-situ* surface treatment.

The aim of this work was to investigate the influence of both *ex-situ* and *in-situ* pre-metallisation surface preparation on the barrier height of Schottky contacts to nGaN in order to define a reproducible process for the fabrication of reliable, near ideal, high barrier Au contacts to nGaN. Two main experiments were conducted during the course of this work. The central experimental techniques employed to probe the GaN surfaces and metal-GaN interfaces were XPS, and, to a lesser extent, SXPS. The metal-GaN contacts were also characterised by I-V measurements and TEM.

The first experiment, described in Chapter 5, is an XPS and SXPS investigation of three different, increasingly complex, surface preparations. The first surface treatment is a simple *ex-situ* chemical treatment. The GaN substrate was degreased in solvent and dipped in an HF solution, thus mimicking the 'practical contacts' surface treatment employed in device manufacture. The second surface treatment consisted of the same *ex-situ* chemical etch, followed by *in-situ* annealing at 600°C. The last pre-metallisation treatment investigated consisted, once again, of the *ex-situ* etch followed by two cycles of *in-situ* Ga reflux cleaning. Finally, Ag contacts made *in-situ* on the third surface were characterised by I-V measurements.

Analysis of the XPS data showed that these three pre-metallisation treatments produced surfaces increasingly free of C and O contaminants, compared to the starting surface. Wet chemical etching in HF reduced O contamination but failed to remove C contamination. Annealing in UHV at 600°C reduced surface O contamination further while Ga reflux cleaning resulted in O levels barely detectable by XPS and caused a significant drop of C contamination compared to the HF etched surface. Additionally, HF etching, UHV annealing and UHV Ga reflux cleaning caused increasingly greater upward band bending at the surface, suggesting a possible link between surface barrier height and O content at the surface. Fermi level displacement during Ga reflux cleaning was investigated further by SXPS. Ga deposition at 600°C was found to produce a 1.0 eV upward band bending while Ga re-evaporation at 775°C was accompanied by a –0.6 eV downward band bending. The MIGS[66] and unified defect models[68] were put forward as a possible explanation for this partially reversible shift. I-V measurements performed on Ag contacts formed *in-situ* on the Ga reflux cleaned GaN substrate yielded a barrier

height of 0.80 eV for an ideality factor of 1.56, in good agreement with the SXPS results and previous work[50].

The second experiment, presented in Chapter 6, is an investigation of Au contact formation on the three surfaces studied in the previous experiment using XPS, I-V and cross section TEM. The GaN samples used in this study were cut from the same wafer in order to minimise the number of parameters. Au was deposited in steps of increasing thickness, from sub-monolayer to blanket coverage, on the HF etched, UHV annealed and Ga reflux cleaned surfaces.

The three, fundamentally different, experimental techniques employed to probe the Au-GaN interfaces revealed striking differences between the HF etched and UHV annealed surfaces on one hand, and the Ga reflux surface on the other. Core level analysis and cross section TEM micrographs suggested that the Au-nGaN interface is abrupt and well defined for the former two surface preparations. Conversely, the results indicated that the Ga reflux surface treatment resulted in a more complex interface with evidence of GaN-Au intermixing. Analysis of the binding energy shift of the GaN core levels yielded a total (from HF etch to final Au deposition) upward band bending of 0.6 eV for both the HF etched and the UHV annealed surfaces. For the annealed surface, this band bending was partly due to the anneal (0.35 eV) and partly to the Au deposition (0.25 eV). In the case of the HF etched surface, the 0.6 eV band bending occurred as a result of Au deposition only. The total band bending observed on the Ga reflux sample was 0.45 eV, entirely caused by the cleaning process. I-V measurements conducted on circular diodes formed on the 600°C annealed and Ga reflux samples confirmed the XPS results. Diodes from the annealed sample exhibited high Schottky barriers (mean ϕ_{B0}=1.25 eV) low ideality factors (best n=1.03) and high contact uniformity. Conversely, I-V measurements conducted on the Ga reflux sample yielded lower barriers (mean ϕ_{B0}=0.85 eV), poor ideality factors and contact uniformity.

I-V and XPS results from the 600°C annealed surface suggest that the HF etched surface presents an initial band bending of 0.65 eV, which is further enhanced by annealing. The final barrier heights of Au-nGaN contacts formed after *in-situ* annealing could therefore be interpreted in terms of the Cowley-Sze model, as the sum of the bare surface band bending and Au induced band bending. The bare surface band bending means a high density of acceptor surface states, which might be caused by structural defects created during GaN growth. These surface defects did not appear to act as

recombination or tunnelling centres, in contrast with Au and Ag contacts formed after Ga reflux cleaning.

The remarkable electrical and structural changes caused by pre-metallisation surface treatment could be further investigated using Scanning Tunnelling Microscopy (STM) and Spectroscopy (STS). As opposed to TEM, STM is a non-destructive electron microscopy technique, which allows imaging of monocrystalline surfaces down to the atomic scale. By simultaneously performing STM and STS, it is possible to correlate local structural surface features such as atom vacancies and point defects with local variations of the electronic properties. Local band bending thus obtained by STS could then be compared with the average band bending and barrier heights obtained by XPS and I-V. Figure 7-1 shows an example of what STM can achieve on GaN. This powerful technique would be ideal to probe the defected GaN surfaces and the effect of sub-monolayer metal coverage.

Figure 7-1: 750 Å × 750 Å STM image of a screw-type dislocation on the N-face of wurtzite GaN (Ref. 125).

[1] F. Braun, Ann. Phy. Chem. **153**,556 (1874)
[2] J. Bardeen and W.H. Brattain, Phys. Rev. **74**, 230 (1948)
[3] J.I. Pankove E.A. Miller and J.E. Berkeyheiser, RCA Review **32**, 383 (1971)
[4] H. Amano, Jap. J. Appl. Phys. **28**, 2112 (1989)
[5] S. Nakamura, G. Fasol, "The Blue Laser Diode", Springer (1997)
[6] F. Binet, J.Y. Duboz, N. Laurent, E. Rosencher, O. Briot and R.L. Aulombard, J. Appl. Phys. **81**(9), 6449 (1997)
[7] J.C. Carrano, T. Li, P.A. Grudowski, C.J. Eiting, R.D. Dupuis and J.C. Campbell, , J. Appl. Phys. **83**(11), 6148 (1998)
[8] E. H. Rhoderick and R. H. Williams, 'Metal-semiconductor contacts', Oxford university press (1988)
[9] Q. Z. Liu and S. S. Lau, Solid-State Electronics, **42**(5), 677 (1998)
[10] B. P. Luther, S. E. Mohney, T. N. Jackson, M. A. Khan, Q. Chen and J. W. Wang, Appl. Phys. Lett. **70**(1), 57 (1997)
[11] X. A. Cao, F. Ren, S. J. Pearton, A. Zeitouny, M. Eizenberg, J. C. Zolper, C. R. Abernathy, J. Han, R. J. Shul, J. R. Lothian, J. Vac. Sci. Technol. A **17**(4), 1221 (1999)
[12] C-T Lee and H-W Kao, Appl. Phys. Lett. **76**(17), 2364 (2000)
[13] J.S. foresi, T.D. Moustakas, Appl. Phys. Lett **62**(22), 2859 (1993)
[14] D. B. Ingerly, Y. A. Chang, N. R. Perkins and T. F. Kuech, Appl. Phys. Lett. **70**(1), 108 (1997)
[15] J. D. Guo, C. I. Lin, M. S. Feng, F. M. Pan, G. C. Chi, C. T. Lee, Appl. Phys. Lett. **68**(2), 235 (1996)
[16] B. P. Luther, J. M. DeLucca, S. E. Mohney, R. F. Karlicek, Jr., Appl. Phys. Lett. **71**(26), 3859 (1997)
[17] Zhifang Fan, S. Noor Mohammad, Wook Kim, Özgür Aktas, Andrei E. Botchkarev, Hadis Morkoç, Appl. Phys. Lett. **68**(12), 1672 (1996)
[18] A.T. Ping, M. Asif Khan, I. Adesida, J. of Elec. Mat., **25**(5), 819 (1996)
[19] M.E. Lin, Z. Ma, F.Y. Huang, Z.F. Fan, L.H. Allen, H. Morkoç, Appl. Phys. Lett. **64**(8), 1003 (1994)
[20] L. F. Lester, J. M. Brown, J. C. Ramer, L. Zhang, S. D. Hersee and J. C. Zolper, Appl. Phys. Lett. **69** (18), 2737 (1996)
[21] J. Burm, K. Chu, W. A. Davis, W. J. Schaff, L. F. Eastmann, T. J. Eustis, Appl. Phys. Lett. **70**(4), 464 (1997)
[22] M.W. Cole, D.W. Eckart, W.Y. Han, R.L. Pfeffer, T. Monahan, F. Ren, C. Yuan, R.A. Stall, S.J. Pearton, Y. Li, Y. Lu, J. of Appl. Phys.**80**(1), 278 (1996)
[23] CT Lee, MY Yeh, YT Lyu, Journal of Electronic Materials 26(3), 262 (1997).
[24] N. A. Papanicolaou, A. Edwards, M. V. Rao, J. Mittereder and W. T. Anderson, J. of Appl. Phys. **87**(1), 380 (2000)
[25] M.E. Lin, F.Y. Huang, H. Morkoç, Applied Physics Letters **64**(19), 9/5/94, pp 2557-2559
[26] H. Ishikawa, S. Kobayashi, Y. Koide, S. Yamasaki, S. Nagai, J. Umezaki, M. Koide and M. Muramaki, J. Appl. Phys. **81** (3), 1315 (1997)
[27] Jong Kyu Kim, Jong-Lam Lee, Jae Won Lee, Hyun Eoi Shin, Yong Jo Park and Tael Kim, Appl. Phys. Lett. **74** (2), 275 (1999)
[28] M. Suzuki, T. Kawakami, T. Arai, S. Kobayashi, Y. Koide, T. Uemura, N. Shibata, M. Murakami, Appl. Phys. Lett. **73** (20), 2953 (1998)
[29] J. M. Delucca, H. S. Venugopalan, S. E. Mohney and R. F. Karlicek, Jr, Appl. Phys. Lett. **73** (23), 3402, (1998)
[30] D. B. Ingerly, Y. A. Chang and Y. Chen, MRS Internet J. Nitride Semicond. Res. **4S1**, G6.49 (1999)
[31] D. B. Ingerly, Y. A. Chang and Y. Chen, Appl. Phys. Lett. **74**(17), 2480 (1999)
[32] J-K Ho, C-S Jong, C. C. Chiu, C-N Huang, C-Y Chen, K-K Shih, Appl. Phys. Lett. **74**(9), 1275 (1999)
[33] J-S jang, I-S Chang, H-K Kim, T-Y Seong, S. Lee, S-J Park, Appl. Phys. Lett. **74**(1), 70 (1999)
[34] T. Maeda, Y. Koide and M. Muramaki, Appl. Phys. Lett. **75**(26), 4145 (1999)
[35] S. Kurtin, T. C. McGill and C. A. Mead, Phys. Rew. Lett. **22**(26), 1433 (1969)
[36] H. Hasegawa, Y. Koyama, and T. Hashizume, Jpn. J. Appl. Phys. **38**(4B), 2634 (1999)
[37] P. Hacke, T. Detchprohm, K. Hiramatsu, and N. Sawaki, Appl. Phys. Lett. **63** (19), 2676 (1993)
[38] S.C. Binari, H.B. Dietrich, G Kelner, L.B. Rowland, K. Doverspike, D.K. Gaskill, Electronics Letters,. **30**(11), 909 (1994)
[39] J. D. Guo, M. S. Feng, R. J. Guo, F. M. Pan, C. Y. Chang, Appl. Phys. Lett., **67**(18), 2657 (1995)
[40] S.N. Mohammad, Z. Fan, A.E. Botchkarev, W. Kim, O. Aktas, A. Salvador, H. Morkoç, Electronics Letters, **32**(6), 597 (1996)
[41] Lei Wang, M. I. Nathan, T-H. Lim, M. A. Khan and Q. Chen, Appl. Phys. Lett. **68**(9), 1267 (1996)

[42] E. V. Kalinia, N. I. Kuznetsov, V. A. Dmitriev, K. G. Irvine and C. H. Carter, Jr, J. of Electron. Mat., **25**(5), 831 (1996)
[43] Y. Kribes, I. Harrison, B. Tuck, T. S. Cheng and C. T. Foxon, Semiconductor Science Technology, **12**, 913 (1997)
[44] A. C. Schmitz, A. T. Ping, M. Asif Khan, Q. Chen, J. W. Yang, and I. Adesida, J. of Electron. Mat., **27**(4), 255 (1998)
[45] Q. Z. Liu, L. S. Yu, F. Deng, S. S. Lau and J. M. Redwing, J. of Appl. Phys. **84**(2), 881 (1998)
[46] Y. Koyama, T. Hashizume, and H. Hasegawa, Solid-State Electronics **43**, 1483 (1999)
[47] S. W. King, J. P. Barnak, M. D. Bremser, K. M. Tracy, C. Ronning, R. F. Davis and R. J. Nemanich, J. of Appl. Phys. **84** (9), 5248 (1998)
[48] M. Asif Khan, J. N. Kuznia, D. T. Olson and R. Kaplan, J. of Appl. Phys. **73**(6), 3108 (1993)
[49] V. M. Bermudez, R. Kaplan, M. A. Khan and J. N. Kuznia, Physical review B **48**(4), (1993)
[50] T. U. Kampen, W. Mönch, Appl. Surf. Sci. 117/118, 388 (1997)
[51] J. Dumont, R. Caudano, R. Sporken, E. Monroy, E. Muñoz, B. Beaumont and P. Gibart, MRS Internet J. Nitride Semicond. Res.
[52] V. M. Bermudez. J. Appl. Phys. **80** (2), 1190 (1996)
[53] C. I. Wu, A. Kahn, N. Taskar, D. Dorman, and D. Gallagher, J. Appl. Phys. **83**(8), 4249 (1998)
[54] Jian Ma, B. Garni, N. Perkins, W. L. O'Brien, T. F. Kuech and M. G. Lagally, Appl. Phys. Lett. **69** (22), 3351 (1996)
[55] R. A. Beach, E. C. Piquette, T. C. McGill and T. J. Watson, MRS Internet J. Nitride Semicond. Res. **4S1**, G6.26 (1999)
[56] M. Eylecker, W. Mönch, T. U. Kampen, R. Dimitrov, O. Ambacheer and M. Stuuzmann, J. Vac. Sci. Technol. B **16**(4), 2224 (1998)
[57] R. Sporken, C. Silien, F. Malengrau, K. Grigorov, R. Caudano, F. J. Sánchez, E. Cajella, E. Munoz, B. Beaumont and P. Gibart, MRS Internet J. Nitride Semicond. Res. **2**, 23 (1997)
[58] A. R. Smith, R. M. Feenstra, D. W. Greve, M.-S. Shin, M. Skowronski, J. Neugebauer, J. E. Northrup, Appl. Phys. Lett. **72**(17) 2114 (1998)
[59] C. I. Wu and A. kahn, J. Vac. Sci. Technol. B **16**(4), 2218 (1998)
[60] V.M. Bermudez, R Kaplan, M. A. Khan and J. N. Kuznia, Phys. Rev. B **48**, 2436 (1993)
[61] V. M. Bermudez, T. M. jung, K. Doverspike and A.E. Wickenden, J. Appl. Phys. **79**(1), 110 (1996)
[62] V. M. Bermudez, Surf. Sci. **417**, 30 (1998)
[63] V.M. Bermudez, J. Appl. Phys. **86**(2), 1170 (1999)
[64] A. M. Cowley and S. M. Sze, J. Appl. Phys **36**, 3212 (1965)
[65] S. M. Sze, 'Semiconductor devices, Physics and technology', John Wiley & sons
[66] V. Heine, Physical review A **138**, 1689 (1965)
[67] S. G. Louie and M. L. Cohen, Physical review B **13**, 4172 (1976)
[68] W. E. Spicer, I. Lindau, P. Skeath, C. Y. Su, P. W. Chye, Physical review letter **44**, 420 (1980)
[69] L.N. Pauling, "The nature of the chemical bond", 2nd ed., Cornell University Press, Ithaca, NY (1960)
[70] S. Kurtin, T. C. McGill, C. A. Mead, Physical review letter **22**, 1433 (1969)
[71] W. Mönch, J. Vac. Sci. Technol. B **17**(4), 1867 (1999)
[72] A.M. Cowley and S.M. Sze, J. Appl. Phys. **36**, 3212 (1965)
[73] H. A. Bethe, M.I.T. Radiat. Lab. Rep., 43-12, (1942)
[74] H. K. Henisch, 'Semiconductor contacts', Oxford university press (1988)
[75] F. A. Padovani and R. Stratton, Solid state electronic **9**, 695 (1966)
[76] C. T. Sah, R. N. Noyce and W. Shockley, Proc. IRE **45**, 1228 (1957)
[77] J.H. Werner, Appl. Phys. A **47**, 291 (1988)
[78] L.F. Wagner, R.W. Young and A. Sugerman, IEEE Electronic device Letter **EDL-4**(9), 320 (1983)
[79] A. Einstein, Ann. Physik, **17**, 132 (1905)
[80] T. Koopmans, Physica, **1**, 104 (1933)
[81] C.S. Fadley in "Electron Spectroscopy: Theory, Techniques and Applications, Vol. 2", edited by C.R. Brundle and A.D. Baker, Academic Press (1978)
[82] J.J. Yeh and I. Lindau, Atomic Data and Nuclear Tables, **32**,1 (1985)
[83] "Practical Surface Analysis, 2nd Edition, Volume 1 Auger and x-ray Photoelectron Spectroscopy", edited by D. Briggs and M.P. Seah, John Wiley and Sons (1990)
[84] P.J. Feibelman and D.E. Eastman, Phys. Rev. B. **10**, 4932 (1974)
[85] G.D. Mahan, Phys. Rev. B. **10**, 4392 (1970)
[86] B. Feuerbacher and R.F. Willis, J. Phys. C: Solid St. Phys. **9**, 169 (1976)
[87] C.N. Berglund and W.E. Spicer, Phys. Rev. **136**, (4A), A1030 (1964)

[88] E.W. Plummer and W. Eberhardt, Advances in Chemical Physics, **49**, 533 (1982)
[89] C. Cohen-Tannoudji, B. Dui and F. Laloë, "Quantum Mechanics, Vol. 2", J. Wiley & Sons (1977)
[90] J.W. Cooper, Phys. Rev. **128**, 681 (1962)
[91] M.P. Seah and W.A. Dench, Surface and Interface Analysis, **1**, 2 (1979)
[92] D.P Woodruff and T.A. Delchar, "Modern Techniques of Surface Science", Cambridge University Press (1990)
[93] T.A. Carlson, "Photoelectron and Auger Spectroscopy", Plenum, New York (1976)
[94] L.J. Brillson, J. Vac. Sci. Technol. **15 (4)**, 1378-1383 (1978)
[95] W.A. Harrison, "Electronic Structure and Properties of Solids", W.H.Freeman and Co. (1980)
[96] R. Ludeke, Surf. Sci. **132**, 143 (1983)
[97] R.D. Rusk, "Introduction to Atomic and Nuclear Physics", Meredith Publications (1964)
[98] W.H. Press, B.P. Flannery, S.A. Teukolsky and W.T. Vetterling, "Numerical Recipes in Fortran", Cambridge University Press (1986)
[99] D.W. Marquardt, J. Soc. Ind. Appl. Math. **11**, 431 (1963)
[100] J.J. Joyce, M. Del Guidice and J.H. Weaver, J. Electron. Spec. Rel. Phen. **49**, 31 (1989)
[101] D.A. Shirley, Phys. Rev. B, **5**, **5**, 4709 (1972)
[102] P.R Dunstan, PhD Thesis, University of Wales, College of Cardiff (1998)
[103] E. Hecht, "Optics, 2nd Edition", Addison-Wesley Publishing Company (1987)
[104] H. Benson, "University Physics", John Wiley & Sons (1991)
[105] N.V. Edwards, M.D. Bremser, T.W.Jr, R.S. Kern, R.F. Davis, and D.E. Aspnes, Appl. Phys. Lett., **69**, 2065 (1996)
[106] St. Hohenecker, D Drews, M. Lübbe, D.R.T. Zahn, W. Braun, Applied Surface Science **123/124** 585-589 (1998)
[107] P.R. Dunstan, S.P. Wilks, S.R. Burgess, M. Pan, R.H. Williams, D.S. Cammack, S.A. Clark, Applied Surface Science **123/124** 533-537 (1998)
[108] C.J. Spindt, M. Yamada, P.L. Meissner, K.E. Miyano, T. Kendelewicz, A. Herreragomez, W.E. Spicer, A.J. Arko, Physical Review B **45** (19), (1992)
[109] D. Mao, M. Santos, M. Shayegan, A. Kahn, G. Lelay, Y. Hwu, G. Margaritondo, L.T. Florez, J.P. Harbison, Physical Review B **45** (3), (1992)
[110] L.L. Smith, W.S. King, R.J. Nemanich and R.F. Davis, J. Electron. Mater. **25**, 805 (1996)
[111] V. M. Bermudez, D. D. Koleske and A. E. Wickenden, Appl. Surf. Sci. **126**(1-2), 68 (1998)
[112] W.R.L. Lambretch, B. Segall, S. Strite, G. Martin, A. Agarwal, H. Morkoç, A. Rockett, Physical Review B, **50** (19), (1994)
[113] R.F. Schmitsdorf, T.U. Kampen and W. Mönch, J. Vac. Sci. Technol. B **15** (4), (1997)
[114] J. Ivanco, J. Almeida, C. Coluzza , F. Zwick, G. Margaritondo , VACUUM **50**(3-4), 407 (1998)
[115] S.A. Clark, S.P. Wilks, J.I. Morris, D.A. Woolf, R.H. Williams, J. of Appl. Phys. **75**(5) 2481 (1994)
[116] D.S. Cammack, S.A. Clark, P.R. Dunstan, M. Pan, S.P. Wilks, M. Elliot, J. of Appl. Phys **84**(8) 4443 (1998)
[117] M.P. Seah, W.A. Dench, Surf. Interface Anal., **1**, 2 (1979)
[118] Maffeis T G G, Clark S A, Dunstan P R, Wilks S P, Evans D A, Peiro F, Riechert H and Parbrook P J, Phys, Stat. Sol. (a) **176**, 751 (1999)
[119] D.T. Jayne, N.S Fatemi, V.G. Weizer, J. of Vacuum Sci. and Tech. A **10**(4), part 3, 2802 (1992)
[120] He L, Wang Z J, Zhang R, J. Vac. Sci. Technol. A **17**(4), 1217 (1999)
[121] Bandić Z Z, Bridger P M, Piquette E C, McGill T C, Vaudo R P, Phanse V M and Redwing J M, Appl. Phys. Let. **74**(9), 1266 (1999)
[122] L.J. Brillson, T.M. Levin, G.H. Jessen, A.P. Young, C. Tu, Y. Naoi, F.A. Ponce, Y. Yang, G.J. Lapeyre, J.D. MacKenzie, C.R. Abernathy, Physica B **273-274**, 70 (1999)
[123] F.D. Auret, S.A. Goodman, F.K. Koschnick, J-M. Spaeth, B. Beaumont and P. Gibart, MRS Internet J. Nitride Semicond. Res. **4S1**, G6.13 (1999)
[124] C.Y. Hwang, M.J. Schurman, W.E. Mayo, Y.C. Lu, R.A. Stall, T. Salagaj ,J. of Elec. Materials **26**(3), 243 (1997)
[125] A. R. Smith, V. Ramachandran, R. M. Feenstra, D. W. Greve, M.-S. Shin, M. Skowronski, J. Neugebauer, J. E. Northrup, J. Vac. Sci. Technol. A **16**, 1641 (1998)